UNIVERSITY OF SOUTHAMPTON

SCALING AND PERFORMANCE COMPARISONS OF A
CENTRIFUGAL PUMP WITH HYDRODYNAMIC DISC SEALS
RUNNING IN WATER AND MERCURY

by

Stephanie L. Merry

DEPARTMENT OF MECHANICAL ENGINEERING

Submitted for the Degree of Doctor of Philosophy

April 1982.

SCALING AND PERFORMANCE COMPARISONS OF A

CENTRIFUGAL PUMP WITH HYDRODYNAMIC DISC SEALS

RUNNING IN WATER AND MERCURY

VOLUME 1

If you can dream - and not make dreams your master;
If you can think - and not make thoughts your aim,...

- KIPLING.

UNIVERSITY OF SOUTHAMPTON

ABSTRACT

FACULTY OF ENGINEERING AND APPLIED SCIENCE

MECHANICAL ENGINEERING

Doctor of Philosophy

SCALING AND PERFORMANCE COMPARISONS OF A CENTRIFUGAL PUMP
WITH HYDRODYNAMIC DISC SEALS RUNNING IN WATER AND MERCURY

by Stephanie Louise Merry

The performance of a small centrifugal pump, normally used to circulate mercury in an I.C.I. chemical plant, is examined in water and mercury over a range of rotational Reynolds Numbers (Re_ω). It is shown that variations in speed and viscosity are not necessarily equivalent for a given change in Re_ω.

The pump design leads to an unusual relationship between leakage and hydraulic efficiency. A scaling technique, which incorporates the effects of leakage, is developed for predicting the pump performance in mercury from its characteristics in water.

Two factors contributing to excessive wear of the pump neckrings are defined. A hydrodynamic seal (HDS) is designed to replace the upper neckring. The extra power requirement of this seal, which is partially offset by the lower leakage rate, is reduced by staging.

HDS performance is shown to be similar whether it runs alone or as part of the pump. In mercury, the seal interface (with water) is found to be less stable than a water/air interface. Interface instability encourages the entrainment of bubbles, which subsequently collect at the interstage region of a staged HDS, posing a potential problem in practical applications. At low seal inlet pressures in mercury, total interface breakdown can occur for a single or two-stage HDS, resulting in water throughflow.

The peak pump efficiency may be accurately monitored by thermometric measurements in water. The same method is shown to be more suitable for fluids of low thermal capacity, such as mercury, if the experimental technique can be refined.

ACKNOWLEDGMENTS

CONTENTS : VOLUME I

CONTENTS : VOLUME II

NOTATION

[N.B. The following symbols are used in Chapters 1-12 and Appendices I-XVIII. In Chapter 13 and associated Appendices (XVIII and XIX) the traditional notation for thermodynamics is employed, as set out at the beginning of that Chapter, which conflicts in some cases with the definitions given below]

Units

a	Vane height	mm
A	Area	m^2
b	Vane width	mm
c	Fluid velocity	$m.sec^{-1}$
$\dot{c}$	Fluid acceleration	$m.sec^{-2}$
C	Clearance between pump intake and sump floor	m
C_D	Drag coefficient	-
C_{EL}	End load coefficient of a HDS $[\dfrac{E.L.}{\frac{1}{2}\rho\omega^2 R^4}]$	-
C_f	Friction coefficient	-
C_M	Torque absorption coefficient $[\dfrac{2M}{\rho\omega^2 R^5}]$	-
C_p	HDS Pressure coefficient $[\dfrac{\Delta p}{\frac{1}{2}\rho\omega^2 R^2}]$	-
	(Local $C_p = \dfrac{P_{tap}}{\frac{1}{2}\rho\omega^2 R^2}$)	
C_v	Basic Coefficient for a Venturi Tube	-
d	Mean slot (seal clearance) diameter	mm
D	Diameter	m.
E	Velocity approach factor for a venturi tube	-
E.L.	End load	N
E_v	Nett suction energy	$J.kg^{-1}$
f	Friction factor	-
F_B	Buoyancy force	N
F_D	Drag force	N
g	Acceleration due to gravity	$m.sec^{-2}$

H	Pressure head	m. of fluid
H_r	Theoretical Euler head	m. of fluid
k	Slip factor	-
K_c	Loss coefficient at a pipe contraction	-
L	Length	m
M	Torque	N.m.
n	Rotational speed	rpm
n_s	Specific speed $[\dfrac{\omega Q^{\frac{1}{2}}}{(gH)^{\frac{3}{4}}}]$	-
N	Number of stages in a multistage HDS	-
p	Pressure	$N.m^{-2}(Pa)$
p_v	Vapour pressure	$N.m^{-2}(Pa)$
P_{in}	Input power	W
P_{out}	Output power	W
Q	Pump delivered flowrate	m^3sec^{-1} or $\ell.min^{-1}$
r	Droplet radius	μm
R	Radius	m
Re	Reynolds Number	-
Re_B	Bubble Reynolds Number $[\dfrac{2r\,c_{rel}}{\nu}]$	-
Re_D	Pipe Reynolds Number $[\dfrac{cD}{\nu}]$	-
Re_u	Couette Reynolds Number (formed with peripheral velocity and clearance)	-
Re_ω	Rotational Reynolds Number $[\dfrac{\omega R^2}{\nu}]$	-
$Re_{\bar{y}}$	Throughflow Reynolds Number in annular clearance	-
s	Clearance	mm
S	Suction specific speed $[\dfrac{NQ^{\frac{1}{2}}}{E_v^{\frac{3}{4}}}]$	-
t	Disc thickness	mm
T	Relative radius $[\dfrac{R}{R_D}]$	-
ΔT	Temperature increment	K
u	Peripheral velocity	$m.sec^{-1}$
V	Volume	m^3

W	Fluid velocity relative to impeller blade	$m.sec^{-1}$
We	Weber Number $[\frac{\rho c^2 L}{\sigma}]$	-
X	Relative radius of interface in a HDS $[\frac{R_i}{R_D}]$	-
$\bar{y}$	Mean axial fluid velocity	$m.sec^{-1}$
Y	Relative shaft or hub radius $[\frac{R_h}{R_D}]$	-
Z_R	Reynolds Number correction for a venturi tube	-

α	Angle between the direction of fluid velocity and the tangent to the impeller periphery	degrees
β	Blade angle	degrees
δ	Losses in a hydraulic machine	%
Δ	Specific diameter $[\frac{D(gH)^{\frac{1}{4}}}{Q^{\frac{1}{2}}}]$	-
Δ	Increment (when used in conjunction with another symbol, e.g. Δp)	-
ζ_{io}	Flow resistance coefficient at slot inlet and outlet	-
η	Efficiency	%
θ	Slot (seal clearance) flow coefficient	-
κ	Power coefficient $[\frac{P_{in}}{\rho \omega^3 D^5}]$	-
λ	Friction coefficient for a smooth walled slot	-
λ_s	Surface roughness	$\mu m.$
λ_{CLA}	Surface roughness measured on the Talysurf	$\mu m.$
μ	Dynamic viscosity	cP
ν	Kinematic viscosity	cSt
ρ	Density	$kg.m^{-3}$
σ	Surface tension	$N.m^{-1}$
$\sigma_{(n-1)}$	Sample standard deviation (statistical analysis)	-
τ	Peripheral component of shear stress	$N.m^{-2}$
ϕ	Pump flow coefficient $[\frac{Q}{\omega D^3}]$	-
ϕ_{tot}	Total flow coefficient $[\frac{Q + Q_{Leak}}{\omega D^3}]$	-
ϕ'	Flow coefficient derived from pump flowrate + upper neckring leakage	-

ψ Pump head coefficient $[\frac{gH}{\omega^2 D^2}]$ –

ω Angular velocity $\sec^{-1}$

Subscripts

1.	Inlet conditions	N	Relating to a multistage HDS
2	Outlet conditions	N1	Relating to one stage of a multistage HDS
A	Axial flow	r	Radial component
c	Contraction	rel	Relative
crit	Critical	R	At radius R
dyn	Dynamic	s	Smooth side
D	Disc	sl	Slot (or clearance)
f	friction	ss	Single stage
F.L.	Filter loss	t	Tip
h	Hub	tap	Tapping
hyd	Hydraulic	tot	Total
i	Interface	v	Vaned side
inc	Inception	vol	Volumetric
m	Mercury	w	Water
mech	Mechanical	ω	Whirl component
		∞	Free stream

TERMINOLOGY

Abbreviations and terminology which occur frequently in the text (after initial definition) have been redefined below for the convenience of the reader.

Term	Definition
C.A.S.E.	Co-operative Award in Science and Engineering (jointly funded by the Science Research Council and an external body - normally an industrial concern)
CLA	Centre Line Average: measurement of surface roughness.
Clean mercury	Mercury which does not contain significant amounts of other chemicals (such as sodium), which would normally be found in "cell" mercury in the chlorine plant.
Gross absorbed power	Power absorbed by the pump, plus losses in shaft seals and bearings, in the right angle gearbox (on the water rig) and in the motor (O.L.R.)
HDS	Hydrodynamic Disc Seal.
I.D.	Internal diameter.
Nett absorbed power	Power absorbed by the pump (or pump/HDS assembly), i.e. gross absorbed power minus parasitic losses on the test rig as detailed in the definition above.
N.P.S.H.	Nett positive suction head, describing cavitation characteristics of the pump.
O.L.R.	Off-Load Rig (mercury test rig).
Standard pump	The original design of pump, fitted with upper and lower neckrings at standard clearance (0.165mm radial).
Water	When referring to pump trials in the present work, "water" indicates a 99% water/1% soluble cutting oil mixture. The temperatures are described as follows:

Cold water   -   at ambient room temperature (20-27°C)
Warm water   -   at 55-57°C.
Hot water   -   at 80-82°C.

LIST OF TABLES

LIST OF TABLES IN APPENDICES

LIST OF FIGURES

[followed by list of Figures included in Appendices]

LIST OF FIGURES IN APPENDICES

CHAPTER 1

INTRODUCTION

This project relates to pumping mercury and to mercury flows. It was financed by a Science Research Council Co-operative Award Scheme in Science and Engineering, with collaboration between the University of Southampton and I.C.I. (Mond Division) Research and Development Department at Winnington, Cheshire. Mercury plays a vital role in the industrial processing of brine by electrolysis for the manufacture of caustic soda and chlorine in several major plant installations at I.C.I.

The initial aims of the project, to be carried out over a three-year period, were:

(a) to investigate the characteristics of a single-entry, centrifugal pump (which is normally used to recirculate mercury in the chlorine plant) running in water and mercury and hence to modify the existing flow scaling laws so that they could be used to transfer data from one liquid to the other.

(b) to design and test a hydrodynamic disc seal (HDS) for the above-mentioned pump.

(c) to investigate the effect of varying inlet conditions on the performance of another design of mercury pump.

As a consequence of difficulties in obtaining components for the second pump, part (c) of the programme was eventually abandoned and replaced by feasibility studies of a thermometric method for measuring pump efficiency.

The principles of the industrial manufacture of caustic soda and chlorine by the electrolytic decomposition of brine in mercury cells, and the main operational requirements for the mercury pump, are described in the following chapter. The historic development of mercury pumping systems at I.C.I. is briefly surveyed, with details of the single entry pump which is currently used in one of the cell units.

The factors involved in modelling the behaviour of turbomachinery in incompressible fluids have been theoretically investigated, as a basis for subsequent experimental work.

Pump performance has been thoroughly examined on a water test rig at Southampton University and a mercury rig at I.C.I., Winnington. A method for predicting pump performance in mercury from water data has been developed from a comparison of the two sets of results, together with an investigation of pump materials and internal surfaces.

Two designs of HDS have been tested alone and as an integral part of the pump, replacing the existing upper neckring. In addition to comparative studies of pump performance with a HDS and with neckrings, dissimilarities in the operation of a HDS running alone with an applied inlet pressure rather than in the pump have been investigated. Seal performance in water and mercury is also compared.

During the final series of seal trials, when the pump was fitted with a two-stage HDS, a quartz crystal thermometer was used to monitor the minute temperature rise across the pump. The feasibility of this technique for measuring pump efficiency has been reviewed.

CHAPTER 2

MERCURY ELECTRODE PUMPING SYSTEMS AT I.C.I.

2.1 Principles of the Electrolysis of Brine in Mercury Cells

Chlorine has been produced at Runcorn, Cheshire, by the electrolytic decomposition of naturally occurring salt deposits since 1895. The Castner rocking cells were used for many years but these have now been superseded by more modern mercury cells developed by I.C.I.

All mercury type chlor-alkali cells operate on the same electrochemical principles[1,2,3]. The cell consists of two essential parts, an electrolyser and a decomposer. In the electrolyser, brine is decomposed between an insoluble anode, where chlorine gas is evolved, and a flowing mercury cathode, where alkali metal is released and dissolves to form liquid amalgam.

The principal reactions for sodium chloride are:

At the anode: $Cl^- \rightarrow \frac{1}{2}Cl_2 + e^-$

At the cathode: $Na^+ + (Hg) + e^- \rightarrow Na\ (Hg)$

Overall: $Na\ Cl + (Hg) \xrightarrow{\text{1 Faraday}} Na\ (Hg) + \frac{1}{2}Cl_2$
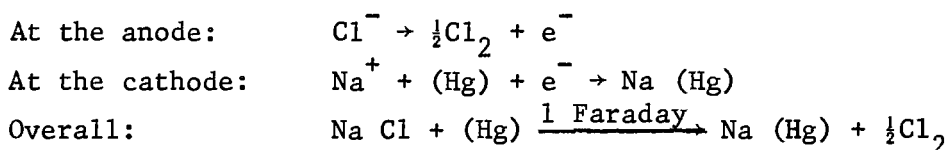
The process is rate controlled by the current density between anode and cathode.

In the decomposer, or denuder, the amalgam is decomposed with water to form sodium hydroxide and hydrogen gas, releasing mercury with low sodium content for re-use in the brine cell. The amalgam is made anodic and a cathode is provided of some material that does not amalgamate with mercury, usually graphite. Sodium is removed from the amalgam and dissolves in the water to form sodium ions, whilst hydrogen is evolved at the cathode, leaving hydroxyl ions in solution.

The electrolytic reactions in the decomposer are:

At the anode: $Na(Hg) \rightarrow Na^+ + e^- + (Hg)$

At the cathode: $H_2O + e^- \rightarrow OH^- + \frac{1}{2}H_2$

Overall: $Na(Hg) + H_2O \xrightarrow{\text{1Faraday}} NaOH + \frac{1}{2}H_2 + (Hg)$
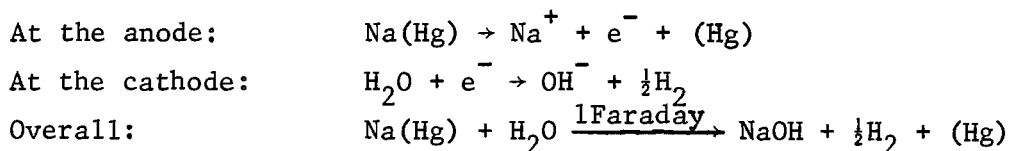
Since there is no direct connection between the brine solution in the electrolyser and the caustic solution in the decomposer, caustic produced by this method is unusually pure. The decomposer is normally operated to produce caustic liquor containing 50% NaOH.

2.2 Operational Requirements for Mercury Pumps Used in Flowing Mercury Cathode Cells

Mercury flow through a brine cell is gravity driven down the gently-sloping base-plate of the cell. It is desirable to maintain as small a gap as possible between the metal anodes and the flowing mercury cathode, but shorting between the two has to be avoided. Hence, it is essential that the turbulent mercury flow runs smoothly down the base of the cell, forming a film of constant thickness. Further difficulties in maintaining the anode-cathode gap arise from roughening of the cell base-plate, caused by the deposition and build-up of "thick mercury"[**]. This problem is reduced by regular stripping and cleaning of the cell floor. Thus it is vital that the pumps which deliver mercury to the top of the cells provide a uniform, non-surging flow. The mercury is pumped from the pump tank to a "mini-box", which holds a quantity of liquid and thereby helps to smooth out any transient surges in the flow. Mercury then flows into a "spreader box", which is designed to ensure an even spread of mercury across the width of the cell base-plate. If these two installments fail to remove the effects of any deviations in pump flowrate, waves will occur in the flow of mercury down the base-plate, with consequent shorting between anode and cathode. Surging tends to

---

[**] "Thick mercury" is a suspension of solid caustic and iron in mercury (approximately 90% mercury by volume) which forms on the base-plate and increases the cathode thickness. The solid caustic is thought to originate from entrained caustic in solution which has dried out in the cell.

be a problem during cell start-up when the mercury flow is held up on the cell base-plate, causing fluctuations in the level of mercury in the pump tank.

The minimum permissible mercury flow rate in the cell is governed by the current density, which regulates the rate of sodium deposition. Sodium concentrations in the amalgam may not rise above 0.3%, otherwise the sodium deposition potential is raised above that required for hydrogen evolution. Significant quantities (i.e. more than 1%) of hydrogen cannot be tolerated in the chlorine gas which evolves at the anode, because of the danger of explosion. Thus the mercury flow rate is controlled to give a sodium concentration of roughly 0.2% at the outlet end of the brine cell.

Mercury flow through the denuder is also gravity driven. Here the sodium concentration should be reduced to less than 0.02%, before the mercury runs into the pump tank, whence it is recycled to the brine cell.

Besides small quantities of sodium, cell mercury contains other impurities which will affect its physical properties, such as viscosity and density, and hence influence its flow behaviour (see Chapter 3.1). A second factor to be considered is the heat liberated by reactions in the cell, which causes a temperature gradient in the mercury flowing down the cell baseplate (typical figures would be $50^{\circ}C$ at the inlet and $75^{\circ}C$ at the outlet to the cell[3]). Thus, although the cell mercury will be cold at start-up, under normal operating conditions the pumps will be delivering fluid at elevated temperatures (see Chapter 3.1).

The required delivery head from the pump is determined by the static lift between the pump sump tank and the spreader box at the top of the cell, plus the frictional losses in pipework, etc.

The formation and build up of thick mercury on the cell base plate constitutes a major operational difficulty. Since this deposit is thought to originate from entrained caustic solution, it is imperative

to avoid entrainment of wash water, which inevitably contains some caustic, through the pump.

In addition, the pumps must be mechanically reliable, so that down time for maintenance is kept to a minimum. Maintenance costs are increased by loss of production during periods when cells are out of action for pump repairs.

Thus, the special mercury pump requirements can be summarised as follows:

(a) Mechanical reliability.
(b) Flow stability. This includes lack of surges during start up, as well as fluctuations in flow rate during normal operation.
(c) Avoidance of water entrainment.

2.3 The Development of Mercury Electrode Pumping Systems at I.C.I.

Details of the historical development of pumps by I.C.I. and other mercury cell operators are contained in reference [4].

The original I.C.I. pumps were of the inclined Archimedian screw type, consisting of a continuous helical screw enclosed in a barrel. However, this design was only suitable for a lift of 0.24m and delivered mercury at low, non-uniform flow rates ($6\ell.min^{-1}$ max.).

This pump was developed into a more compact, vertical arrangement in 1938, with a vertical helical screw attached to the extended shaft of a 3 phase motor. The maximum lift was increased to 0.3m with flow rates of up to $11\ell.min^{-1}$. However, the efficiency was estimated at only 2.5% and severe agitation was found to occur at the helical screw inlet and exit due to the high rotational speeds involved.

In 1944/45, a rotating barrel pump was introduced. Although this proved mechanically reliable and capable of delivering a maximum

flow rate of $45\ell.\text{min}^{-1}$ at 0.36m head, severe agitation of mercury occurred at the barrel entry and exit, whilst fluctuations in delivered flowrate constituted another disadvantage. Thus the design was considered unsuitable for further development.

The first centrifugal pumps were installed in 1952. The performance of these pumps had previously proved satisfactory when they were operating in another plant, under the conditions for which they were designed ($37\ell.\text{min}^{-1}$ at 2.1m head of water). However, in the mercury cells, the pumps were operating against an insufficient system resistance, so the flowrate was much higher than specified, causing a significant fall in the level of mercury in the pump tank. As a result of inadequate pump immersion, the delivered flowrate was surging with entrainment of weak caustic and water.

Other experimental pumps have undergone trials in the past and been rejected as unsuitable for use in the mercury cells. These include bucket elevators, air and steam powered gas lift pumps and electromagnetic pumps. Of these, only the D.C. powered electromagnetic pump appeared potentially attractive, but it required a great deal of development. This type of pump is used for sodium-potassium duty in some nuclear applications[5].

By 1964, vertical centrifugal pumps were favoured by the majority of mercury cell operators, such as Solvay et Cie (Belgium), de Nora (Italy) and Mathieson (USA). However, the Kureha Chemical Industry Co.Ltd. (Japan) were still using a simple circular bucket wheel. This machine was reliable and efficient, but it compared unfavourably with the centrifugal type pumps, due to high cost and large size.

In 1963, plans were made by I.C.I. to uprate the existing mercury cell units so that they would operate at higher current densities. This necessitated increasing the flowrate of mercury in the cell, by using a steeper cell base-plate. As a result, the required

duty of the mercury pumps was increased with respect to both flowrate and differential head.

To meet this requirement, a new centrifugal pump (basically a water pump design) was developed in conjunction with Manufacturer A. A design flowrate of $40\ell.\text{min}^{-1}$ with a total differential head of 1m at a rotational speed of 720rpm (to suit the existing extended shaft motors) was specified. After successful preliminary test rig trials, the new centrifugal pumps were installed on all increased slope cells.

2.4 Current Mercury Pumping System

At the present time, a single entry centrifugal pump is used to maintain the circulation of mercury in one of the works units manufacturing caustic soda at I.C.I. A diagram of the pump, supplied by Manufacturer A, is presented in Figure 1. It consists of a double shrouded impeller and volute, keyed onto the vertical extended shaft of a 2.6kW (3.5HP) 40 volt 3 phase induction motor. This low voltage motor is used to reduce the likelihood of sparking and consequent danger of explosion in an atmosphere which may contain small quantities of chlorine and hydrogen.

Details of the pump and impeller may be found in Appendix I. The design flowrate is $55\ell.\text{min}^{-1}$, producing a differential head of 5.9m (19.5ft) and absorbing 2.4kW power (3.2HP).

The Euler equation may be used to calculate the theoretical runner head H_r which would be developed by the pump without losses.

$$H_r = \frac{1}{g} (u_2 c_{\omega 2} - u_1 c_{\omega 1}) \qquad \dots \text{(2.1)}$$

For a pump operating at its design point, it is usual to assume that the whirl component of the fluid velocity is zero at the pump inlet,

i.e. $c_{\omega 1} = 0$.

The Euler equation then reduces to :

8.

$$H_r = \frac{1}{g} u_2 c_{\omega 2} \qquad \qquad \ldots \text{(2.2)}$$

When the pump is operating at its design point, $u_2 = 10.86 \text{m.sec}^{-1}$ and $c_{\omega 2} = 8.09 \text{m.sec}^{-1}$.

Substituting these values in equation (2.2) we obtain

$$H_r = 8.96 \text{m.}$$

In practice, the pump produces a head of 5.9m at its design point, which corresponds to a hydraulic efficiency of 66%.

In order to check the validity of the assumption that the fluid whirl component is zero at the pump inlet, the direction of the fluid velocity relative to the runner was calculated, presuming purely radial inlet flow. This calculation gives a relative fluid inlet angle of 11°. With a vane angle of 21°, high shock losses would result.

It is possible that the inlet vane angle was chosen to be compatible with a certain amount of prewhirl. For minimum shock losses (fluid flow parallel to the vanes at inlet), the prewhirl component of fluid velocity ($c_{\omega 1}$) would be 1.66m.sec^{-1}.

Substituting $u_1 = 4.33$, $u_2 = 10.86$, $c_{\omega 1} = 1.66$, $c_{\omega 2} = 8.09$ into the full Euler equation, we obtain:

$$\underline{H_r = 8.22 \text{m.}}$$

When this theoretical value is compared with the actual head of the pump at its design point (5.9m) the hydraulic efficiency is 72%. Full details of the calculation of the separate terms in the Euler equation are contained in Appendix II.

Operation of the pumps in the caustic plant involves a static lift of mercury between the pump tank and mini-box of 3.1m. Calculated head losses in the system, due to bends, valves and pipe friction,

increases the nett head required at the design flowrate to 4.0m.
(B. Heald, personal communication, Nov.1976). The kinetic energy
of mercury is largely dissipated in the mini-box and spreader box.
The value of the kinetic head $(\frac{c^2}{2g})$ is 0.05m at the design flowrate,
which is insignificant in comparison to the static head and head
losses in the system. During cell operation, the pump flowrate is
manually controlled to suit specification, using a ball valve.

The specific speed $(n_s = \frac{\omega Q^{\frac{1}{2}}}{(gH)^{\frac{3}{4}}})$ and specific diameter $(\Delta = \frac{D(gH)^{\frac{1}{4}}}{Q^{\frac{1}{2}}})$
of the pump have been calculated by the present author. At its design
point:

$$n_s = 0.22$$

$$\Delta = 13.0.$$

Figure 2 shows the empirical relationship between specific speed
and specific diameter for existing pumps of conventional design and of
proven efficiency[6]. The point for the mercury pump under investigation
lies very close to the empirical curves.

2.5 Shortfall in Pump Performance

The impeller of the pump is sealed into its casing by an upper
and lower neckring. The standard radial clearance between the neckring
and impeller is 0.165mm but this clearance increases through wear and
often exceeds .75mm before the pump is taken out of service for mainten-
ance. The main reason for wear is thought to be abrasive particles,
which are forced into the annular space between the impeller hub and
neckring. Opinion at I.C.I. favours graphite spheres which have escaped
in the mercury flow from the denuder as the main source of such particles,
but an investigation of pump materials by the present author suggests
this is unlikely (see Chapter 8.2.1).

Mercury leakage through the increased neckring clearance of a
badly worn pump has been estimated by the pump manufacturers at roughly
30% of the delivered flow. The mercury then jets out of the holes in

pump shaft casing (see Figure 1) and is recycled through the pump,
causing a large amount of turbulence in the pump tank. This in turn
causes high wash water and caustic entrainment through the pump,
which is thought to contribute substantially to the formation of
thick mercury.

Pump performance is also affected by neckring wear, as shown
in Figure 3. These curves were produced by the pump manufacturer using
cold water as the test liquid, and show that increased seal clearance has
a more pronounced effect on the N.P.S.H. than on the delivered head.
This is because leakage from the lower neckring is discharged directly
into the pump inlet (see Figure 1). Initially this was thought simply
to restrict the available area for fluid entering the pump, thereby
causing higher inlet velocities with consequent reduction of inlet
pressure (conditions which favour cavitation), but recent research has
shown that the effects of leakage on pump pressure generation are more
extensive (see Chapter 5.5).

Pump failures in the plant due to excessive neckring wear amount
to approximately 40 per year, with 1 fitter employed almost full-time
on removing and refurbishing pumps.

2.6 Recent Developments of the Current Pump Design by I.C.I.

Various ideas have been put forward to improve the performance of
the pump by reducing or eliminating leakage of mercury through the neck-
rings. As a result, the delivered flowrate from the pumps should not
drop off so significantly with cumulative running time, the mechanical
reliability and efficiency of the pumps should be improved and water
entrainment should be reduced.

(a) Back-vaned impeller (see Figure 164a).

A shrouded impeller incorporating backvanes, to form a hydro-
dynamic seal[7] on the top side of the pump was designed for the pump[8].
This would reduce the pressure on the top neckrings, preventing foreign

11.

bodies from being forced into the annular space between the neckring and impeller hub and thus reduce wear. There would also be a substantial reduction or even total removal of the amount of mercury being recycled through the top neckring. However, the lower neckrings would be unaffected and because of their larger diameter (and hence the higher relative velocity of contact surfaces) they were thought to contribute more to loss of pump performance than do the upper neckrings[9]. The back-vaned impeller would consume more power, so the present motor would require an increased power rating, unless a considerable increase in overall efficiency could be achieved. This idea was shelved[9] whilst more promising modifications were tested.

(b) Open impeller

The feasibility of an open impeller design for the pump has been investigated[9]. This would have the advantage of total removal of the neckrings, since a hydrodynamic shaft seal was envisaged. The seal would have to be effective against pressures only a little above suction and hence the extra power absorbed would be small (about 0.15kW). However, wear between the open impeller and wear plates positioned above and below it (caused by axial and/or radial movement of the impeller) would probably occur more rapidly than the present neckring wear, because the peripheral velocity between the wearing surfaces (impeller and wear plates) would be higher than that between impeller hub and neckrings. The associated problems of churning and water entrainment have been discussed in Section 2.5.

(c) Other

Suggestions have been put forward by I.C.I. to pump manufacturer B for trials with ceramic-coated neckrings and impeller hubs.

Manufacturer B also suggested tests using wind-back helical grooved neckrings, since they have been successful in other applications. However, they would be unsuitable for use on the mercury cell pumps,

since they require small radial clearances and would thus be sensitive to particles in the mercury.

No recent trials have been carried out in either of these areas.

CHAPTER 3

FACTORS INVOLVED IN MODELLING THE PERFORMANCE
OF TURBOMACHINERY IN INCOMPRESSIBLE FLUIDS

The use of geometric scaling for predicting the performance of prototype turbomachines, by testing small scale models, has long been established[10]. However, it is not yet clear how data collected from tests on turbomachinery with water can be used to predict performance with fluids of different physical properties.

The problem of pumping viscous fluids and predicting pump performance under these conditions on the basis of tests carried out with water has been of major importance for both the petroleum and chemical industries[11]. All available data in this field applies to fluids of higher viscosity than water[12,13,14]. Pantell[15] used the experimental data from Stepanoff's book[16]* to develop a theoretical method for predicting pump performance in oil from water tests, but this method is only valid for viscosities greater than 180 cSt. The present author has been unable to trace any work relating to pump performance in fluids of low kinematic viscosity, e.g. Naphtha, petrol, hot water, or mercury.

Hence, the initial stages of the present project involve comprehensive tests on identical pumps running in water and mercury, in order to test the validity of the existing flow scaling laws for the transference of data from one liquid to another.

In this chapter, the main parameters relating to pump performance scaling between water and mercury are discussed.

14.

* 1st Edition (1948)

3.1 Dimensionless Groups

If Reynolds Number and surface roughness effects are neglected, for similar flow conditions to occur in two geometrically similar pumps delivering water and mercury respectively, the head coefficient Ψ and flow coefficient Φ must be the same in both cases. That is:

$$\Psi_w = \Psi_m \qquad \qquad \ldots (3.1)$$

$$\Phi_w = \Phi_m \qquad \qquad \ldots (3.2)$$

where $\quad \Psi = \dfrac{gH}{\omega^2 D^2} \quad$ and $\quad \Phi = \dfrac{Q}{\omega D^3}$.

In the present case, the same pump is to be used for both liquids, i.e. $D_w = D_m$. Thus:

$$\frac{H_w}{H_m} = \left(\frac{\omega_w}{\omega_m} \right)^2 \qquad \qquad \ldots (3.3)$$

and

$$\frac{Q_w}{Q_m} = \left(\frac{\omega_w}{\omega_m} \right) \qquad \qquad \ldots (3.4)$$

However, the kinematic viscosity (ν) of mercury is unusually low, so that the Reynolds Number for water flow will be much lower than for mercury flow at equal velocity. We must therefore stipulate equality of Reynolds Numbers.

The specific speed of the pump ($n_s = 0.22$)[*] is appropriate for a relatively high head/low flow centrifugal pump. This justifies the equating of the rotational flow Reynolds Numbers rather than the pipe flow Reynolds Numbers, i.e.

$$\frac{\omega_w D_w^2}{4\nu_w} = \frac{\omega_m D_m^2}{4\nu_m} \qquad \qquad \ldots (3.5)$$

or

$$\frac{\omega_w}{\omega_w} = \frac{\nu_w}{\nu_m} \qquad \qquad \ldots (3.6)$$

[*] Based on experimental data from the present research (Figures 15-20), at η_{max} , $n_s = 0.35$

The kinematic viscosity of mercury varies by less than 10% in the temperature range 20-100°C, but that of water is more variable, as shown in Figure 4.

The maximum temperature that can safely be accommodated in the water rig at Southampton is 75°C. Thus we chose a ratio of $\frac{v_w}{v_m} = \frac{0.4}{0.11} \simeq 4$. Substituting in equation (3.6) we obtain:

$$\omega_w = 4\omega_m \qquad \qquad \ldots (3.7)$$

The mercury pumps in the caustic plant run at 1450 r.p.m. hence, for similarity conditions, the pump on the water rig must run at 5800 r.p.m. For a typical mercury flow of $55 \, \ell.min^{-1}$, the water flow will be $220 \, \ell.min^{-1}$, and from equation (3.3) the head rise for water will be 16 times the head rise for mercury. The pressure rise across the pump (Δp) is given by:

$$\Delta p = \rho g H \qquad \qquad \ldots (3.8)$$

(where ρ = density of fluid in pump).

Then

$$\frac{\Delta p_w}{\Delta p_m} = \frac{\rho_w \omega_w^2}{\rho_m \omega_m^2} = 1.16 . \qquad \ldots (3.9)$$

This means that the water pressure rise will be 1.16 times the mercury pressure rise. If Re_w is a little below Re_m, the mercury and water rigs will be run with the same pressure rise across the pumps, so that mechanical loadings on components will be approximately equal.

The input power to the pump operating in clean mercury at its design point is 2.5kW. To estimate the input power to the pump when operating under similarity conditions on the water rig, we assume that the power coefficients (κ) are equal in both cases, i.e.

$$\kappa_w = \kappa_m \qquad \qquad \ldots (3.10)$$

(where $\kappa = \dfrac{P_{in}}{\rho \omega^3 D^5}$)

Since $D_w = D_m$,

$$\frac{P_{in_w}}{P_{in_m}} = \frac{\rho_w \omega_w^3}{\rho_m \omega_m^3} = 4.66. \qquad \qquad \text{... (3.11)}$$

Then $P_{in_w} = 11.6 \text{kW}.$

This power demand slightly exceeds the nominal capability of the water rig motor (see Chapter 5.1).

It is also desirable that thermal expansion and distortion should be equal on the water and mercury rigs. Vapour hazards dictated that the mercury test rig should not be run above 55°C so this condition could not be totally met.

The above discussion is based on a comparison between water and clean mercury as pumping fluids. It is worth noting that mercury used in the chlorine plant is impure. Previous tests by I.C.I.[17] have shown that the flow behaviour of cell mercury differs considerably from that of pure mercury at room temperature. Physical properties of the mercury such as density and viscosity will be affected by (a) the presence of impurities and (b) the operating temperature of the cells[18]. However, no work was done using cell mercury during the present project and details of such variations, which are fully described in Reference 18, have been omitted.

3.2 Surface Topography

The influence of surface texture on pump performance has been acknowledged by several workers[19,20,21,22] and may be particularly relevant to the present project if there is a difference in roughness between the flow surfaces of the two pumps on the water and mercury rigs. In addition, it is thought that the low kinematic viscosity of

mercury will make mercury flows more sensitive to surface irregularities than water flows through the same equipment at the same volumetric flow-rate.

Most work regarding friction losses of fluid flows through pipes or across plates is based on a uniformly rough surface, such as the artificially sand-roughened pipes of Nikuradse[23]. However, extensive research by Millionschchikov et al[24] and Schlichting[25] has shown that the roughness profile and spacing also affects friction losses, particularly in the transition region between hydraulically smooth and fully rough surfaces. Furthermore, the resistance of wavy or grooved surfaces varies with the direction of the fluid flow.

The accepted laws of surface friction cannot be applied directly to turbomachinery. Here one has to consider the roughness of each section of the machine with respect to flow direction. The channels are curved and varying in cross-section, whilst the flow is non-uniform and unsteady, often tending to separate. These concepts emphasise the difficulty of developing a valid scaling law which embraces all the relevant parameters.

Nixon and Cairney[19] investigated the effect of surface rough-ness on the performance of centrifugal pump models and their results have been used in the present report (see Chapter 5.2.1) for estimating the transition between smooth and fully rough flow regimes. Bobok[22] obtained correlations between head loss coefficient, wall roughness and Reynolds number, producing curves of similar shape to those for pipe friction losses[23] except that the transition dip is absent. Oster-walder[20] found there was a linear relationship between runner disc losses and rotational Reynolds Number for a given value of surface roughness, the losses increasing with surface roughness. However, all these investigations are concerned with the "technical roughness" of surfaces and the effect of the shape or spacing of surface irregularities is not mentioned.

In an attempt to assess the effects of surface roughness on pump performance for the present project, topographical measurements

have been carried out on the pump impeller flow surfaces. In addition, standard metallographic techniques were used to investigate the cause and extent of material wear during normal in-plant operation, with its consequent effect on the mercury flow characteristics.

3.3 Reynolds Number Effects

Secondary effects due to changes in Reynolds Number between model and prototype turbomachines have been studied in detail by Osterwalder[20,26]. By defining the separate loss components in a radial pump, he investigates the Reynolds Number effect on those which can be scaled up. Friction losses of the flow guiding surfaces, disc friction losses, some of the diffuser losses and leakage losses belong to this category. Shock losses, most of the energy conversion losses in the diffuser, losses due to sudden area changes and friction losses for fully rough surfaces cannot be scaled. Osterwalder's results[26] show that the scale effect depends on the manner in which the Reynolds Number is altered, i.e. by speed or by a change in fluid viscosity. Since this discovery is of particular relevance to the present project, it is unfortunate that he does not present a detailed analysis of his data.

The effect of scaling on model and prototype turbomachinery performance has also been studied by Fay[21]. He assesses the accuracy of the Hutton scaling formula :

$$\frac{\delta}{\delta_o} = 1 - B + [\frac{Re_o}{Re}]^{\frac{1}{\gamma}}$$

where δ and δ_o refer to hydraulically smooth prototype and model respectively and standard values for the constants are taken as $B = 0.7$ and $\gamma = 5$. As a result of his analysis, Fay extends the above formula to machines which are not hydraulically smooth, by the addition of roughness correction factors.

In the present project, the pump was tested in water over a wide range of speeds and water temperatures, so that variations in performance due to changes in Reynolds Number could be examined.

CHAPTER 4

DEVELOPMENT OF WATER TEST RIG AT SOUTHAMPTON UNIVERSITY

4.1 Mechanical Layout

The water rig at Southampton was previously used for tests on
hydrodynamic disc seals in particle laden liquids[27]. The original layout
is described in Reference 18, but this has been modified substantially
to suit the present programme of pump trials.

The new design for testing the standard pump is illustrated in
Figures 5 and 6. The drive is provided by a 19kW 3 phase motor, which is
connected via a Dynadrive variable slip magnetic coupling with DX/C
control equipment to a 3.6:1 step-up toothed belt drive. An Autoguard
torque limiter manufactured by GIB Precision Ltd., which can be set to
disconnect the drive at any given torque up to a maximum of 28.5 Nm
(250lb.in) has been installed in the output shaft, to protect the torque
transducer (see Figure 7). The sixty-toothed gear wheel and magnetic
pick-up, which measures shaft speed, has been fitted between the torque
limiter and torque transducer, so that there is an immediate indication
if the torque limiter has disengaged. The transducer shaft is connected
to the drive shaft with Turboflex flexible metallic couplings, which
allow for angular and axial misalignment. Full details of these mechan-
ical components are set out in Appendix IIIA.

In order to simulate conditions in the plant at I.C.I. where the
pump is driven from a vertical shaft, the output from the horizontal
drive shaft on the water rig is turned through 90° by a spiral bevel
gearbox. Torque absorption in the gearbox, due partially to churning
of the Hypoid 90 lubrication oil, was found to be excessive and highly
temperature dependent. Therefore during the initial stage of experimental
work, the gearbox temperature was monitored by a Zeatron thermister probe

so that the parasitic torque could be estimated from a series of torque/speed curves for the rig operating in air without an impeller at various gearbox temperatures (see Appendix IV). However, this method was not totally satisfactory, particularly at low values of nett torque. Hence, a circulatory system of gearbox lubrication was designed, with a drip feed of oil (see Figure 8a) from a positive displacement pump onto the gear teeth and bearings and a scavenge pump fitted to drain holes at the bottom of the box, to ensure that the level of oil inside is kept to a minimum (Figure 8b).

With the new arrangement, the power absorbed at a given speed and gearbox temperature was reduced, together with the rate of heat evolution. However, because the gearbox was running cooler, torque absorption was still excessive, particularly at slow speeds. Further refinements, such as external heating of the oil, proved unsuccessful and for the remainder of the project, parasitic torque was estimated from a new set of torque/speed curves (Appendix IV) obtained by running the rig in air as before.

The output shaft from the gearbox is connected via an air bearing (which has the advantage of minimal torque requirements) to a stub shaft carrying the pump impeller. These components were dynamically balanced before assembly. The bearing is contained within a hollow steel cylinder, as shown in Figure 6, which also supports the pump body at its lower end. Unfortunately, the position of the bearing directly below the gearbox caused a major problem, when oil which had leaked from the box seeped into the air exhaust ports with subsequent seizure of the bearing. A new, identical bearing was fitted, with tubes attached to the exhaust ports leading out of the cylindrical support tube, to prevent the recurrence of a similar disaster. The specified air supply to the bearing is 80 psi. However, initial runs indicated that the pump neckrings were occasionally rubbing due to radial deflection of the shaft at speeds of 3000 r.p.m. and above, so the supply pressure was raised to 120 psi, in order to increase the radial stiffness.

4.2 Hydraulic Circuit

Figure 9 illustrates part of the hydraulic test circuit, which is laid out schematically in Figure 5. Water from the pump volute is delivered via a 38mm (1.5in) I.D. steel pipe to a 100 mesh filter. A 3m length of 25mm (1in.) I.D. pipe leads to the turbine flowmeter. Water is returned to the tank via a loop of 50mm (2in) I.D. pipe, with the flowrate controlled by a manually operated diaphragm valve. A bypass pipe of 25mm (1in.) I.D. has been installed, incorporating a second diaphragm valve, for ease of control at low flowrates. The test circuit has been kept as simple as possible in order to minimise the system resistance, permitting investigation of the high flowrate/low head generation pump characteristics. Water returning to the tank leaves the hydraulic circuit via a distribution manifold running along the bottom of the tank at the opposite end to the pump. This arrangement was designed to ensure minimal turbulence within the tank, particularly near the pump inlet.

The temperature of the water may be varied using two 3kW domestic water heaters fitted on either side of the pump at the bottom of the main tank. One heater, thermostatically controlled, is used to maintain a given temperature to within $2^{\circ}C$ during tests, whilst the second, manually operated heater is available for a faster heat-up. The whole hydraulic circuit is thermally insulated for high-temperature runs.

A secondary tank is installed for measuring upper neckring leakage (see Figure 10). Water which has leaked past the upper seal collects in the steel cylinder supporting the pump body. Two 25mm (1 in) I.D. pipes (clearly visible in Figure 11) leading from diametrically opposed holes in the cylinder wall, conduct the fluid to two two-way valves, where the flow may be diverted either into the secondary tank or back into the main tank. A calibrated sight glass on the side of the

secondary tank facilitates measurement of the leakage volume during a given time interval.

Since most of the pipework is fabricated from mild steel, it was necessary to use a rust inhibitor in the water. Initially Bryto No.5 was added to a concentration of 1%, but this reacted with the galvanized tank, forming a sediment which blocked the water filters. A 1% solution of soluble cutting oil proved more satisfactory, although it tended to separate with time and carburized on the heater elements during high-temperature runs. The oil was found to change the viscosity of the water by less than 0.1%.

During the latter stages of the research programme, two hydro-dynamic seals were tested both individually and in conjunction with the pump. The only modification required to accommodate the seals onto the rig was the fabrication of a new extended stub shaft below the air bearing, to carry the seal and pump impellers, and an extension of the pipework connected to the pump outlet. The rig assembly for pump and two-stage hydrodynamic seal trials is shown in Figure 11.

Individual seal performance was investigated by removing the pump from the rig, thus disconnecting the main hydraulic circuit, and replacing it with a hollow steel cylindrical block. The internal dimensions of the block were identical to that part of the pump casing which joins the seal during normal operation, with the pump and seal combined. Variable water pressure, up to a maximum of about 9.8m of water (mains pressure), could be applied to the seal entrance via a length of reinforced tubing leading from the bottom of the steel block, through a constant pressure device (Flostat valve) to the mains supply. This arrangement is illustrated in Figure 12.

The hydraulic circuit required further slight modification to suit the thermometric efficiency measurements (see Chapter 13). Initial

24.

trials indicated severe temperature fluctuations at the pump inlet, which were attributed to turbulence within the pump tank. These fluctuations were suppressed to a large extent when a wire mesh was fitted across the tank, between the pump inlet and the return pipe from the hydraulic circuit.

4.3 Instrumentation

Figure 13 shows the instrument panel on the test rig. During pump and seal performance trials, the following parameters were measured:

(i) Torque

A new torque transducer comprising a strain gauged shaft and sliprings was purchased from British Hovercraft Corporation after the original transducer failed under excess load (thought to have been caused by rubbing of the pump neckrings). The working range of the new transducer is 0-10,000 r.p.m. and 0-20Nm. The old analogue display was also replaced by a digital readout system with a bridge power supply and amplifier of superior stability.

(ii) Shaft Speed

Shaft speed was measured by a sixty toothed gear wheel on the drive shaft, in conjunction with an electromagnetic pick-up and Dawe counter. A digital readout is presented in r.p.m. with the speed controlled by a Dynadrive feedback unit.

Some problems were encountered in maintaining the required speed during tests. These were traced to:

a) vibration of the electromagnetic pick-up which was sending false signals to the feedback unit,

b) poor contact of the Dynadrive brushes caused by dirt and/or slight run-out of the tacho-generator shaft.

(iii) <u>Flowrate</u>

The turbine flowmeter.was manufactured by AOT Flo-meters of
Andover. A digital display gives direct readout of volumetric flowrate
in $\ell.min^{-1}$. The advantages of this type of meter include a high
attainable accuracy ($\pm$0.25%) and low sensitivity to viscosity changes.

(iv) <u>Pressure</u>

Initially there were four pressure tappings on the rig, situated
at the pump outlet, the upper and lower neckrings, and inside the
cylindrical support tube, near the exhaust of the air bearing. Additional
tappings were needed during seal performance trials, in order to monitor
the radial pressure distribution across the upper surface of the seal
discs and these are visible in Figures 11 and 12. The tappings were
led via three six-way Drallim valves to a precision Bourdon gauge
reading to 500 psi. Leakage of the Drallim valves occasionally caused
problems with the accuracy of pressure measurements (see Appendix IV).

The diameter of the final 1cm length of all tappings was 1mm,
with square edges at the point of emergence, to minimise errors due
to dynamic pressure sensing[28]. Extreme care was taken to avoid
blemishing the internal pump surfaces during drilling, as this might
disturb the normal flow patterns during pump operation.

(v) <u>Temperature</u>

The gearbox running temperature was measured by a Zeatron
thermister probe inserted just inside the box. The analogue display
unit, comprising eight channels, covers the temperature ranges 10-80°C
or 80-150°C.

A Hewlett-Packard quartz crystal thermometer was used during
the final stages of the research programme to measure the increment in
temperature across the pump, as an indication of pump efficiency. One
temperature probe was located in the 38mm I.D. pipe above the pump

outlet (see Figure 9), where it was used initially to monitor the
temperature of the pumping fluid. A second probe was sealed inside a
length of polythene piping, to protect its connecting cable (which is
not totally waterproof), with just the tip of the probe protruding.
This pipe could then be immersed in the pump tank, so that the probe
was located as close as possible to the pump inlet.

The quartz thermometer gives a direct digital readout of
temperature or of temperature differences to 10^{-4} °C.

Full details of the water test rig and instrumentation,
including types and serial numbers, are contained in Appendix III and
the accuracy of experimental measurements is discussed in Appendix IV.

CHAPTER 5

MEASUREMENT AND ANALYSIS OF PUMP PERFORMANCE IN WATER

5.1 Experimental Procedure

Extensive trials were carried out on the pump with standard neckring clearances (0.165mm radial), running in a 1% soluble cutting oil in water solution (Chapter 4.2). The tests were performed over as wide a range of speeds as possible, in order to achieve a significant variation in rotational Reynolds Number. Although the static head of the hydraulic circuit (∿3.0m) exceeded the delivery head of the pump at speeds of 1000 rpm and below (Figure 15), steady flowrates could still be maintained by a siphon effect down to 600 rpm.

Originally it was planned to test the pump up to a speed of 5,800 rpm, which would involve a power consumption of 11.6kW (Chapter 3.1). The power available from the rig is limited by the magnetic coupling, which is rated at 68Nm (50ft.lb). This torque is reduced by a factor of 3.6 at the step-up toothed belt drive, so that the maximum available power at 5,800 rpm is:

$$\frac{68 \times 2 \times \pi \times 5800}{3.6 \times 60} = 11.5 \text{ kW.}$$

If parasitic torque absorbed by the gearbox is taken into account it is unlikely that the test rig motor and coupling would have been capable of driving the pump at 5,800 rpm.

In practice, the maximum attainable speed on the rig was found to be 3,500 rpm. At this speed, with the flow control valves almost closed, the asymmetrical pressure distribution within the pump volute caused deflection of the stub shaft below the air bearing, which induced rubbing

of the neckring seals. The resultant torque was high enough to activate the torque limiter, set at 16Nm. Thus several of the high speed runs were incomplete.

A further variation in rotational Reynolds Number was achieved by altering the temperature of the pumping fluid. Tests were carried out at room temperature ($25\text{-}28^{\circ}C$), $56^{\circ}C$ and $81^{\circ}C$, the latter being the maximum temperature that the water heaters could maintain.

During a run at a given speed and water temperature, readings were taken of the delivery pressure, upper and lower neckring pressures, gross torque absorbed and gearbox temperature for a series of flowrates ranging from zero to the maximum attainable. The leakage rate at a given delivery flow was measured by diverting water which had leaked from the top neckring into the secondary calibrated tank during a known time interval, as explained in Chapter 4.2. The nett torque absorbed by the pump was found by subtracting the parasitic torque, read off from the curves in Appendix IV, from the gross torque. The input power to the pump itself was then calculated from the product of the nett torque and rotational speed (in radians per second) i.e.

$$P_{in} = \frac{2\pi nM}{60} \qquad \dots (5.1)$$

The hydraulic output power of the pump is:

$$P_{out} = \rho gQH \qquad \dots (5.2)$$

The overall pump efficiency is then:

$$\eta = \frac{P_{in}}{P_{out}} \times 100\% \qquad \dots (5.3)$$

If the head, flow and power absorption data obtained at each speed and water temperature is converted into a non-dimensional form, all points should collapse onto common dimensionless head and power

curves, providing that secondary factors such as Re effects are absent.
The dimensionless parameters characterising pump performance are:

a) Head coefficient $\quad \psi \quad = \quad \dfrac{gH}{\omega^2 D^2}$ $\qquad$ ... (5.4)

b) Flow coefficient $\quad \phi \quad = \quad \dfrac{Q}{\omega D^3}$ $\qquad$ ... (5.5)

c) Power coefficient $\quad \kappa \quad = \quad \dfrac{P_{in}}{\rho \omega^3 D^5}$ $\qquad$ ... (5.6)

In subsequent experiments, the pump performance was evaluated
with the impeller hub machined down to give a radial seal clearance of
(a) 0.318mm (0.0125in) and (b) 0.635mm (0.025in). The intention was to
simulate the characteristics of the pump running in a worn condition
and to investigate the effects of increased leakage rate on overall
pump performance. In addition to decreasing the volumetric efficiency,
it was felt that fluid leaking past the lower neckring could cause
disturbed flow conditions at the impeller inlet, thereby influencing
the hydraulic efficiency (see Figure 1).

The readings taken during these tests with increased seal
clearance were identical to those taken during tests on the standard
pump. The rotational speed was varied between 600 and 3000 rpm, with
the water at room temperature $(25-28^{\circ}C)$.

5.2 Characteristic Performance Curves of the Standard Pump

The characteristic dimensional head, absorbed power and efficiency
curves for the pump operating at various speeds and water temperatures are
presented in Figures 14-20. Absorbed power and efficiency data has been
omitted from Figure 14, since the torque absorbed by the gearbox at 600 rpm
amounted to more than 75% of the gross measured torque, leading to an
unacceptably high uncertainty in the value of nett torque absorbed by

the pump. The curves of Figure 20 are also incomplete. This is
because the torque limiter was activated at high rotational speeds and
low flowrates, as explained in the preceding section.

5.2.1 Head Characteristics

The fairly flat head/flow curves exhibited at all speeds are
typical of a low specific speed pump (n_s=0.22, see Chapter 2.4) with
a large discharge vane angle of 33° and five vanes. The pump has a
stable, falling head characteristic under all conditions tested.

Outlying points at maximum flowrate on the head curves in
Figures 19 and 20 suggest that these flowrate measurements are inaccurate,
due to cavitation at the turbine flowmeter (which will cause the
instrument to over-read). A pressure tapping was subsequently fitted
at the meter as a check, and although high speed runs at elevated
temperatures had been discontinued by this time (as a safeguard for
the air bearing and torquemeter), the recorded pressure drop between
the pump and meter at the maximum available flowrate confirms that
cavitation would be likely, if the fluid velocity and/or water
temperature were further increased (see Appendix IV).

The estimated maximum error in pump head measurement is $\pm$15% at
1000 rpm and $\pm$40% at 600 rpm (see Appendix IV). Test results at these
speeds have been presented throughout the thesis for interest, but are
usually omitted from the discussions because of their poor accuracy.

Figures 16-19 show that the pump delivered head decreases slightly
as the water temperature is raised. The trend disappears at 3,500 rpm
(Figure 20), although data collected at this speed is rather limited,
particularly at 81°C water temperature. Reasons for this phenomenon
are examined below, in relation to the dimensionless head characteristics.

The head/flow measurements have been plotted in a non-dimensional
form for each water temperature (Figures 21-23). At 56°C and 81°C, the

31.

data falls onto a single common curve, with only slight scatter, which is mainly attributable to (a) experimental error at low rotational speeds and (b) cavitation at the flowmeter for maximum flowrates, as discussed above. At 25°C, the scatter of points is wider, with data collected at the higher speeds (3,000 and 3,500 rpm) falling slightly below the main curve. Apart from this disparity, a change of rotational speed at a given water temperature does not effect the pump head characteristics.

However, the head characteristic, is altered by a change in water temperature, as illustrated in Figure 24a. Since seal leakage also depends upon water temperature, as shown below in Section 5.3, it was felt that the lower head characteristics in hot water might be a direct result of increased leakage losses. Therefore, a total flow coefficient, based on the total fluid flow through the pump impeller (i.e. delivered flowrate + leakage) has been defined as:

$$\phi_{tot} = \frac{(Q + Q_{leak})}{\omega D^3} \qquad \ldots (5.7)$$

Two representative speeds were chosen for each water temperature to plot the dimensionless head/total flow characteristics, see Figure 24b. Since the pump head characteristics at each temperature still differ, an alternative explanation for this change in pump performance must be sought.

Skin friction losses (δ_f) within the pump, caused by surface drag on fluid in the impeller passages and volute casing, are known to depend upon through-flow Reynolds Number under certain flow conditions. According to Nixon and Cairney[19], for this type of loss:

$$\delta_f \propto C_f W^2 \qquad \ldots (5.8)$$

where W is the relative fluid velocity, and C_f is a function of through-flow Reynolds Number and surface roughness. Figures 25a and b

illustrate the relationship between these parameters for the simplest case of a flat plate at zero incidence and for artificially sand-roughened pipes [23]. Up to a certain critical Reynolds Number (Re_{crit}) whose value depends on the surface roughness, C_f decreases as Re increases. The interdependence is approximately given by:

$$C_f \propto Re^{-0.25} \qquad \ldots (5.9)$$

This is the 'smooth' law regime.

Beyond the critical Reynolds Number, there is a transition regime, where values of C_f are difficult to quantify, but often rise with Re, followed by a region where C_f is independent of Re and is solely a function of $\frac{L}{\lambda_s}$, the relative roughness of the surface.

From Figure 25a, a good approximation of the upper limit of the smooth law behaviour is given by:

$$Re_{crit} \approx 100 \frac{L}{\lambda_s} \qquad \ldots (5.10)$$

In their extensive studies of skin friction losses in scale models of a centrifugal pump, Nixon and Cairney found that for the disturbed flow in an impeller, the flow conditions remain fully rough (C_f independent of Re) for considerably lower values of Re than for a flat plate. They considered that the value of Re_{crit} for pump flow was given by:

$$Re_{crit} \approx 25 \frac{L}{\lambda_s} \qquad \ldots (5.11)$$

(L = blade length). This is followed by a transition dip in the value of C_f, where flow conditions are not fully understood, but where anomalous behaviour, such as an increase in skin friction losses with Re, are to be

expected. Above the transition, C_f becomes independent of Re.

According to Hutton[29], the limiting surface roughness for rotating pump blades is represented by the following expressions:

(i) Lower limit between smooth and transitional flow:

$$\lambda_s = \frac{28\nu}{W} \qquad \ldots (5.12)$$

(ii) Upper limit between transitional and fully rough flow:

$$\lambda_s = \frac{224\nu}{W} \qquad \ldots (5.13)$$

The value of λ_s is given approximately by:

$$\lambda_s = 1.7 \, \lambda_{CLA} \qquad \ldots (5.14)$$

where λ_{CLA} is the surface roughness of the impeller, as measured on the Talysurf machine.

Therefore, an attempt was made to measure the surface roughness of the pump impeller, for substitution in the above equations. Techniques used for such measurements are described in Reference 18. Values of λ_{CLA} were obtained directly on the surface of an impeller blade and indirectly by replication (see Chapter 8.4 and Appendix V) of the inner impeller surface. The resulting CLA values ranged between 7 and 10+ μm.

In view of this wide scatter, the following factors were taken into account in order to choose a representative value for the pump CLA:

(a) 10μm is the upper limit of roughness for the Talysurf machine. The impeller surface may have been considerably rougher in places, but unfortunately no other instrument was available to provide the kind of detail of surface irregularities required for the present calculations (see Chapter 8.4).

(b) Visual inspection confirmed that there was a wide variation in surface roughness within the impeller passages. The roughest areas are likely to predominate in influencing the flow regime, since any turbulence which they generate will carry over into the smoother areas.

(c) Replication is not recommended on surfaces rougher than 4μm (160μ"). Above this value, the accuracy of the technique is worse than 10%.

Consequently, a figure of 10μm was chosen as a representative value for the CLA of the impeller surface. However, direct application of this value to Hutton's formulae is not necessarily valid, since no account has been taken of the surface profile and spacing of irregularities. Similar CLA values may be obtained from a uniformly rough surface and a surface consisting of fewer, but much larger, perturbations. The skin friction losses at two such surfaces may differ considerably, a concept which is discussed more fully in Chapter 8.4. Therefore, the figure of 10μm CLA is very approximate and can only give a general indication of the flow regime within the pump.

The values of Re, $\frac{28\nu}{W}$ and $\frac{224\nu}{W}$ presented in Table 5.1 have been calculated for each water temperature and pump speed at the flowrate corresponding to maximum pump efficiency. At this point of operation, the direction of flow within the impeller is assumed to match the impeller vane angle. The method for calculating W is set out in Appendix II and the variation of ν with water temperature is shown in Figure 4 . The length L for computing Re was taken as the blade length (9.3cm).

From Table 5.1 we may conclude that over the range of speeds and water temperatures tested, the pump is operating in, or close to, the regime of transition flow. At the lowest speeds in cold water, the "smooth" law of surface friction may apply, but any effects on the head characteristic would be masked by the inaccuracy of pressure readings (see page 31). At all speeds and temperatures, $\lambda_s < \frac{224\nu}{W}$ which indicates that

35.

Table 5.1: Calculations for Predicting the Flow Regime within the Pump in Water.

Pump Speed and Flowrate	Water Temp. [oC]	Re $[\frac{WL}{\nu}]$	$\frac{28\nu}{W}$ [m]	$\frac{224\nu}{W}$ [m]	λ_s^* [m]
n = 600 r.p.m. Q = 50ℓ.min^{-1}	25	0.83×10^5	3.1×10^{-5}	25×10^{-5}	1.7×10^{-5}
	56	1.53×10^5	1.7×10^{-5}	13.9×10^{-5}	
	81	2.14×10^5	1.2×10^{-5}	9.7×10^{-5}	
n = 1000 r.p.m. Q = 80ℓ.min^{-1}	25	1.33×10^5	2.0×10^{-5}	15.7×10^{-5}	
	56	2.40×10^5	1.1×10^{-5}	8.7×10^{-5}	
	81	3.43×10^5	0.76×10^{-5}	6.1×10^{-5}	
n = 1500 r.p.m. Q = 100ℓ.min^{-1}	25	1.59×10^5	1.6×10^{-5}	12.6×10^{-5}	
	56	2.87×10^5	0.87×10^{-5}	7.0×10^{-5}	
n = 2000 r.p.m. Q = 140ℓ.min^{-1}	25	2.33×10^5	1.1×10^{-5}	9.0×10^{-5}	
	56	4.19×10^5	0.62×10^{-5}	5.0×10^{-5}	
	81	5.99×10^5	0.43×10^{-5}	3.5×10^{-5}	
n = 2500 r.p.m. Q = 190ℓ.min^{-1}	25	3.03×10^5	0.82×10^{-5}	6.6×10^{-5}	
	56	5.45×10^5	0.46×10^{-5}	3.7×10^{-5}	
n = 3000 r.p.m. Q = 230ℓ.min^{-1}	25	3.81×10^5	0.68×10^{-5}	5.5×10^{-5}	
	56	6.86×10^5	0.38×10^{-5}	3.0×10^{-5}	
	81	9.80×10^5	0.26×10^{-5}	2.1×10^{-5}	
n = 3500 r.p.m. Q = 250ℓ.min^{-1}	25	4.16×10^5	0.63×10^{-5}	5.0×10^{-5}	
	56	7.49×10^5	0.35×10^{-5}	2.8×10^{-5}	
	81	10.7×10^5	0.24×10^{-5}	2.0×10^{-5}	

$^*\lambda_s = 1.7 \lambda_{CLA}$, where λ_{CLA} is the surface roughness of the impeller which was tested in water, as measured on the Talysurf machine (see page 34).

the region of fully rough flow (C_f independent of Re) is never
attained. However, if the chosen value of surface roughness is
slightly low, flow within the impeller passages could be fully rough
for operation at the highest speeds and water temperatures. This
might explain the absence of any interdependency between the head
characteristic and water temperature at 3,500 rpm.

For flow within the transition region, an increase in skin
friction losses with increasing Reynolds Number is to be expected.
Thus, as the temperature of the pumping fluid is increased, thereby
raising the value of throughflow Reynolds Number, frictional losses
within the pump also rise and the head characteristic falls slightly.
The phenomenon is most apparent between the tests at $25^{\circ}C$ and $56^{\circ}C$,
corresponding to a change in the kinematic viscosity of water from
0.9 to 0.5 cSt, as shown in Figure 4. A closer correlation is
found between the data collected at $56^{\circ}C$ and $81^{\circ}C$, since the kinematic
viscosity changes by only 0.15 cSt between these temperatures.

Figure 26 presents a graphical representation of the range of
throughflow Reynolds Number covered for each water temperature at
1500-3500 rpm. It is apparent that equivalent changes in Re should
be achieved, either by altering the fluid temperature or the pump
speed: for example, an increase in speed from 1500 rpm to 2500 rpm at
$25^{\circ}C$ is roughly equivalent to increasing the water temperature from
$25^{\circ}C$ to $56^{\circ}C$ at 1500 rpm.

We would therefore expect a corresponding drop in head
coefficient as the pump speed is increased, temperature remaining
constant. Although the head coefficient values at 3000 rpm and 3500
rpm in cold water fall slightly below the average curve (Figure 21)
the effect is not particularly marked and no such trends are apparent
at the higher water temperatures (Figures 22 and 23). This endorses
the point made by Osterwalder[26] that the manner in which the Reynolds
Number is changed, i.e. by altering the speed or the fluid viscosity,

will affect the friction losses. During recent research into the performance of pumps for automotive cooling systems, Hadji-Sheik[30] also found discrepancies between Re changes due to speed and fluid viscosity.

In the present work, results may be further complicated by the transition flow regime at the impeller passage walls. Flow conditions for this area of operation are not fully understood, as the relationship between skin friction losses and Re varies with different types of surface roughness[19]. However, it is apparent that a change in the viscosity of the pumping fluid has a greater effect upon the dimensionless head characteristic than a change in rotational speed. This is of particular importance for scaling results between water and mercury, since the latter fluid has an exceptionally low kinematic viscosity.

The preceding discussion is confined to the area of operation corresponding to maximum pump efficiency, where the relative fluid velocity may be calculated with reasonable accuracy. Conditions at other points of operation can only be treated qualitatively, due to the complications arising from flow separation, turbine action, etc.

Since throughflow Reynolds Number increases with flowrate, the convergence of the characteristic head curves for each water temperature at a given speed towards the point of maximum flowrate (Figures 16-19) may also be a Reynolds Number effect, with the flow regime becoming fully rough and skin friction losses independent of Re. The curves also converge at low flowrates, where skin friction losses in the impeller passages become negligible in comparison with hydraulic shock losses[31].

5.2.2 Power Characteristics

The dimensional absorbed power curves for the pump are presented in Figures 15-20. Their general shape is similar at all speeds and temperatures, with minimum power absorbed at zero flowrates, which is typical for a low specific speed radial pump. The curves exhibit a

38.

region of maximum slope in the middle range of flowrates, then flatten out at high flows.

There is a discrepancy between the power curves for the three water temperatures when the pump is running at 1000 rpm (Figure 15). However, no systematic trend is present and the difference can be accounted for by experimental error, since parasitic torque accounts for 60% of the gross measured torque at this speed (see Appendix IV).

At higher pump speeds, the absorbed power appears to differ slightly between high and low temperature runs, but when the results are plotted non-dimensionally for each water temperature, we find that all points fall onto a single curve with only slight scatter attributable to experimental error (Figures 27-29). Once again, the probable source of inaccuracies is uncertainty in the value of parasitic torque absorbed by the gearbox. The three smoothed curves of Figures 27-29 are almost identical, except that the power coefficient at zero flowrate is approximately 5% higher in water at $81^{\circ}C$ than at the lower temperatures.

The power absorbed by the pump is a function of the torque coefficient for disc friction C_{MD}, where:

$$C_{MD} = \frac{2M_D}{\rho \omega^2 R^5} \qquad \qquad \ldots (5.15)$$

The variation in C_{MD} for enclosed rotating discs has been thoroughly investigated by several workers[32,33].

Two flow regimes exist, one for a hydraulically smooth disc and the other for a rough disc.

In the smooth regime:

$$C_{MD} = 0.075 \, Re_{\omega}^{-0.2} \, [1 + 0.75 \, (\frac{s_s}{R} + \frac{s_t}{R})] \qquad \ldots (5.16)$$

In the rough regime:

$$C_{MD} = \frac{(1 + 0.75 \frac{s_t}{R})}{[3.8 \log_{10} (\frac{R}{k_s}) - 2.4(\frac{s_s}{R})^{0.25}]^2} \qquad \ldots (5.17)$$

According to Nixon and Cairney[19], the approximate boundary between the two regimes in a centrifugal pump occurs at $\lambda_{s_{crit}}$, where :

$$\lambda_{s_{crit}} \simeq \frac{150\nu}{\omega R} \qquad \ldots (5.18)$$

The maximum value of $\lambda_{s_{crit}}$ in the present work is 9.0×10^{-6} m, which corresponds to pump operation in cold water at 1000 rpm. This value is considerably lower than the estimated value of λ_s for the pump impeller (1.73×10^{-5} m), therefore the flow in relation to disc friction is in the fully rough regime at all speeds and water temperatures and C_{MD} is independent of Re_ω.

The following possibilities have been examined in an attempt to explain the high value of power coefficient at zero flowrate in hot water:

(a) The Effect of Leakage Flow: As the temperature of the pumping fluid is raised, leakage through the upper neckring, which is greatest at zero flowrate, also increases (see Figures 34 and 35). The relationship between seal leakage and disc friction for a radial flow pump has been investigated by Nixon and Cairney[19], who showed that the torque coefficient increases with leakage rate. In the present case, a 16.5% increase in leakage flow results when the water temperature is raised from 25°C to 81°C at 2000 rpm. Nixon and Cairney found that a similar increase in leakage rate caused a 1% rise in the value of C_{MD} for their pump. Even if we take into account the extra power which will be absorbed in pumping the leakage flow through the seals, this increase is

insufficient to explain the present discrepancy. Conversely, the work by Daily et al with enclosed rotating discs[34] shows a fall in C_{MD} with increasing radial inflow, which suggests that the higher leakage rate in hot water will decrease the pump absorbed power.

(b) Excessive End Load: The axial pressure distribution within the pump volute at low flowrates (see Figures 38 and 39) leads to a nett downward force on the impeller which, together with the weight of the impeller and shaft, could induce touchdown of the air bearing. However, calculations show that the maximum resultant end load is only 314N, or 50% of the specified end load for the bearing (see Appendix IIIA) and the possibility of an overload occurring has been discounted.

(c) Differential Thermal Expansion within the Test Rig: The shaft of the airbearing, which connects the bevel gearbox to the stub shaft carrying the pump impeller, is continuously cooled by high-pressure air supplied at a rate of 85 ℓ.min^{-1} (free air). It is also insulated from the pumping fluid by an external casing and the cylindrical steel support tube, with an air gap in between. Therefore its temperature is unlikely to change, regardless of the water temperature.

In contrast, the cylindrical steel tube which supports the pump volute casing is in direct contact with the water and once thermal equilibrium has been attained, the temperature of the support tube will match that of the water. The coefficient of linear expansion of mild steel is 11μm/m K. Since the tube is approximately 0.5m in length, the total thermal expansion between 25°C and 81°C will be about 0.3mm. Figure 1 shows that the upper neckring seal is positioned just above a radius on the impeller. If the tube supporting the pump volute expands whilst the length of the impeller shaft remains constant, the neckrings will move downwards in relation to the impeller, thereby decreasing the seal clearance.

As previously mentioned in Section 5.1, unequal pressures within the pump volute at low flowrates were found to cause deflection of the pump shaft at high speeds, which induced rubbing of the neckrings. With a reduced seal clearance due to differential expansion rates, this will occur more readily and seems the most likely explanation for the high power coefficient measured at zero flowrate in hot water. The rub was not severe enough to activate the torque limiter at speeds less than 3000 rpm.

The above theory is borne out by the presence of wear marks on the impeller hub beneath the upper neckrings, which were found when the pump was dismantled after the initial stages of the research programme.

5.2.3 Efficiency Characteristics

The efficiency curves of Figures 15-20 show that the maximum efficiency attained at all speeds is about 50%. This figure was calculated using nett power absorbed by the pump and excludes all bearing friction and motor efficiencies. It would not be possible to attain a comparable overall efficiency under normal plant running conditions. The top of the efficiency curves are fairly flat, so that high efficiency may be attained over a wide range of flowrates. However, it is interesting to note that at its normal duty point in the plant at I.C.I. (1450 rpm, $55\ell.min^{-1}$ mercury flowrate) the pump is operating at an efficiency considerably below the maximum (see Figure 16).

The detrimental effect of increased water temperature on the pump delivered head between 1500-3000 rpm (section 5.2.1) is reflected by a decrease in efficiency at $56^{\circ}C$ and $81^{\circ}C$. Flow conditions become fully rough within the impeller passages at 3500 rpm, so the efficiency is no longer a function of temperature. Note that the outlying points at high flowrates in Figures 19 and 20 are caused by inaccurate flowrate measurements (see Section 5.2.1).

When efficiency is plotted against flow coefficient for each water temperature, the points fall onto a single common curve (discounting 1000 rpm): see Figures 30-32. The efficiency at 3000 and 3500 rpm in cold water falls just below the main curve, corresponding to the lower head coefficient at these speeds in cold water (Figure 21).

The effect of water temperature on pump efficiency is illustrated more clearly in Figure 33.

5.3 Neckring Leakage at Standard Seal Clearance

Figures 34 and 35 illustrate the relationship between upper neckring leakage rate and pump delivery flowrate for all speeds and water temperatures that were investigated. The radial clearance of the upper and lower neckring seals was 0.165mm, as specified for a standard pump (Appendix I).

At a given pump speed and flowrate, the leakage increases with water temperature, as a consequence of the reduction in viscosity of water at elevated temperatures. The possibility of an increase in leakage rate due to thermal expansion at elevated temperatures has been discounted, since the radial neckring clearance increases by less than 0.1% between $25^{\circ}C$ and $81^{\circ}C$. Values of the percentage increase in maximum leakage rate (i.e. at zero pump flowrate) when the water temperature is raised from $25^{\circ}C$ to $56^{\circ}C$ and $81^{\circ}C$ are presented in Table 5.2. The data in this table shows that the effect of reduced viscosity on leakage rate becomes less marked at high rotational Reynolds Numbers.

The graphs of leakage as a function of pump flowrate generally take the form of a smooth curve with a negative gradient. Occasionally however, the relationship appears to be linear. It is not clear why this should be so, especially since no systematic trend is exhibited, but eccentricity of the seal clearances under certain operating

Table 5.2: Increase in Upper Neckring Leakage Rate at
            Elevated Water Temperatures

          Tabulated values give the increase in maximum leakage rate
(i.e. at zero pump flowrate) at the stated water temperature, expressed
as a percentage of the leakage rate in cold water (25°C) at the same
point of operation.

| Pump Speed | Water Temperature ($^{\circ}$C) | |
(r.p.m.)	56	81
600	14%	45%
1000	16%	28%
1500		18%
2000	7%	15%
2500		5%
3000	5%	7%

Water Temperature ($^{\circ}$C)	Kinematic Viscosity of Water ($m^2.sec^{-1}$)
25	0.905×10^{-6}
56	0.510×10^{-6}
81	0.364×10^{-6}

conditions could account for the small differences involved.

Typical measured seal leakage values for the pump operating over a range of speeds and flowrates have been compared with predicted values according to a correlation developed by Weber[35]. The correlation is based on the following equation, which gives the rate of flow through an annular slot formed by a smooth-walled outer cylinder and a rotating inner cylinder:

$$Q_{s1} = \theta A_{s1} \sqrt{\frac{2\Delta p_{s1}}{\rho}} \qquad * \qquad \ldots \quad (5.19)$$

The total resistance to flow can be broken down into two components: that due to the slot inlet and outlet, and friction between the fluid and slot walls. Therefore, the flow coefficient θ is given by:

$$\theta = \frac{1}{\sqrt{(\frac{\lambda L}{2h} + \zeta_{io})}} \qquad \ldots \quad (5.20)$$

Here ζ_{io} comprises the flow resistances at the slot inlet and outlet.

The test programme carried out by Weber showed the following interdependencies:

1. For flow resistance in the slot:

$$\lambda = f(Re_{\bar{y}}, Re_u, L, h).$$

2. For flow resistance at the slot inlet and outlet:

$$\zeta_{io} = f(Re_{\bar{y}}, Re_u, h, \text{ shape of the slot inlet and outlet,}$$
$$\text{prerotation of the liquid before the slot inlet})$$

---

*Some symbols in the following paragraphs have been altered from the original to conform with the notation generally accepted in the U.K.

In the above expressions, Re_u is the Reynolds Number formed with the peripheral velocity u, and $Re_{\bar{y}}$ is formed with the mean axial velocity $\bar{y}$,

i.e $\qquad Re_u = \dfrac{2hu}{\nu}$ $\qquad\qquad$ ... (5.21)

$\qquad\qquad u = \dfrac{d\omega}{2}$ $\qquad\qquad$ ... (5.22)

$\qquad\qquad Re_{\bar{y}} = \dfrac{2h\bar{y}}{\nu}$ $\qquad\qquad$ ... (5.23)

$\qquad\qquad \bar{y} = \dfrac{Q_{s1}}{A_{s1}}$ $\qquad\qquad$ ... (5.24)

Since Q_{s1} is unknown, the estimated value is normally inserted in equation (5.24) to find $\bar{y}$ and hence $Re_{\bar{y}}$. An iterative process is then used to calculate the leakage flow. However, in the present case, the measured value of Q_{s1} was substituted in equation (5.24).

Figures 36a and 36b, which have been redrawn from Reference 35, illustrate the variation of λ and ζ_{io} with Re_u and $Re_{\bar{y}}$.

The predicted leakage rate was calculated for the following operational speeds and water temperatures:

a) At 1500 r.p.m. in cold water (close to the normal duty speed of the pump).

b) At 600 r.p.m. in cold water (minimum values of Re_u).

c) At 3500 r.p.m. in water at $56^{\circ}C$ (maximum values of Re_u for which a complete set of experimental data is available).

A numerical example of the relevant calculations is contained in Appendix VI.

The predicted values have been plotted on Figures 34 and 35 for comparison with experimental results. Generally, the predicted leakage rates are too low. At 1500 r.p.m., the maximum error is 20%, whereas at 3500 r.p.m. the predicted values are about 30% lower than those measured. The agreement between predicted and experimental curves is generally better at high pump delivery flowrates, when differential pressures across the neckring, and hence the rate of leakage, are lower. This would indicate that the relationship between slot flowrate and axial flow Reynolds Number, as determined by Weber, requires some modification for the pump presently under investigation.

At 600 r.p.m., the percentage error varies between 50% too high and 16% too low, but this is mainly attributable to limitations of the instrumentation on the rig for measuring small changes in leakage and/or pressure, combined with the relatively low precision of Figures 36a and b.

Application of Weber's graphs to the present work is not totally justified for the following reasons:

1. Weber used a slot width (h) of 0.203mm to obtain the inter-dependencies of Figures 36a and b. With a reduced radial seal clearance of 0.165mm, the resistance to flow at the slot inlet and exit will increase, leading to higher values of ζ_{io}.

2. Figure 36b is based on a full-edged slot entrance. Weber found that a bevelled entrance, such as that of the pump upper neckring, decreased the resistance to flow at the slot inlet. Thus the value of ζ_{io} would be smaller in the present case.

3. Prerotation of the fluid, induced by contact with the back of the pump impeller, will also reduce the resistance to flow at the slot inlet and hence the value of ζ_{io}. Such prerotation was minimised on Weber's rig by fixed blades in front of the slot entrance.

From the above considerations we may deduce that the values of ζ_{io} used in the present leakage calculations are too high, which partially accounts for the discrepancy between predicted and experimental values.

A further factor is the non-concentricity of the impeller neck within the seal clearance. Wear marks on the neckring and impeller have shown that the shaft often runs slightly eccentrically (see Section 5.2.2) and this would have a significant effect on the rate of leakage. Shaft run-out is known to increase with rotational speed (Section 5.1) which explains the large error in calculated leakage rate at 3500 r.p.m.

Finally, the range of Re_u and $Re_{\bar{y}}$ values covered by pump operation between 600 and 3500 r.p.m. at the various water temperatures is greater than that covered by Weber's graphs. Therefore, the curves in Figures 36a and b had to be extrapolated for many of the calculations, which inevitably involves an unknown error.

Despite these shortcomings, Weber's method gives a reasonable, if somewhat low, estimate of the rate of leakage through the upper seal on the pump. It would be interesting to apply his formulae to other centrifugal pumps whose seal dimensions and geometry conform more closely with the experimental arrangements used in his own work.

The relationship between the static pressure difference across the upper neckring and the leakage flowrate for the pump operating at various speeds in water is presented in Figure 37. Data from each test speed falls on a separate curve, confirming Weber's results[35], which showed an interdependency between slot flowrate and rotational Reynolds Number.

The general trend of this family of curves is not followed at

the lowest pump speed of 600 r.p.m. where the gradient of the curve increases rather than decreases as the differential pressure across the neckring is raised. In physical terms this means that a small rise in differential pressure causes a disproportionate increase in leakage rate. Such behaviour may be predicted from Figure 36a. At very low values of rotational and through flow Reynolds Number (in the present case, Re_u = 525 and $Re_{\bar{y}}$ = 270-470), the graph of friction coefficient λ against $Re_{\bar{y}}$ is steepest. Consequently, a small increase in $Re_{\bar{y}}$ leads to a considerable reduction in the friction losses between the leaking fluid and slot walls, and the leakage rate increases rapidly with Δp.

The separate curves of Figure 37 do not appear to extrapolate through the origin: they would pass through the abscissa at some positive differential pressure. This illustrates the effect of wall friction resistance to flow through the seal clearance and of slot inlet and outlet resistances as outlined by Weber[35] and represented mathematically in Equation 5.20. The implication here is that at each pump speed there is a certain pressure difference across the upper neckring at which the seal would be 100% effective. Unfortunately, such a low differential pressure is never attained during normal pump operation and the seal always leaks.

The upper and lower neckring pressures during operation in water at 20°C and 81°C have been plotted as a function of pump delivery flow-rate in Figures 38 and 39. Results at 56°C, which show a similar trend to those illustrated, have been omitted for the sake of clarity.

These graphs illustrate the change in axial pressure distribution within the volute as the flowrate is altered. At high flowrates, the pressure at the lower neckring periphery, i.e. below the impeller, is higher. This pressure difference will be balanced to a certain extent by the weight of the impeller and shaft so that any resultant end load

on the thrust bearings is reduced. As the delivery valves are closed
both the upper and lower neckring pressures increase, but the change
in upper neckring pressure is greater, so that the pressure differential
decreases. At a certain flowrate, roughly between $50-90\ell.min^{-1}$, the
pressures above and below the impeller are equal. At near zero flow-
rates, the pressure at the upper neckring is higher, resulting in a
nett downward end load acting in the same direction as the weight of
the impeller and shaft. Calculations have shown that the maximum
resultant load is well within the specified limits of the gas bearing
(see Section 5.2.2).

The reasons for this change in pressure distribution within the
pump casing are at present unclear. The fact that the upper neckring
pressure is less than the lower neckring pressure at high pump flowrates
(i.e. minimum leakage and hence minimum flow between the impeller and
casing) may be explained by the fact that the two tappings are at slightly
different radii: 36.6mm for the upper neckring and 41.3mm for the lower.
If the fluid between the impeller and casing rotates as a forced vortex,
the radial pressure drop will be proportional to the square of the radius.
At higher pump speeds, as the pressure at the impeller tip increases,
the effect of this difference in the position of the two tappings becomes
more marked.

The fact that the pressure rises more steeply at the upper
neckring than at the lower neckring as the volute pressure increases
(i.e. pump flowrate is reduced) may be connected with the concomitant
rise in seal leakage rate.

In an extensive study of the flow around enclosed rotating discs,
Daily et al[34] showed that the pressure gradient across the back of
such a disc is a function of the throughflow between the disc and its
casing. This effect is modified by the axial clearance between the
disc and case, being most marked at small clearances. Therefore, the

present phenomenon could possibly be explained by one of the following factors, or a combination of the two.

(i) Leakage through the lower seal is likely to be about 37% higher than through the upper seal, because of its larger diameter (Appendix I).

(ii) The axial clearances above and below the impeller are not specified on the pump drawings and are extremely difficult to measure in situ. It may be that the impeller was fitted asymetrically within its casing, so that the axial clearance on one side was very small.

Unfortunately time limitations did not permit further investigation into the causes of this phenomenon.

Volumetric efficiency curves for the pump are presented in Figures 40-43. The total seal leakage rate has been calculated by assuming that the ratio of the leakage rates through upper and lower seals will be equal to the ratio of the cross-sectional areas of their annular clearances, or 1:1.375 (see Appendix I). This assumption is not entirely valid for the following reasons:

(a) Pressures at the entrance to the two neckrings are rarely equal (see Figures 38 and 39).

(b) The exit pressure head at the lower neckring, which is submerged in the pump tank, is approximately 0.3m of water higher than that of the upper neckring, which is at atmospheric pressure.

Consequently, the differential pressures across the two seal clearances, which directly affect the leakage flowrate as indicated by equation (5.19) are not equal. However, calculations indicate that the resultant error should be less than 5%, particularly at pump speeds of 1500 r.p.m. and above.

51.

The volumetric efficiency (η_{vol}) is then calculated from the following equation:

$$\eta_{vol} = \frac{Q}{Q + Q_{leak}} \times 100\% \qquad \ldots \text{(5.25)}$$

Figures 40-43 show that the fall in volumetric efficiency due to an increase in temperature of the pumping fluid is less marked at higher rotational speeds. In fact, at 3500 r.p.m., the difference between cold and hot water results is so small that a single curve has been drawn through all points. At each speed an efficiency of at least 85% is attained at maximum flowrate, but the curves are much steeper for low speeds, so that a high efficiency occurs earlier on the characteristic.

It is interesting to note that at 1500 r.p.m. and a flowrate of $55\ell.\text{min}^{-1}$, which roughly corresponds to the duty point of the pump, the volumetric efficiency is less than 70% in warm water. Thus a considerable gain in overall efficiency with corresponding reductions in power consumption, would be achieved if effective shaft seals were fitted.

Since the volumetric and overall efficiency characteristics of the pump are known, we may calculate the hydraulic efficiency from the formula:

$$\eta_{overall} = \eta_{vol} \cdot \eta_{mech} \cdot \eta_{hyd} \qquad \ldots \text{(5.26)}$$

It has been assumed that η_{mech} is approximately 100% on the water rig, as an allowance has already been made for losses in the gearbox, whilst bearing and seal friction losses are negligible.

The hydraulic efficiency curves for two representative speeds (1500 r.p.m. and 3000 r.p.m., cold water) are presented in Figures 44

and 45. The curves are flat topped with a broad range of flowrates over which a high efficiency is attained. In both cases, the maximum efficiency is better than 60%, which is an acceptable value for a low specific speed pump operating at relatively low flowrates[31].

5.4 Pump Performance with Increased Seal Clearance

As previously explained in Section 5.1, the pump performance was also investigated with the impeller hub machined down to increase the upper and lower seal clearance, i.e. to simulate running in a worn condition. The radial seal clearances chosen were (a) 0.318mm (0.025"), which represents an approximate increase of 100% in the clearance, and (b) 0.636mm (0.050"), corresponding to the maximum amount of wear that can be tolerated on a pump operating under normal plant conditions at I.C.I. (see Chapter 2.5).

The effect of this increased seal clearance on the pump performance is shown in Figures 46-53, where the characteristics of a "new" pump (i.e. standard seal clearance) have been marked with a solid line and the broken lines represent the characteristics at larger clearances.

5.4.1 Head Characteristics

At a given speed, water temperature and delivered flowrate, an increase in seal clearance causes a drop in pump outlet pressure. This pressure drop is not constant along the pump characteristic for a particular speed and the maximum difference generally occurs in the middle flowrate range. Values of the decrease in pump delivered head, expressed as a percentage of the maximum head produced by the pump in the new condition (i.e. the head at zero flowrate), are presented in Table 5.3. For each speed, water temperature and seal clearance, the head drop at zero and maximum flowrates, plus the maximum head drop (which occurs in between) have been tabulated.

Table 5.3: Decrease in Pump Delivered Head at Increased Seal Clearance

Tabulated values give the head drop under the stated operating conditions, expressed as a percentage of the maximum head delivered by the standard pump (0.165mm radial seal clearance) at the corresponding speed and water temperature.

Point of Operation	Pump Speed (r.p.m.)					Conditions
	600	1000	1500	2000	3000	
Q = 0	0*	1%	2%	3%	2%	Radial seal clearance = 0.318mm
Max. head drop	0*	3%	13%	8%	5%	Water temperature = 25°C
Q = max.	0*	0	4%	3%	4%	
Q = 0	2%		3%		3.5%	Radial seal clearance = 0.318mm
Max. head drop	9%		5%		3.5%	Water temperature = 81°C
Q = max.	8%		4%		2.5%	
Q = 0	8%	10%	8%	7%	5%	Radial seal clearance = 0.636mm
Max. head drop	16%	16%	16%	15%	12%	Water temperature = 25°C
Q = max.	16%	14%	14%	14%	11%	
Q = 0	25%		7%		4%	Radial seal clearance = 0.636mm
Max. head drop	27%		12%		8%	Water temperature = 81°C
Q = max.	23%		11%		8%	

*Note: The pressure drop under these operating conditions was too small to be detected by the gauge (graduated in units of 0.5 psi).

At a particular speed and water temperature, the family of head/flow curves for the three seal clearances converge at zero flowrate. This can be explained by the flat head characteristics of the pump at low flows, which masks the deterimental effect of leakage on measured fluid flowrate at the pump outlet. A similar convergence of curves for the three clearances occurs at maximum flowrates, where the lower leakage rate (see Figures 65 and 66) represents a much smaller percentage of the total flow through the pump.

Several factors will influence the pump performance with worn seals. One of the main parameters is the ratio of leakage flowrate to delivered flowrate (Q_{leak}:Q) and the consequent shift of the head/ flow characteristic towards the ordinate axis. But, as we have seen in Section 5.3, the leakage flowrate is itself a function of rotational and throughflow Reynolds Numbers, as well as seal clearance and eccentricity. In addition, the effect of fluid jetting from the lower seal, which will cause disturbed flow conditions at the impeller inlet (see Figure 1) must be considered. The random values of the decrease in delivered head shown in Table 5.3, which bear no direct relationship to speed or water temperature, reflect the complexity of these factors governing the behaviour of a worn pump.

The head/flow data for increased seal clearance is presented non-dimensionally in Figure 54 (cold water) and Figure 55 (hot water). Cold water results at 0.318mm clearance scale well, falling onto a common curve, but at 0.636mm clearance, the increased leakage causes a wide scatter of points. Leakage is also increased by the higher water temperature, so that even at the smaller clearance in hot water, the pump performance cannot be predicted with accuracy by the conventional method of dimensionless parameters (Figure 55).

In an attempt to encompass the effect of seal leakage within the performance scaling technique, the dimensionless head values for two representative speeds at each seal clearance have been plotted

against the total flow coefficient (ϕ_{tot} - see Equation (5.7)) in Figures 56 (cold water) and 57 (hot water). In both cases there is a slight speed effect, which becomes more marked at the higher leakage rates in hot water. However, there is reasonable agreement between points obtained for different seal clearances at a single speed, so it appears that this simple mathematical procedure may be used to predict the effect of seal leakage on pump delivered head at a fixed speed and water temperature with an accuracy of ±3%. However, the conventional performance scaling techniques which involve changes of speed and/or kinematic viscosity cannot be applied with such accuracy at high leakage rates, even if allowance is made for the effect of that leakage on the nett pump flowrate through the concept of a total flow coefficient.

5.4.2 Power Characteristics

Figures 48-50 and 52-53 show that for a given speed and water temperature, the absorbed power is generally higher at zero flowrate and lower at maximum flowrate if the seal clearance is increased; i.e. the gradient of the power curve is reduced. This effect becomes more marked at the wider clearance. The change in absorbed power at the extremes of the characteristic have been tabulated for the reader's convenience below.

Table 5.4: Change in Pump Absorbed Power at
            Increased Seal Clearance in Cold
            Water.

Tabulated values are expressed as a percentage of the nett power absorbed by the standard pump (0.165mm seal clearance) at the same point of operation.

Nett Pump Flowrate	Pump Speed (r.p.m)			Radial Seal Clearance (mm)
	1500	2000	3000	
Q = 0	+ 4%	+ 3%	+ 8%	0.318
Q = max.	- 3%	- 2%	- 3%	0.318
Q = 0	+14%	+23%	+22%	0.636
Q = max.	- 5%	- 4%	- 6%	0.636

Water Temperature = 25°C

At very low flowrates, the extra power required to pump fluid through an increased seal clearance constitutes a substantial proportion of the total pump power requirement. However, as the flowrate rises, the effect of leakage on disc friction becomes the over-riding factor. Previous research has shown [34] that the torque absorbed by an enclosed rotating disc is reduced when fluid flows inward through the surrounding casing. In the present experiments, fluid leaking between the pump impeller and its housing has similar consequences and the overall power consumption at high flowrates falls as the seal clearance is increased.

There is no apparent increase in absorbed power for the 0.318mm clearance results in hot water as compared with the standard pump at zero flowrate (Figures 52 and 53). Here the wider seal clearance has eliminated the rub between the impeller hub and neckrings (see Section 5.2.2), thereby offsetting the extra power required for leakage flow. However, a further rise in leakage at 0.636mm clearance means that the power input at low nett flowrates exceeds that of the standard pump, confirming the measurements taken in cold water.

The absorbed power measurements do not scale well, as shown by the non-dimensional plots of Figures 58-61. If the results are plotted on a total flow basis (ϕ_{tot} - see equation 5.7), in order to eliminate the effect of leakage flow that is pumped through the impeller but is not measured with the nett pump flowrate, the scatter is increased: see Figure 62. Many factors are concerned here. The power required to pump fluid round the pump volute and out through the delivery pipe will differ from that required to force leaking fluid between the impeller and casing, then out through the seal clearance. The latter will depend on the resistance to flow in the slot (see Section 5.3), which in turn is a function of rotational speed and clearance (Figures 36a and b). An additional consideration is the effect of leakage on disc friction mentioned above. A detailed analysis is beyond the scope of the present project, but these results indicate that the effect of leakage on pump

absorbed power is one area of pump operation where further research would be fruitful.

5.4.3 Efficiency Characteristics

The overall maximum pump efficiency decreases by about 5% at 0.318mm seal clearance and 10-15% at 0.636mm clearance, as shown in Figures 48-50 and 52-53. The flowrate for maximum efficiency, which does not change at 0.318mm clearance, is some 5% lower at the widest clearance.

In view of the scatter shown on the dimensionless head and power characteristics for 0.318mm clearance (Figures 54-55, 58 and 60), it is surprising that the corresponding efficiency results scale well, as shown in Figure 63 and 64. However, at 0.636mm clearance the correlation is poor, with lower efficiencies being attained as the pump speed is increased, at both water temperatures. This trend is related to the speed effect exhibited by the dimensionless power results in Figures 59 and 61.

5.5 Neckring Leakage with Increased Seal Clearance

The relationship between upper neckring leakage rate and nett pump flowrate in hot and cold water is shown in Figure 65 for 0.318mm seal clearance and Figure 66 for 0.636mm clearance. In the latter case, water temperature has little effect on leakage rate, and an apparent 3-4% reduction in leakage for hot water at 3,000 r.p.m. indicates the probable size of experimental error in leakage measurements. The extent of leakage losses in a worn pump and the diminished significance of changes in fluid viscosity at large seal clearances are illustrated more clearly in Tables 5.5 and 5.6.

Table 5.5: Effect of Seal Clearance on Upper
Neckring Leakage Rate in Cold Water

Tabulated values give the rise in maximum leakage from
the upper neckring, expressed as a percentage of the
maximum leakage in a standard pump operating at the same
speed, due to increased seal clearance.

Pump Speed	Seal Clearance (mm)	
(r.p.m.)	0.318	0.636
600	109%	227%
1000	75%	223%
1500	74%	213%
2000	62%	189%
3000	58%	167%

Table 5.6: Effect of Water Temperature on Upper
Neckring Leakage Rate at Increased
Seal Clearance

Tabulated values give the percentage increase in maximum
leakage from the upper neckring in water at 81°C, as
compared with the leakage in cold water (25oC) at the
same speed and seal clearance.

Pump Speed	Seal Clearance (mm)	
(r.p.m.)	0.318	0.636
600	24%	18%
1500	7%	0%
3000	0%	-3%

Water Temperature (°C)	Kinematic Viscosity of Water $(m^2.sec^{-1})$
25	0.905×10^{-6}
81	0.364×10^{-6}

Although Figures 65 and 66 are of interest for comparing leakage losses with pump delivered flowrate, these two variables are not directly related. The primary factor governing seal leakage is the pressure at the neckring entrance, which changes according to the pump operating point and seal clearance, thereby governing the shape of the leakage versus pump flowrate graphs.

The variation of upper and lower neckring pressure with pump flowrate is shown in Figures 67 (0.318mm clearance) and 68 (0.636mm clearance). The "cross-over" effect exhibited at standard seal clearance (see Figures 38 and 39) is shifted to the left as the clearance is increased, so that it is never attained at 0.636mm clearance, where pressure at the lower neckring is always greater. This shift is caused by a larger pressure drop at the upper neckring than at the lower neckring as the seal clearance is increased, as shown by the data in Table 5.7.

Table 5.7: Decrease in Seal Entry Pressure at
Zero Pump Flowrate (1500-3000 r.p.m.)

Values are expressed as a percentage of the seal entry pressure at standard clearance and zero flow.

Neckring	Seal Clearance (mm)	
	0.318	0.636
Upper	8 - 10%	37 - 40%
Lower	4 - 5%	24 - 25%

This effect may be attributed in part to the higher pressure at the lower neckring exit, as discussed in Section 5.3.

Upper neckring leakage rate has been plotted as a function of differential pressure across the seal in Figure 69 (0.318mm clearance) and Figure 70 (0.636mm clearance). The slight deviation of points corresponding to a given speed and water temperature from the general trend exhibited by the results taken as a whole illustrates the inter-dependency of leakage flowrate with rotational and throughflow Reynolds Numbers.

To examine the variation of leakage with neckring clearance, results from the whole speed range 600-3500 r.p.m. have been put into envelopes: see Figure 71. The leakage rate is not directly proportional to $\sqrt{\text{(pressure drop)}}$, but rises more rapidly, particularly at low differential pressures.

By cross-plotting the curves of Figure 71, the effect of radial seal clearance (which is approximately proportional to clearance area for a narrow annulus) on seal leakage at a given pressure drop is shown more clearly: see Figure 72. For the range shown on the figure, the relationship between leakage and radial clearance is parabolic. All the curves, if extrapolated, would cut the ordinate at a positive leakage value, implying the existence of a discontinuity at small radial clearances. The transition may also be predicted from Figure 36a, which shows that for $Re_{\bar{y}} < 2\text{x}10^3$ and $Re_u \leqslant 3000$, the slot friction coefficient rises sharply if leakage flow and/or radial clearance (and hence $Re_{\bar{y}}$) is further reduced. For the range of Re_u under investigation, this laminar flow regime prevails entirely at radial clearances below 0.1mm, where the curves in Figure 72 will be much steeper. At low rotational Reynolds Numbers, the transition occurs at a wider clearance and its effects have been demonstrated in the standard pump at 600 r.p.m. (see Section 5.3).

The lower neckring leakage rate has been estimated, as in Section 5.3, from leakage measurements at the upper neckring with a wider clearance, by allowing for the larger radius of the bottom seal.

This method becomes less accurate as the pressure difference between upper and lower neckrings increases (compare Figures 38 and 39 for the standard pump with Figures 67 and 68). The error in total seal leakage data for 0.318mm clearance is less than $\pm 5\%$ at low flowrate, but rises to $^{-5}_{+10}\%$ at maximum flows, where pressure is much higher at the bottom seal than at the top. With an even greater pressure difference at 0.636mm clearance, the probable error in the middle flowrate range is $^{-5}_{+15}\%$. In both cases, the calculated leakage rate is probably low.

The volumetric efficiency of the pump at various duties has been determined from the leakage data and is presented in Figures 73-79. The maximum volumetric efficiency is 80-83% at 0.318mm clearance and 71-75% at 0.636mm clearance, in contrast to values of 86-90%, in the standard pump (see Figures 40-43).

The hydraulic efficiency of the pump operating in cold water at 1500 r.p.m. and 3000 r.p.m. with increased neckring clearance has been computed from Equation (5.26) and the resultant curves are compared with the standard pump characteristics in Figures 80 and 81. These figures indicate that the hydraulic efficiency would actually be increased in a worn pump, particularly at low flowrates.

Such a phenomenon could only occur if there was substantial recovery of the dynamic pressure of leakage flow jetting from the lower neckring into the pump inlet. Initially, this explanation was felt to be implausible, but subsequent trials on the standard pump in mercury, where leakage is higher than in water due to a lower kinematic viscosity, lend support to the hypothesis (see Chapter 7.3.1).

The dynamic pressure head of leakage flow has been calculated for a representative pump speed and flowrate at each seal clearance: see Table 5.8. The proposed path for the leakage flow has been marked in Figure 1.

Table 5.8: Details of Lower Neckring Leakage
at Different Seal Clearances

Pump Speed: 1500 r.p.m.; Nett Flowrate: $25\ell.min^{-1}$
Test Fluid: cold water.

| Radial Seal Clearance (mm) | Gross Pump Flowrate $(Q + Q_{leak})$ $\ell.min^{-1}$ | Computed Lower Neckring Leakage | | Dynamic Pressure of Leakage (m.of water) |
		Absolute $(\ell.min^{-1})$	% of Gross Pump Flowrate	
0.165	47.6	13.1	27.5%	1.8
0.318	63.0	22.0	34.9%	1.4
0.636	90.3	37.8	41.9%	1.0

Although the velocity, and hence dynamic pressure, of the leakage is shown to fall at wider seal clearances, fluid jetting from the lower neckrings forms a higher percentage of the gross flow through the pump inlet. The theory can therefore neither be proved nor disproved from the available data.

It is also possible that the computed values of η_{hyd} in Figures 80 and 81 are too high, due to errors in the original calculation of volumetric efficiency. This could arise if the rate of leakage through the lower neckring were over-estimated, leading to low values of η_{vol}, which will be particularly misleading at low flowrates, where the measured upper neckring leakage is greatest. However, the axial pressure distribution within the pump volute is more likely to cause an under-estimation of lower neckring leakage, as shown by the quoted accuracy of this data.

A true picture of the changes in hydraulic efficiency of a pump with worn seals can only be obtained through experimental determination of the leakage rate through both neckrings. The time and expense

involved in fitting such sophisticated equipment as would be required
to measure lower neckring leakage, without causing other side-effects
on the pump performance, could not be justified for the present project.

5.6. Summary of Results

An outline of the main features arising from the pump performance
trials in water is presented below for the convenience of the reader.

1. Analysis of the head characteristics of the standard pump
shows a slight Reynolds Number effect for changes of fluid viscosity,
but not for speed changes, within the same range of Re_{ω}. Investigation
of this aspect of performance scaling is complicated by the prevailing
transition flow regime near the impeller passage walls, which causes
an increase in skin friction losses as the viscosity is reduced. In
contrast, the pump absorbed power characteristics are found to scale
well for both speed and viscosity changes, as the flow regime on the
shroud walls is fully rough/turbulent and disc friction losses are
independent of Re_{ω} .

2. When the neckring seal clearance is increased, the maximum
head drop occurs in the middle flowrate range (i.e. near the duty point).
The head characteristics cannot be scaled accurately by conventional
techniques, but by introducing a total flow coefficient, which encompasses
the leakage flow, the head characteristic at different seal clearances
can be predicted for a given speed.

The pump absorbed power rises at low flowrates for a wider
seal clearance, but is found to fall below that of the standard pump
at higher flows. The power characteristics cannot be scaled, even if
a total flow coefficient is used.

3. The hydraulic efficiency of the pump is shown to increase
at wider seal clearances, due to the recovery of the dynamic pressure
from leaking fluid which jets from the lower neckring clearance gap
and re-enters the impeller.

CHAPTER 6

MERCURY TEST RIG

6.1 Mechanical Layout and Hydraulic Circuit

A pump test rig (the Off-Load Rig) was available for the
present project in the I.C.I. (Mond) Research and Development Department
at Winnington, Cheshire. The rig had previously been used for research
into aspects of cell and pump performance. Although it was modified
to suit the special requirements of the project in hand, limited funds
and a shortage of workshop time meant that the test facilities were
less sophisticated than on the water rig at Southampton.

A diagram of the salient features of this rig is presented
in Figure 82. The pump impeller is keyed into the extended shaft of
a 2.6kW (3.5 HP) 40 volt 3 Phase induction motor. The whole pump body,
which is a duplicate of the one used on the water rig at Southampton,
is immersed in a small sump at the bottom and towards one end of the
mercury collecting tank. This part of the test rig is identical to the
installation in some production plant. A level glass is fitted for
measuring the depth of mercury in the sump.

The pump delivers mercury into a simple hydraulic loop consisting
of two branches, each containing a venturi flowmeter and control valve.
This system with parallel pipework was installed because the original
single venturi severely limited the maximum attainable flowrate. The
two branches rejoin before the mercury is returned via a simple open-
ended pipe into the collecting tank at the opposite end to the pump
sump. This return flow jets with considerable momentum out of the pipe,
but much of the turbulence is lost by the time the fluid has run down
the tank floor into the sump.

Because of the toxic nature of mercury vapour, all free surfaces of the fluid are covered with water and the rig is equipped with an extraction hood and safety screens.

A steam line is available to heat the mercury for high temperature runs.

The technique for measuring neckring leakage caused many problems and was never fully satisfactory in achieving adequate precision. The leakage flow enters the annular space between the pump shaft and the surrounding support tube (see Figure 1) whence it jets out through two diametrically opposed holes in the support tube, into the pump tank below. It is important to avoid applying back pressure to these holes, otherwise the mercury would rise up the shaft and damage the induction motor. However, the openings are on a level with the floor of the tank, which means it is impossible to catch the leaking fluid directly.

The specially-designed arrangement for collecting the leakage flow is illustrated in Figure 83. Two U-shaped tubes, with a lift of 75mm, are clamped against the holes in the support tube and rubber tubing, connected to the ends of the U-tubes, is used to direct the leaking fluid into a shallow tray situated on the floor of the tank for a given time period. The mercury is then decanted into a graduated cylinder for volumetric measurement.

The two hydrodynamic seal designs were tested during the latter stages of the project in conjunction with the pump in mercury. As on the water rig, it was necessary to fabricate an extension to the pump shaft which would carry the pump and seal impellers and to extend the pipework connected to the pump outlet for these trials. Extra clearance between the sump floor and the bottom of the sump was required to accommodate the hydrodynamic seal, so a new framework was built in order to lift the whole motor/pump assembly by about 6cm. The final

set-up was identical to that used for performance trials in water, as shown in Figure 11.

Since a pressurized, piped supply of mercury was not available, individual seal performance without the pump could not be investigated on this rig.

6.2 Instrumentation

(i) Pressure

Initially there were four 1mm pressure tappings on the mercury rig. The tappings for pump delivery pressure, upper neckring and lower neckring pressures were situated in an identical position to those on the water rig. The fourth tapping measures the pump inlet pressure. This is located on a plunger which protrudes through the bottom of the mercury sump on the axis of the pump shaft. These tappings lead to four separate Bourdon gauges with isolating diaphragms to prevent damage to the Bourdon tubes by the mercury.

Additional tappings were drilled for seal performance trials in the same positions as on the water rig. Unfortunately, the number of these extra tappings was limited by the available space inside the screens surrounding the rig and one of the tappings on the two-stage HDS had to be omitted. The tappings lead via simple gate valves to a manifold connected to another Bourdon gauge with an isolating diaphragm.

All the precautions outlined in Section 4.3(iv) to minimize errors due to dynamic pressure sensing and also the disturbance of internal flow patterns were taken during the drilling of these tappings.

Because of the high density of mercury, a correction for the static head of the gauge above the tapping must be applied to all pressure readings.

(ii) Flowrate

The pump delivered flowrate is measured by two identical Perspex venturis on parallel branches of the hydraulic circuit. Their dimensions were checked by the present author against the specifications for venturi tube flowmeters set out in BS.1042[36] and although there were a few minor deviations, it was felt that the accuracy of flowrate measurements would not be adversely affected. Recent calculations by the present author agreed with the existing calibration curve to within $2\ell.min^{-1}$. See Appendix IV for details of the venturi dimensions and calibration checks.

(iii) Power

The input power to the induction motor is measured by the two Wattmeter method. A correction for motor efficiency is applied to this gross absorbed power figure from the following table, supplied by the motor manufacturer.

Table 6.1: Variation of Motor Efficiency
with Loading on Off-Load Rig

Fraction of Full Load	Load (kW)	Efficiency (%)
$\dfrac{1}{1}$	2.6	85.9
$\dfrac{3}{4}$	2.0	85.4
$\dfrac{1}{2}$	1.3	83.2

The resultant value gives the output shaft power from the motor, which includes losses in the seals and bearings in the rig, in addition to the power absorbed by the pump itself. Since the effect of these losses cannot be estimated, all power data is slightly high.

An alternative method of efficiency (and hence input power) measurement based on thermometric data was investigated during the latter stages of this project (see Chapter 13).

(iv) Speed

Although the three phase induction motor runs at a nominal fixed speed of 1450 r.p.m., the speed is in fact a function of the motor loading. Variations were checked using a Smith's hand-held tachometer applied to the upper end of the motor shaft.

(v) Temperature

The mercury temperature in the pump tank was checked with a simple mercury-in-glass thermometer during pump and seal performance trials.

The Hewlett Packard quartz crystal thermometer described in Section 4.3(v) was used for thermometric efficiency measurements. The mercury temperature at the pump inlet was monitored by one probe, sealed, as on the water rig, inside a length of polythene tubing with the tip protruding. This arrangement permitted the probe to be immersed in the mercury pool and located close to the pump suction plate, without damage to the stainless steel cable sheathing.

The pump outlet temperature was measured at the top bend in the delivery pipe. Although this introduced a slight error due to heat losses along approximately 1m of exposed pipe, the probe could not be located elsewhere due to space limitations imposed by the safety screens and the pump tank.

CHAPTER 7

MEASUREMENT AND ANALYSIS OF PUMP PERFORMANCE IN MERCURY

7.1 Experimental Procedure

The drive on the Off Load Rig (O.L.R.) is provided by a single speed three phase induction motor, so it was not possible to vary the rotational Reynolds Number during these trials by altering the pump speed. The change in kinematic viscosity of mercury with temperature is also slight (see Figure 4)[37,38] so little variation of rotational Reynolds Number was actually attained. Tests were carried out at $20^{\circ}C$ and $55^{\circ}C$, to check for effects due to thermal expansion, an upper limit of $55^{\circ}C$ being imposed because of the hazards of mercury vapour at high temperatures. Since the results from both tests were similar, within the limits of experimental error, no further elevated temperature runs were performed.

As far as possible, all measurements taken during the water rig trials were duplicated on the mercury rig, for purposes of comparison. The main problem here lay in assessing the rate of neck-ring leakage. The metal tray described in Section 6.1 for collecting the leakage flow was of necessity very shallow ($\sim$25mm deep). It was also extremely heavy when full of mercury, and these two factors caused considerable difficulty in lifting the tray out of the tank without spillage, so that the mercury could be decanted into a graduated cylinder. Thus the volume of fluid in the tray was kept to a minimum and the time of collection was limited to 10 seconds. Such short periods of time and small volumes of fluid are detrimental to the accuracy of the final calculated leakage rate (see Appendix IV).

A second source of error lay in the splashing of mercury in the pump tank. The water covering the mercury became extremely murky

71.

at high temperatures or high flowrates when sediment in the pipework was disturbed, so that the entire operation of diverting the leakage flow into the tray and out again was carried out blind. It was impossible to tell whether mercury was splashing out of the tray, or even into the tray from the jet of fluid leaving the return pipe of the main hydraulic circuit.

Finally, one should question the assumption that the distribution of the leakage flow between the two holes in the support tube is constant. Measurements from the two tubes were taken consecutively and the results were added to give the total leakage rate. Thus, if the distribution changed during the course of the two operations this would introduce a further source of error. The volumes of mercury collected from each of the two tubes during a given time interval were generally equal to within 10%, which gives a good indication of the possible size of error involved.

Pump trials with increased neckring clearance were not possible on the O.L.R., due to the limited workshop time available at I.C.I. for pump modifications.

7.2 Characteristic Performance Curves of the Standard Pump

7.2.1 Head Characteristics

The dimensional head/flow curves for the pump operating at a nominal 1450 r.p.m. in clean mercury are presented in Figure 84. This figure contains four sets of results:

(1) Operation on the O.L.R., modified as described in Chapter 6, at 20°C.

(2) Operation on the modified O.L.R., at 55°C.

(3) Results obtained on the same rig in May 1977, before modifications were put in hand.

(4) Data extracted from the chlorine plant maintenance manual[39], published internally by I.C.I.

Note that when the pump is operating in the plant, pumping sodium/
mercury amalgam, the characteristic curves may not correspond exactly
to those of Figure 84, as the properties of pure mercury are altered
by the presence of sodium (see Section 3.1).

The results obtained on the modified rig at $20^{\circ}C$ and $55^{\circ}C$ are
almost identical, exhibiting a continuous falling characteristic
throughout the range of attainable flowrates. Since the effect of
temperature change appeared to be negligible, it was deemed unnecessary
to carry out further tests at elevated temperatures. There is, however,
a marked discrepancy between the developed head in cold and hot mercury
at a flowrate of $143\ell.min^{-1}$, suggesting the occurrence of cavitation at
the pump inlet. According to the calculations set out in Appendix VII,
which were based upon an extrapolation of Figure 3, this is likely at
both temperatures, but will be more extensive at $55^{\circ}C$ on account of the
20-fold increase in vapour pressure of mercury above its value at room
temperature. Cavitation is unlikely at $119\ell.min^{-1}$ flowrate, which is
the last point along the head/flow curve where data for hot and cold
mercury coincides.

Although cavitation could be suppressed at all attainable pump
flowrates by maintaining the pump immersion below 22cm (see Appendix VII),
this is not possible at the maximum flowrate, since so much mercury is
held up in the pipes of the hydraulic circuit (which do not run full
at lower flows). The cost of supplying a sufficient volume of this
fluid would be prohibitive. Therefore any data obtained on the O.L.R.
at flowrates exceeding $119\ell.min^{-1}$ is unlikely to represent the true pump
characteristics.

Measurements taken before the rig was modified give a slightly
flatter head/flow curve at low flowrates, which drops more steeply at
the right hand end of the characteristic. The inconsistency between data
for increasing and decreasing flowrates suggests that once again fluid
was held up in the pipework, causing inadequate submersion of the pump
at high flows.

Surface friction losses might constitute another source of
error, since the tapping for pump delivery pressure was situated about
one metre along the outlet pipe before the rig was modified. These
losses will become more apparent at high flows, since they are
proportional to the square of fluid velocity[40].

$$i.e. \quad H_f = f \frac{L}{D} \frac{c^2}{2g} \qquad \qquad ... (7.1)$$

However, even at maximum mercury flowrate H_f is only 0.01m and
negligible in comparison with the discrepancy of 0.4m between the
two sets of results.

Calculations based on a method suggested by Wyler and Benedict[41]
have also shown that any error introduced by oversize pressure tappings[28]
(approximately 6mm I.D. on the original rig) would be less than 0.3mm
of mercury, which is also negligible. Therefore, the incompatibility
of results obtained on the modified O.L.R. and those collected prior to
rig modification is attributed mainly to inadequate pump submersion in
the latter case.

According to the I.C.I. chlorine plant maintenance manual, the
characteristic head/flow curve has a positive gradient at near zero flow-
rates. This behaviour was also apparent, but to a lesser extent, during
the trials in 1977 on the unmodified Off-Load Rig (discussed in the
preceding paragraph). However, the most recent tests resulted in a
falling head characteristic at all values of flowrate. Furthermore,
the values of delivery head indicated by the manual are up to 10% higher
than those found during the present project.

In an attempt to clarify these anomalies, the author contacted
the I.C.I. employee who compiled the data for the plant manual and
obtained the following information regarding measurement of pressure
and flowrate. The pump delivery pressure was gauged by the height of
a column of mercury inside a vertical pipe (8m long and of unknown I.D)

connected to the pump exit. The flowrate was calculated from the time taken to fill a 6 litre collecting box. Note that this time would be less than 10 seconds at the maximum flowrate of $63\ell.min^{-1}$, leading to an error of up to 10% if a simple stopwatch reading to the nearest second were used.

These somewhat unorthodox and inaccurate methods of pressure and flow measurement help to explain the deviation of the graphs in the plant manual from those obtained in more recent trials. It is probable that the latter results give the most accurate indication of the true head/flow characteristics of the pump.

7.2.2 Absorbed Power and Efficiency Characteristics

The dimensional absorbed power and efficiency curves for the pump operating in mercury are presented in Figure 85. Data for these was obtained from:

(a) Runs at $20^{o}C$ on the modified O.L.R. carried out by I.C.I. personnel on 30.6.78, after the Wattmeter connections for the initial trials by the present author on 20.6.78 were found to be faulty.

(b) The I.C.I. chlorine plant maintenance manual[39].

As discussed in Section 6.2(iii), a correction factor has been applied to all gross power measurements to allow for motor efficiency, but losses in seals and bearings have not been taken into account. This introduces a positive error of unknown magnitude into all absorbed power data, thereby reducing the apparent pump efficiency.

Although the initial Wattmeter measurements by the present author, at mercury temperatures of $20^{o}C$ and $55^{o}C$, were incorrect, they showed that, relative to the accuracy of these instruments, the effect of mercury temperature on the pump absorbed power is negligible. The data obtained on 30.6.78 (see (a) above), therefore applies to both hot and cold mercury operation.

The pump absorbed power is a minimum at zero flowrate. The curve exhibits a maximum gradient at about $60\ell.min^{-1}$, peaking around $120\ell.min^{-1}$ and falling off at higher flowrates. This peak occurs prior to the point of cavitation inception discussed previously and the absorbed power would continue to rise with increasing flowrate if such behaviour were suppressed.

The curve extracted from the plant manual deviates considerably from the results described in the preceding paragraph. This is partly because the graph refers to gross power absorbed by the pump and motor combined, which is the value of prime interest to plant engineers. Therefore a correction factor for motor efficiency, estimated from Table 6.1, has been applied to the manual data, and the corrected results have also been plotted in Figure 85. Although the order of magnitude of the nett absorbed power values from the manual and those measured on the O.L.R. are now similar, there remains a discrepancy between the gradients of the two curves, which coincide only at a flow-rate of $20\ell.min^{-1}$. This cannot be explained without further details of the test rig, instrumentation and pump motor used for the original trials and such information is no longer available. It has therefore been assumed that the O.L.R. data obtained on 30.6.78 supplies the most accurate indication of the pump power requirements for operation in mercury, (except at maximum flowrate).

The efficiency curve of Figure 85 has been calculated from the pump output power values measured by the present author and the absorbed power characteristics obtained by I.C.I. personnel on the O.L.R. (see (a) on p.75). A maximum efficiency of 47.5% is attained at $120\ell.min^{-1}$ flow-rate. Note that when the pump is operating in the plant at its so-called design point of $55\ell.min^{-1}$, the efficiency is less than 37%.

Efficiency figures from the chlorine plant manual have also been plotted on Figure 85. Since the original curve refers to combined pump and motor efficiency, it lies well below the graph representing O.L.R. data. Application of a correction factor from Table 6.1 to compensate

for motor efficiency gives excellent agreement between the two sets of results at flowrates below $45\ell.\text{min}^{-1}$, but above this point the trend of the manual curve is towards a lower efficiency.

Measurement of the temperature increment across the pump presents a feasible, and possibly more accurate, method of calculating pump efficiency, which is particularly suitable for operation in mercury because of the low thermal capacity of this fluid. The technique was studied during the later stages of the research project and details are presented in Chapter 13.

7.3 Comparison of Pump Performance in Mercury and Water

7.3.1 Head Characteristics

Trials by the present author on the modified O.L.R. appear to give the most accurate representation of the pump head/flow character-istics in mercury. Therefore the dimensionless curve in Figure 86 has been computed from this data alone, disregarding the other results in Figure 84. The dimensionless head characteristics in hot and cold water (see Figure 24a) have also been included in Figure 86. Approximate similarity of Re_ω occurs between operation at 3500 r.p.m. in hot water $(Re_\omega = 5.4 \times 10^6)$ and at 1450 r.p.m. in mercury $(Re_\omega = 6.8 \times 10^6)$.

The mercury curve is known to be inaccurate at ϕ values above 4.5×10^{-3} (see Section 7.2.1) and will therefore be discounted in the following discussion.

Similarity of Re_ω suggests that the pump performance in mercury will best be modelled by hot water trials. However, Figure 86 shows that although the hot water and mercury characteristics run parallel above a flow coefficient of about 2.0×10^{-3}, the head coefficient in mercury is some 2.5×10^{-3} higher, corresponding more closely to the cold water results. At lower values of flow coefficient, the mercury curve diverges from the other two, lying approximately 3% above the cold

77.

water curve at zero flow.

This discrepancy at low flowrates is difficult to explain. Research concerned with the effects of viscosity on centrifugal pump performance has been reviewed by Moore [42] , but the work relates to petroleum products and other fluids of higher viscosity than water. In the present case, we are dealing with a liquid of considerably lower kinematic viscosity than water. However, according to Stepanoff[16] , at a constant speed and variable viscosity, the delivered head decreases as the viscosity increases, but the head at zero capacity remains essentially the same, thus resulting in steeper head-capacity curves for higher viscosities. Since the opposite effect has been observed in the present case, this empirical law apparently does not hold for viscosities lower than that of water. Stepanoff does comment that if the impeller diameter is too small for the pump casing, so that there is a large gap between the impeller periphery and the volute casing cut-water, the shut-off head will be lower for higher viscosities. This is because the impeller cannot maintain a normal velocity distribution in the pump casing, since most of the shear takes place at the impeller periphery and a lower generated head results. However, the effect will also be accompanied by a greater than expected head drop at the best efficiency point - a phenomenon which does not occur in the present case.

The following possibilities have been examined as an explanation for the differing head/flow characteristics of the pump in water and mercury.

(i) Instrumentation error

The pressure gauge of the O.L.R. was new and its range was chosen so that no readings fell at the extremities of its scale. The diameter of the pressure tapping was 1mm with square edges, which would cause a negligible error (see Appendix IV). There is therefore no reason to question the accuracy of the pressure readings.

The dimensions of the two venturi tubes were checked against the specifications set out in B.S.1042 Part 1[36]. Although there were certain minor discrepancies, the author does not feel that these would have an appreciable effect on the accuracy of flowrate measurements. Several corresponding values of flowrate and pressure difference were calculated using the appropriate standard equation given in B.S.1042 and these points were plotted as a calibration curve for the venturi tubes. This new curve fitted the existing curve to within $2\ell.min^{-1}$ throughout the range of attainable flowrates.

(ii) <u>Differing Pump Geometry</u>

The dimensions of the pump on the O.L.R. were not checked for exact similitude with the pump on the water rig until the latter stages of the research programme. Initially, measurements from a photograph were scaled up and it appeared that the impeller in the mercury pump was slightly oversize. Recalculation of all the dimensionless characteristic parameters using an impeller diameter of 0.146m gave good correlation between pump performance in mercury and hot water[43]. This theory was subsequently refuted when the pump was dismantled and its impeller was found to be identical to that on the water rig (see Chapter 9 for a comparison of the geometry and surface roughness of the two pumps).

(iii) <u>Surface Amalgamation</u>

Chemical amalgamation between mercury and grey cast iron (the pump fabrication material) does not occur at room temperature, although dissolution of the metal into the mercury may occur above $115°C$[44]. The mirror-like surface appearance of pump components which have recently been removed from mercury/sodium amalgam in the chlorine plant is due entirely to physical wetting of the cast iron by mercury, induced by the presence of sodium. The surface texture sensed by the flowing mercury inside the pump is that of the cast iron itself.

Research by Fleming et al[45] into surface friction effects in mercury flows has shown that the friction factor is only affected when chemical amalgamation takes place between the mercury and surrounding conduit.

In the present case, if the surface finish of the pump impellers and bodies on the water and mercury test rigs are similar, the boundary layer losses due to skin friction should be the same for equal rotational Reynolds Numbers. No equipment was available at I.C.I. for measuring surface roughness, but visual inspection confirmed that the condition of the pump on the O.L.R. was not superior to that of the water pump. In order to reduce friction losses to the extent illustrated in Figure 86, the improvement of surface texture on the O.L.R. pump as compared with the water rig pump would be visible to the naked eye.

(iv) Differing Entry Flow Conditions

The volumetric leakage rate through the upper neckring at a given speed and flowrate is considerably higher when the pump is operating in mercury rather than in water, particularly at low delivery flowrates (see Figures 34, 35 and 89). Assuming that the ratio of upper and lower neckring leakage rates is constant regardless of the test fluid, any adverse or favourable influence of the leakage flow on pump performance will be more pronounced when the test fluid is mercury.

There are two possible effects of leakage from the lower neck-rings. It seems most likely that high velocity fluid jetting from the annular clearance between the seal and pump casing (see Figure 1) would form a blockage around the circumference of the impeller inlet, restricting the available flow area for fluid entering the pump. A study of the inlet velocity triangles (see Appendix II) shows that the consequent increase in absolute inlet fluid velocity (c_1) will cause an increase in the whirl component ($c_{\omega 1}$). Now the theoretical pump head is given by the Euler equation:

$$H_r = \frac{1}{g}(u_2 c_{\omega 2} - u_1 c_{\omega 1}) \qquad \ldots (2.1)$$

Thus an increase in $c_{\omega 1}$ would produce a reduction in pump delivery head. The opposite effect occurs in the present case, where a higher leakage rate is accompanied by a higher delivery head.

A second possibility is that the high velocity leakage flow
is diverted into the impeller inlet, where part of the dynamic pressure
is recovered, causing an increase in output pressure. The velocity of
mercury leaking through the seal clearance at zero pump flowrate (see
Figure 89) is $8.6m.sec^{-1}$, which gives a dynamic pressure equivalent to
3.8m of mercury. Because of the lower rate of leakage, the dynamic
pressure of water leaking through the seal clearance at the same point
of operation is only 2.0m of fluid. Partial recovery of the extra
dynamic pressure head would account for the different head/flow
characteristics observed during water and mercury operation at low
flowrates and this theory is supported by the computed increase in
hydraulic efficiency of the pump with increased seal clearance in
water (see Chapter 5.5).

As the pump flowrate increases, the leakage rate falls more
rapidly in mercury than in water (Figure 89), so that the disparity
between the leakage rates is reduced. Furthermore, the dynamic heads
involved form a lower percentage of the total delivery head. These two
facts would explain the closer correlation between water and mercury
characteristics at high flowrates.

It is worth noting that the pump inlet pressure on the O.L.R.
showed rapid fluctuations of the order of $\pm 3450N.m^{-2}$ when the control
valve was closed to give flowrates lower than $60\ell.min^{-1}$. The water
and mercury characteristics start to diverge at about $40\ell.min^{-1}$. Such
pressure variations indicate disturbed flow conditions at the pump
inlet, the presence of which also endorses the above hypothesis.

(v) Through-Flow Reynolds Number Effects

Comparison of the pump performance in water and mercury based
on Reynolds Number effects is complicated by the turbulent/smooth
transition conditions which exist for the water tests (see Chapter 5.2.1).
High speed hot water trials give the nearest equality of Re (both

rotational and through flow) to mercury operation, but in fact the pump behaviour in mercury and cold water correspond more closely.

Using the Hutton criteria[29] for determining the flow regime within the pump when it is operating at maximum efficiency in mercury, we obtain:

$$\frac{28\nu}{W} = 1.8\mu m.$$

$$\frac{224\nu}{W} = 14.51\mu m.$$

Assuming similar surface textures on the water and mercury pumps (see Chapter 9):

$$\lambda_s = 17\mu m.$$

Since $\lambda_s > \frac{224\nu}{W}$, flow within the impeller is fully rough/turbulent for mercury operation.

The discrepancies between the curves in Figure 86 may be explained by changes in friction factor with Re similar to those illustrated for pipe flow in Figure 25b. Nikuradse[23] found that for a relative roughness $(\frac{\lambda_s}{D})$ less than 0.008, the friction curve passes through a maximum in the transition regime, so that losses in the completely rough regime are lower. Thus it is possible to have similar values of C_f for pump operation in mercury (fully rough) and cold water (transition dip), with a higher C_f value in hot water (transition maximum). As the pump flowrate is reduced, thereby decreasing the blade Reynolds Number, friction losses in mercury remain constant, or may even fall slightly as shown in Figure 25b, whilst losses in cold water must increase as the 'smooth' law becomes operative: hence the higher head coefficient at low flowrates in mercury.

The above hypothesis must be treated with some reservation.

82.

Figure 25b refers to artificially roughened pipes; the type of
roughness generally encountered in practice (i.e. "commercially rough")
usually leads to a more gradual transition between the smooth and
fully rough regimes, without the marked transition dip[46]. Likewise,
Bobok [22] was unable to detect a transition dip when he investigated
wall roughness effects on the losses in centrifugal pumps. However,
these experiments were based on changes of Re due to speed, whereas
the present project has shown that this is not equivalent to the
changes of Re caused by viscosity variation, which appears to give
more pronounced secondary effects (see Chapter 5.2.1).

As previously discussed in Chapter 3.2, surface friction losses
will also vary with the roughness profile and spacing. In addition,
the non-uniform shape of channels in turbomachinery, combined with
unsteady flow conditions, complicates the analysis of frictional losses
within a pump. Despite these limitations, variations in surface
friction coefficient associated with viscosity-induced changes in
through-flow Reynolds Number was shown in Chapter 5.2.1 to affect the
pump head characteristic in water. Extension of the same argument to
the fully turbulent conditions in mercury may explain the dissimilar
pump head characteristics in the two fluids.

7.3.2 Power Characteristics

The dimensionless absorbed power curve for the pump operating in
mercury, calculated for data obtained on the O.L.R. (see Figure 85) is
presented as Curve A in Figure 87. Warm rather than hot water results
have been included for comparison (Curve C) since the upper neckring was
thought to have been rubbing during hot water tests at low flowrates
(see Chapter 5.2.2).

Absorbed power measurements on the O.L.R. included parasitic
power consumption in bearings and seals, whereas such losses are virtually
absent on the water rig. There are no facilities on the O.L.R. for
quantifying this additional power requirement and hence Curve A for

mercury lies 15-25% above the scatter band of Curve C. Although small changes in parasitic torque may occur on the O.L.R., due, for example, to variations in side and thrust loads on bearings when the pump operates away from its design point, an approximate value has been estimated as follows.

Pump performance trials in water with increased seal clearance have shown that the overall effect of a higher leakage rate is to increase the pump absorbed power at zero delivered flowrate and decrease the absorbed power at maximum flows (see Figures 58-61). Because of the greater seal leakage rate in mercury as compared with water (Figure 89), the nett absorbed power coefficient of the pump on the O.L.R. should be higher than that of the water pump at ϕ=0. Therefore the difference in power coefficient values for the two fluids at this point of operation (shown in Figure 87 as $\Delta\kappa$= 0.115 x 10^{-3}) identifies the upper limit for parasitic power consumption on the O.L.R. as 350W at 1450 r.p.m. Similarly, the power coefficient in mercury should be lower than in water at the right hand end of the characteristic (disregarding results where cavitation is known to have occurred) and therefore the minimum value of parasitic power, corresponding to $\Delta\kappa$ = 0.055×10^{-3}, is 157W at 1450 r.p.m. The mean of these two limiting values is 242W[$\Delta\kappa$ = 0.085×10^{-3}], which has been subtracted from the experimental power data on the O.L.R. to obtain the nett power characteristic of the pump in mercury, marked as Curve B on Figure 87. The accuracy of this curve is unlikely to be better than $\pm$6%, since the error in the parasitic torque figure may be as high as $\pm$30%.

In view of this uncertainty, a detailed analysis of the results in Figure 87 would not be justified. The main point illustrated is that the higher seal leakage rate in mercury leads to greater pump power requirements than in water at a given speed and low flowrates. Because the power characteristic is steeper in water, the power consumption in the middle flowrate range, which is of most interest to plant engineers, is similar for both fluids and may actually be lower in mercury at maximum flows.

7.3.3 Efficiency Characteristics

The dimensionless efficiency/flow characteristic for pump operation on the O.L.R. is presented in Figure 88 (Curve A). The curve lies below the scatter band of corresponding results in hot water (Curve C) with a maximum difference of about 4% in efficiency values because of the additional mechanical losses on the mercury rig. Curve B in Figure 88 represents the nett pump efficiency characteristic, which has been corrected for parasitic power consumption using the figure calculated in the preceding section. If the possible error of $\pm 1.5\%$ on this curve is taken into account, agreement between the mercury and hot water results is remarkable.

7.3.4 Neckring Leakage at Standard Seal Clearance

The upper neckring leakage at the standard seal clearance (0.165mm radial) was measured in mercury at $20^\circ C$ and $55^\circ C$. The poor accuracy due to experimental technique has already been described in Chapter 7.1, but the scatter of results in Figure 89 is acceptable. A single curve has been drawn through all points because any temperature effect (which would be slight since the kinematic viscosity of mercury decreases very slowly as the temperature is raised: see Figure 4) is masked by this scatter. Comparison with warm water results at 1500 r.p.m. shows that the leakage rates are almost equal at high flowrates, but the mercury curve is steeper, so that leakage losses are much higher for low pump flowrates.

The low kinematic viscosity of mercury leads to higher values of Re_u and $Re_{\bar{y}}$ despite a 3% reduction in speed, thereby changing the values of the parameters ζ_{io} and λ which govern the slot flowrate (See Chapter 5.3). It is unlikely that exact similitude of flow conditions in the neckring clearance could be achieved by running the pump in hot water at 5,800 r.p.m. (see Chapter 3.1). Rotational Reynolds Numbers would then be equal, but the general trend of curves in Figure 37 indicates that the seal leakage rates at this speed would not match the range of throughflow Reynolds Numbers that is found in mercury at 1450 r.p.m. $(Re_{\bar{y}} = 1.1 - 2.6 \times 10^4)$.

The magnitudes of Re_u and $Re_{\bar{y}}$ for pump operation in mercury are not encompassed by Weber's empirical relationships for estimating the wall friction and inlet resistance coefficients of the seal clearance slot[35]. Extrapolation of the curves in Figures 36a and b to predict seal leakage rates was not successful, as illustrated in Figure 89. The calculated leakage rates are 10-25% lower than experimental values.

There is a steep axial pressure gradient in the volute of the pump on the O.L.R., as shown in Figure 90. Pressure is always higher above the impeller at the upper neckring inlet, but falls with increasing pump flowrate, whereas the lower neckring pressure varies little.

Since data in this Figure is presented in dimensional form and the pressure head generated by the pump $\propto \omega^2$, pressures in mercury should be approximately 10% lower than for the water results at 1500 r.p.m., which have been included for comparison. A further small decrease in pressure may be attributed to the higher leakage rate in mercury, particularly at low flows. However, the particularly low pressure at the bottom neckring on the O.L.R. is thought to result from a very small axial clearance on this side of the impeller, leading to a high dynamic pressure of the leakage flow. As explained in Chapter 5.3, this clearance cannot be checked once the pump has been assembled and similarity on the two test rigs cannot be guaranteed.

Seal leakage data in mercury has also been plotted in Figure 37 showing a linear dependence on differential pressure across the seal. Water results conform more closely to Weber's formula[35], which predicts that $Q_{s1} \propto [\Delta p]^{\frac{1}{2}}$ (see equation 5.19). The higher leakage rate in mercury as compared with water (at a similar speed) becomes even more apparent when presented in this manner, which emphasises the importance of an efficient sealing mechanism for low viscosity fluids.

The volumetric efficiency of the pump at its duty point of $55\ell.min^{-1}$ in mercury is only 70% (see Figure 91). If the upper neckring

were replaced by a more effective seal such as a HDS (see Chapter 10), an increase of 10% in overall pump efficiency could be achieved. From Figure 85, this represents a power saving of 0.2kW which would partially offset any additional power requirement for the new seal.

7.4 Summary of Results

The main features arising from the foregoing comparison of pump characteristics in water and mercury are summarised below for the convenience of the reader:

1. The existing laws of scaling based on dimensionless parameters can be used to predict the pump delivered head in mercury with an accuracy of at least $\pm 7\%$. This margin of uncertainty is caused either by secondary Reynolds Number effects, which lead to a variation in skin friction losses between the two fluids, or by the partial recovery of dynamic pressure from leakage flow re-entering the pump inlet, or a combination of the two factors.

2. No firm conclusions can be drawn with regard to scaling of pump power requirements, because of uncertainties in the value of parasitic power consumption on the O.L.R., but it is apparent that the higher seal leakage rate in mercury leads to extra power consumption at low flows. An approximate value of the parasitic power has been calculated from a comparison of the measured power characteristic on the O.L.R. with the nett power characteristic of the pump in warm water.

3. The greatest disparity in pump power consumption for the two liquids occurs at zero flow, where efficiency values are unaffected. Consequently, this aspect of pump performance in mercury can be predicted with reasonable accuracy from tests in water, by assuming that it will be about 4% lower over most of the useful operating range (including parasitic torque losses). When an approximate correction for this parasitic torque is applied to the mercury characteristic, to give

nett pump efficiency, the error band of the corrected curve ($\pm1.5\%$) falls within the scatter band of the characteristic in hot water.

4. The low kinematic viscosity of mercury causes a high seal leakage rate, which bears no direct relationship to the leakage in water and affects several aspects of the pump performance, as outlined above.

The concept of scaling data from pump performance trials in water, in order to predict the performance in mercury, is discussed more thoroughly in Chapter 9.

CHAPTER 8

INVESTIGATION OF PUMP SURFACES AND MATERIALS

8.1 Material Specifications

The pump impeller, volute and bellmouth suction plate are
fabricated from grey cast iron (B.S.1452). The advantages of this
material are that it is cheap and easy to cast and machine, combining
a reasonable tensile strength with high compressive strength.

For engineering purposes, the types of cast iron are not normally
specified by chemical composition, but rather by the mechanical properties -
or other special properties - required for a particular purpose. Although
composition is one factor governing these engineering properties,
metallurgical structure and section of the casting must also be taken
into account. Hence the chemical composition is normally left to the
discretion of the founders.

In grey cast irons, the quantity and form of the graphite, and
its degree of refinement together with the pearlite determine the
strength category. This is specified by the tensile strength which
would be obtained with a 30mm diameter bar cast from the melt in
question: i.e. the tensile strength of a grade 10 cast iron would be
10 ton.in^{-2} ($154 \times 10^6 \text{N.m}^{-2}$). Components of the pump body (volute and
suction plate) are sand cast in Grade 12 cast iron, whilst the impeller
is shell moulded in Grade 17 cast iron. In the latter case, the melt
is innoculated before pouring, to refine the graphite structure. After
casting and machining, the impeller necks are induction hardened to a
maximum of 32 Rockwell C.

The neckrings of the pump are fabricated from high duty
carbon steel (Manufacturers specification MS T.152). These components
are case-hardened to a minimum of 80 Rockwell A.

8.2 Metallographic Examination of Pump Components

The impellers and neckrings from 2 worn pumps were examined
in 1974 by the I.C.I. materials laboratory[44]. They found a varying
pattern of hardness in the neckrings (manufactured from grey cast iron
at that time) indicative of a flame hardened surface which had suffered
a considerable amount of wastage. However, there was no correlation
between the varying degrees of hardness and the wastage patterns, so
the loss of metal was not thought to be a function of surface hardness.

The wetted surfaces of the impeller were also found to have
suffered wastage. It was felt that the principal mechanism of wastage
must be the dissolution of the metal surface into the mercury, i.e.
amalgamation. However, examination of a pump impeller at Southampton
appears to contradict this.

8.2.1 Pump Impeller

Figure 92 shows the worn pump impeller*which was brought from
I.C.I. to the University in November 1976 for material investigations.
Deep grooves are evident around the impeller neck caused by debris
which becomes trapped in the annular space between the impeller and
neckring. A graphite sphere from the denuder can also be seen lodged
inside the impeller - this is thought by I.C.I. personnel to be one
source of the suspended particles responsible for neckring wear.
However, a simple abrasion test between one of these spheres and a
mild steel neckring, carried out by the present author, showed that
the graphite wears in preference to the metal.

The surface of the impeller in Figure 92 appears to be extremely
corroded, but examination under a low powered microscope showed that this

* The surface profile of this impeller is not representative of the impellers used
in the present research for pump performance trials.

was mainly due to surface rust. The impeller had been lying discarded in the plant for some time, undergoing atmospheric corrosion. However, the rust was easily removed using a wire brush, without disturbing the underlying surface texture.

The pump impeller was cast in 2 sections. (This method of fabrication is no longer used and the impellers are currently made as an integral casting). The upper section incorporates the vanes and is joined to the lower plate, containing the fluid inlet, by studs. These studs were drilled out and the sections separated to facilitate examination of the inner surface of the impeller. The inner surfaces of the upper and lower sections are shown in Figures 93 and 94 respectively. Much of the apparent corrosion has been caused by atmospheric exposure and is only superficial.

However, in certain areas deep pitting is evident in which the presence of free mercury was detected and undercutting of the vanes has occurred (see Figure 95). This is thought to be a result of erosion by the mercury flow which contains iron and other suspended particles. Although the pitting is reminiscent of cavitation[47], it is doubtful whether this occurs in view of its location. Cavitation would occur first in low pressure/high velocity areas, i.e. at the pump inlet. Figure 96 gives an indication of the extent of surface erosion. In the vicinity of the studs, the surface of the lower section of the impeller has been protected from the flowing mercury, due to close contact with the vanes. In these areas, the original machining marks are still visible on the surface, which contrasts sharply with the rough texture of adjoining unprotected areas.

The impeller was sectioned and mounted for routine metallographic examination. 2% Nital etch was used. Figure 97 shows the general microstructure of the main body of the impeller, which consists of coarse graphite flakes in a ferrite matrix. The almost total absence of pearlite in the structure indicates a high silicon content in the cast iron.

The microstructure in areas which underwent faster cooling rates during casting, such as the vanes, contain a much finer graphite distribution in the ferrite matrix - see Figure 98.

Figure 99 illustrates the mechanism of erosion on the impeller vanes. It is obvious that the soft graphite is preferentially attacked and worn away, causing particles of the relatively harder ferrite to separate from the surface. This could well be one source of the suspended particles responsible for neckring wear.

The spacing of the graphite flakes in the microstructure indicates that the size of the ferrite particles between them would be 0.01-0.1mm diameter. The specified neckring radial clearance is 0.165mm. Thus any slight radial shaft float would cause the larger particles to become trapped between the impeller neck and neckring, resulting in abrasive wear. Figure 100 shows the extent of pitting on the impeller surface. At higher magnification of the same area (see Figure 101), it is again obvious that fracture will occur along the weak graphite flakes, causing separation and removal of the ferrite matrix.

The contrast between the original machined surface of the impeller and an area where mercury erosion has set in, is shown in Figure 102. This type of eroded surface would be extremely rough in high Reynolds Number mercury flows.

It is suggested that a simple modification in pump fabrication material, such as the use of a spheroidal iron, would reduce the rate of wear between the impeller neck and sealing ring, by eliminating the release of abrasive ferrite particles into the circulating mercury. In addition, the smoother surface texture of pump components would improve the overall pump efficiency.

The mismatch between the maximum efficiency point of the pump

and its duty flowrate in the chlorine plant (see Chapter 7.2.2) also contributes to the high rate of neckring wear. Pumps operating in similar erosive liquids at partial loads (i.e. away from the point of maximum efficiency) always show evidence of damage on the wearing rings[48]. Liquid rotating between the shroud and wall of the casing and high velocity flow through the clearance erodes the casing in that area. Therefore, a pump of smaller diameter, with a true design point and maximum efficiency at $55\ell.min^{-1}$ and 1450 r.p.m. would not only be more economic for power consumption (with $\kappa \propto D^5$: see Chapter 3.1) but would also reduce the frequency of plant shut-down for pump maintenance, by improving the useful life of the sealing rings.

8.2.2 Pump Neckrings

Two sets of upper and lower neckring seals from the pump, one set in a new condition and the other worn, were sent to the University for metallographic examination in February 1977. The manufacturer's material specification for these components is MS T.152 (thought to be a high duty carbon steel) and they are case-hardened to a minimum of 80 Rockwell A.

The microstructure of the core of the new upper neckring, as revealed using a 2% nital etch, is shown in Figure 103. This consists of sorbitic pearlite in a ground mass of ferrite. Etching with boiling sodium picrate confirmed that no free cementite was present in the structure.

The structure of the case is shown in Figures 104 and 105. This appears to consist of an outer layer of martensite (white band along the edge) and an inner layer of upper bainite (etching black). Hardness tests confirmed that the white band was martensite and not a decarburized layer. The results of hardness tests carried out on the neckrings are presented in Table 8.1.

93.

Table 8.1: Average Hardness Values of
Pump Neckrings

		Hardness* (V.P.N)		
		Core	Wearing Surface	Outer Surface
Upper Neckring	(New	466	861	826
	(Used	254	374	356
Lower Neckring	(New	586	1001	980
	(Used	502	923	967

* Obtained using 1 kg load.

Examination of the worn upper neckring revealed a structure
similar to that of the new component in both core and case, but with
increased amounts of ferrite present in the core (see Figure 106). This
would probably be due to a slower rate of cooling after heat treatment.
The wearing surface of the worn neckring is deeply grooved, as shown in
Figure 107 which may be compared with the unworn surface of Figure 105.

However, the worn neckring is considerably softer than the new
component, both in the core and in the case (see Table 8.1). It is
unlikely that any martensite is present in the case of the worn seal,
which consists mainly of bainite and pearlite. Therefore either the
fabrication material or the method of heat treatment for the upper
neckrings has been changed during recent years to give superior
mechanical properties.

The structures of both the upper neckrings suggest that they
are manufactured from an alloy steel. Nickel steels are commonly used
for case-hardening components, but it is impossible to tell which alloying
elements are present without carrying out a detailed chemical analysis.

The microstructure of the core of the new lower neckring, etched with 2% Nital, is shown in Figure 108. Pearlite is dispersed in an acicular ferritic groundmass, forming a Widmanstätten structure. At higher magnification (see Figure 109), manganese sulphide inclusions are visible, elongated in the direction of working. The case, illustrated in Figures 110 and 111, consists of an outer layer of martensite and an inner layer of bainite.

The core of the worn lower neckring is shown in Figure 112. The structure is mainly pearlitic, with a little ferrite demarcating the boundaries of the original austenite grains. This indicates a slower cooling rate, with more time for separation of ferrite along grain boundaries, than in the new neckring, where ferrite separated along the crystallographic planes in a Widmanstätten structure. The worn neckring also contains elongated manganese sulphide inclusions, illustrated in Figure 113. The wearing surface of the lower neckring is in a smoother condition than the upper neckring, as shown in Figure 114. The martensitic and bainitic layers are also clearly visible in this figure, hardness tests confirming that the brilliant white band along the outer edge of the specimen is pure martensite (see Table 8.1).

The microstructures of the lower neckrings are typical of a medium plain carbon steel. The worn neckring is not as hard as the new one (Table 8.1) but this could have resulted from the slower cooling rate after the heat treatment, indicated by the grain boundary ferrite. Etching both specimens with boiling sodium picrate confirmed that there was no free cementite in the structure, i.e. the material is a hypo-eutectoid steel.

8.3 Dimensional Measurements of Pump Neckrings

The depth of case-hardening on both sets of neckrings was measured using a microscope graticule. The results are presented in Table 8.2.

Table 8.2: Depth of Case Hardening on Pump Neckrings
(Measured by microscope graticule)

Component	Depth of Case (mm)	
	Wearing Surface	Outer Surface
Upper Neckring (New (Used	0.224 av.0.112	0.168 - 0.224 ** 0.134
Lower Neckring (New (Used	0.448 - 0.560 0.448 - 0.560	0.448 - 0.560 0.448 - 0.560

** Surface is grooved due to machining.

Measurements of the wall thickness of the neckrings were also taken using a ball-ended micrometer screw. Readings were taken at six random positions around the annuli, in order to estimate the amount of material wear. The results are presented in Table 8.3.

Table 8.3: Wall Thickness of Pump Neckrings
(measured using ball-ended micrometer screw)

Component	Wall Thickness (mm)	
	Min.	Max.
Upper Neckring (New (Used	5.46 5.21	5.49 5.69
Lower Neckring (New (Used	3.10 3.10	3.12 3.10

In places, the wear grooves extend more than halfway through the case of the used upper neckring. If we assume that no wear has occurred

on the outer surface of the neckring, then the original depth of case
was 0.134mm. The average depth of case on the wearing surface is now
about 0.112mm, i.e. 0.022mm of material has been lost. This corresponds
to an increase of 15% in the standard radial seal clearance of 0.165mm.
In contrast, a negligible amount of material has been removed from the
used lower neckring, although microscope examination at high magnitude
shows that some surface irregularities are present, probably due to
material wear (Figure 114).

The relative duty lives of the used upper and lower neckrings
are not known, but if these components had been in service for comparable
lengths of time, wear occurs mainly at the upper neckring. This can be
explained by two factors:

(a) the fabrication material of the upper neckring is much
softer and hence less resistant to abrasion;

(b) fewer abrasive particles will be washed downwards
towards the lower neckrings, because of the upward
buoyancy forces exerted on them by the high density
mercury.

Absence of wear at the lower neckrings indicates little or no
radial shaft float, since this would cause the lower seals to wear
slightly faster than the upper seals.

8.4 Surface Topography

The importance of surface roughness in the scaling of fluid
flows, with particular reference to the non-uniform, unsteady conditions
in turbomachinery, has been discussed in Chapter 3.2. The effects of
varying skin friction losses due to changes in fluid viscosity (and
hence throughflow Reynolds Number) have been clearly demonstrated by
pump tests in cold and hot water during the present project (see Chapter 5.2.1).

Whether the pump performance in mercury is a consequence of similar changes in Reynolds Number or of increased seal leakage has yet to be established.

Therefore measurement of the surface texture in flow passages within the pump forms an integral part of the scaling technique. Initial concern that amalgamation of mercury with cast iron would modify the surface profile as examined in air proved unfounded (see Chapter 7.3.1) and it has been assumed that when the pump runs in both water and mercury, the surface sensed by the fluid is that of the impeller itself.

Centre Line Average (C.L.A.) values and surface traces of the impeller shroud and blades were obtained using the Talysurf machine. This instrument, which is suitable for finer grades of surface, makes use of a sharply pointed stylus to trace the profile of surface irregularities. A flat shoe provides a datum. A pick-up, carrying the stylus and shoe, is traversed across the surface by means of a motorised drive unit. Using an inductive transducer, the up and down movements of the stylus relative to the shoe are converted into changes in an electric current. Signals are fed to a graph recorder, which provides a magnified profile of the surface, and an average meter, which shows the C.L.A. values of all irregularities coming within a standardized length of surface. Widely different types of surface may yield the same average index, hence the profile on the graph recorder is as important as the C.L.A.

To facilitate roughness measurements on inaccessible parts of the pump, e.g. inside the impeller, techniques for surface replication were investigated, (see Appendix V). The Talysurf kit proved the most reliable, although (as discussed in Chapter 5.2.1) it is not recommended for surfaces with a roughness exceeding 4μm C.L.A., when the accuracy of replication is said to be less than 10%. Comparison of traces obtained from the original surface and a replica of the same area indicate that, at least in the present application, the accuracy is considerably better than 10% (see Appendix V).

The Talysurf traces show a random surface texture on the pump impeller, so we may discount any anomalies in the value of surface friction losses due to directional roughness such as grooves or waviness. The initial C.L.A. measurement was 7.0μm, but according to subsequent tests, the roughness was outside the limit of the instrument, which is 10μm. However, it was still possible to obtain reasonable traces of the surface profile and these are presented in Appendix V.

The only other instrument available at the University for measuring surface roughness is the Mitronic[18]. With a 1mm radius sphere as a sensor on the stylus, this would smooth out too many irregularities when tracing the impeller surface. More sophisticated equipment was ordered for the Talysurf, to extend its operating range to rougher surfaces and also to analyse the wavelength of recurrent irregularities, but did not arrive in time for this project, so further investigations of the pump impeller surface profile were abandoned.

As discussed in Chapter 5.2.1, a figure of 10μm was taken as a representative value for the C.L.A. of the impeller surface, to substitute into Hutton's formulae[29] for predicting the flow regime within the pump. The approximate nature of the figure is endorsed by the above discussion, but since the roughest areas will govern the flow regime within the pump, the value is thought to be correct to within ±20%.

CHAPTER 9

SCALING OF PUMP PERFORMANCE WITH NECKRINGS

A comparison of the pump performance in water and mercury, as discussed in Chapter 7.3, has shown that the head characteristics in mercury at 1450 r.p.m. can be predicted to within 7% by applying the basic affinity laws described in Chapter 3.1 to values of head generated in water. The absorbed power requirements can be predicted with less accuracy, but this is partly because power measurements on the mercury rig include losses in the motor, shaft bearings and seals, the total value of which can only be estimated to within +30% (see Chapter 7.3.2).

A more precise scaling technique must encompass phenomena that do not depend solely on the Reynolds Number of the main flow, such as skin friction and leakage losses. In order to develop such a technique, experimental data should ideally be gathered from a single pump running in different fluids on the same test rig. If, as in the present case, separate pumps and test rigs are to be used, the following stipulations should apply:

1. The internal geometry of the two pumps must be identical.
2. Measurement facilities on the two rigs must achieve a similar, high accuracy.

To ensure geometric similarity (stipulation 1), it was initially planned to run the same pump on both rigs, but this proved impractical because of mercury contamination. The external dimensions of the impellers on the two pumps used were found to be almost identical, as

shown by the measurements in Table 9.1.

Table 9.1: Measured Dimensions of Water and
Mercury Pumps

	Water Pump	Mercury Pump
Impeller dia. (mm)	143 ± 0.5	143 ± 0.5
Upper hub dia. (mm)	50.65 ± 0.03	50.65 ± 0.03
Lower hub dia. (mm)	69.67 ± 0.05	69.47 ± 0.05

The close similarity indicated in the above Table is assumed to apply equally to the internal dimensions of the pumps, since these could not be checked without sectioning the impellers.

The surface roughness of flow passages inside the two separate pumps should also be similar. No equipment for surface measurement was available at I.C.I. and mercury contamination again prohibited removal of O.L.R. pump components for investigation at Southampton. Although long-term mercury erosion causes pitting of cast iron (Chapter 8.2.1), the surface of the O.L.R. pump, which was new at the beginning of the project, was found by visual inspection to have suffered minimal damage when it was stripped down for fitting of the new seals. Since the water pump was also new, and manufactured at the same plant, the roughness of the as-cast surfaces in both pumps will be comparable.

The second stipulation above concerning accuracy has been met with respect to pump delivered head, but power measurements are less satisfactory. Problems are caused by parasitic torque on both test rigs. The main factor on the water rig is power absorbed in the right-angle gearbox, which is fitted between the torque transducer and the

pump. The value of this parasitic torque can be estimated from a
series of experimentally derived graphs showing its variation with
gearbox temperature and shaft speed (Appendix IV), but relocation
of the torque transducer on the opposite side of the gearbox would
have provided a better solution. Unfortunately, any such modification
was prevented by the geometry of the existing rig design and by cost
limitation.

Absorbed power measurements on the O.L.R. include losses in the
motor, seals and bearings. A correction factor for motor efficiency
may be applied from Table 6.1 (Chapter 6.2), but no facilities are
available for measuring the magnitude of other losses. Unlike the
water rig, where variations in side and thrust loads, imposed when the
pump operates away from its design point, are absorbed by the virtually
frictionless air-bearing, the power absorbed by bearings on the O.L.R.
may change according to the point of pump operation. Since the O.L.R.
motor speed is only nominally constant, small changes in parasitic
torque with speed may also occur. A rough value for the parasitic
power consumption was estimated in Chapter 7.3.2 by assuming that the
effect of increased seal leakage rate on the pump power characteristic
will be similar, whether it is caused by a lower fluid viscosity when
the pump runs in mercury, or by a wider seal clearance in water. Due
to the approximate nature of this figure, the calculated nett pump
power characteristic in mercury involves an error of $\pm 6\%$.

A further stipulation set down originally (Chapter 3.1) for
modelling mercury flows with water was equality of rotational Reynolds
Number on both rigs. This was to be achieved by:

(i) running the water rig at an elevated temperature
    ($75^\circ C$) to reduce the kinematic viscosity of water
(ii) running the water rig at four times the speed of
     the mercury rig, i.e. at 5800 r.p.m.

As previously explained in Chapter 5.1, mechanical problems
limited the maximum speed for obtaining a complete water characteristic
to 3000 r.p.m, but it is now questionable whether true dynamic similarity
would be obtained between pump operation in mercury at 1450 r.p.m. and
in hot water at 5800 r.p.m.

The through-flow rather than rotational Reynolds Number
governs passage skin friction losses, which affect the pump delivered
head. Performance trials in water, discussed in Chapter 5.2.1, confirm
the findings of previous workers[26,30] that changes in Reynolds Number
due to viscosity and speed are not necessarily equivalent. Fluid
viscosity appears to be the major factor, whilst variations in rotational
speed, which alter the velocity of liquid flowing through the pump, has
a minimal effect. Therefore, the restricted range of speed on the
water rig is of less consequence than the inability to reduce the
viscosity of water much below 0.5 cSt (Figure 4).

The variation in dimensionless head characteristic when the
pump runs in water and mercury is attributed in Chapter 7.2.1 either
to differing skin friction losses as a consequence of the higher
Reynolds Number in mercury, or to the effects of a more rapid seal
leakage rate in mercury, or to a combination of both factors. Because
fluid which leaks from the lower neckring jets into the pump inlet
(Figure 1), it is probable that any change in leakage rate will modify
the hydraulic performance of the pump, as well as affecting the
volumetric efficiency.

To test this hypothesis, the dimensionless characteristics of
the standard pump in mercury are compared in Figures 115-117 with those
of the pump running in water with a wider seal clearance than standard
(0.318mm as opposed to 0.165mm radial), so that the leakage rate is
increased for a given speed. Measured values show that the standard
pump leakage in mercury lies approximately midway between that of the
water pump at the standard and increased clearances (see Figure 118),

but unfortunately no water data for an intermediate slot width is available.

The two head curves in Figure 115 are identical in shape and run parallel up to the point of cavitation inception in mercury ($\phi \simeq 4.5 \times 10^{-3}$). The head coefficient is lower in water (by about 5% at shut-off) as a result of pressure losses through the wider seal clearance, but there is a closer correlation between the general form of these two curves than between the dimensionless head characteristics of the pump with standard neckring clearance running in water and mercury (see Figure 86). The power characteristics shown in Figure 116 are also of similar shape, as opposed to the curves of differing gradient which are exhibited by the standard pump in the two fluids (Figure 87). Furthermore, the nett pump power characteristic in mercury (curve B in Figure 116), which has been corrected for the estimated value of parasitic power consumption as discussed on page 102, falls within the scatter band of the power characteristic at 0.318mm seal clearance in water. The corrected efficiency characteristic of the O.L.R. pump (curve B in Figure 117) lies just above curve C for water with increased seal clearance (where the generated head is lower: see Figure 115) and resembles more closely the characteristic for the standard pump in cold water (curve D).

The importance of leakage in pump performance scaling is emphasised by the similarity of the pump head and absorbed power curves with 0.165mm seal clearance in mercury and 0.318mm clearance in water. Therefore, a scaling method which encompasses leakage flow must be investigated. The concept of a total flow coefficient was first discussed in Chapter 5.2.1 and has proved a successful technique for predicting the effect of leakage on pump delivered head at a given speed and water temperature, i.e. where the seal leakage is controlled solely by neckring clearance. Unfortunately, the same approach is less successful when changes in leakage rate are a consequence of varying viscosity. The head coefficient of the standard pump running in water and mercury is plotted against total flow coefficient in Figure 119,

and there is still a wide discrepancy between the two curves at low flowrates.

These results support the hypothesis put forward in Chapter 7.2.1 that the dynamic pressure of leakage jetting from the lower neckrings is partially recovered on re-entry into the pump, thereby increasing the delivered head. They also corroborate the high values of hydraulic efficiency calculated for the pump with increased neckring clearance – see Chapter 5.5.

Since the design of this pump leads to such an unusual inter-dependency between leakage and delivered head, its performance in mercury cannot be predicted accurately from water tests using conventional scaling techniques based on nett flow and head alone. Data from the present research suggests that the general shape of the dimensionless head characteristics in mercury is best modelled by a pump with wider seal clearance than standard, running in cold water. It would be worthwhile repeating the water tests using a pump with a clearance of, say, 0.250mm, in order to achieve equal volumetric leakage rates in water and mercury at a given speed over most of the operating range and again compare the shape of the head characteristics.

The generated head is lower in the water pump with 0.318mm seal clearance than in the mercury pump with a standard clearance (Figure 115) although the two characteristics run parallel. A pair of coordinates (ψ', ϕ'_{tot}) on the mercury characteristic can be predicted from the head/ total flow characteristic of the pump in cold water with standard seal clearance if $4.0 \times 10^{-3} < \phi'_{tot} < 5.0 \times 10^{-3}$, since the water and mercury curves are identical at high flows (see Figure 119). If the leakage rate in mercury is known, or can be calculated, the corresponding nett flow coefficient (ϕ') may be found. When the head characteristic of the water pump with increased seal clearance has been shifted vertically upwards, so that it passes through (ψ', ϕ'), it represents the pump head characteristic in mercury with an accuracy of about $\pm 1\%$.

Accepted techniques for computing seal leakage in water[35] cannot be extrapolated to include high Reynolds Number mercury flows (see Figure 89). In the absence of reliable leakage data, the procedure outlined above becomes unfeasible and the head/nett flow characteristic of the pump with standard neckring clearance in cold water must be used to evaluate (ψ', ϕ') in mercury. Although the two curves are not exactly similar (see Figure 86), the accuracy of the predicted mercury characteristic should still be within $\pm 2\%$, if ϕ' lies between $4.0-4.5\times10^{-3}$.

Measurements of the power requirements of a pump with 0.318mm seal clearance in water give a reasonable indication of the power characteristics of the pump with standard clearance in mercury (Figure 116). If the water tests cover a range of speeds, there will be a wide scatter band ($\pm 4.5\%$ at $\phi=0$, decreasing to $\pm 2.5\%$ at maximum flows in the present case) which results from the change in leakage rate with rotational speed. Comparison of the pump characteristics in the two fluids is complicated by the uncertainty in parasitic torque values on the O.L.R., which introduces a possible error of $\pm 6\%$ at $\phi=0$, decreasing to $\pm 4\%$ at high flows, on the mercury power curve (B in Figure 116). In the middle to high flowrate range, the two error bands overlap, so the accuracy of the pump power characteristic in mercury, as predicted by pump trials in water with a wider seal clearance, will be better than $\pm 5\%$ for $\phi > 2.0\times10^{-3}$, but at low flows the accuracy deteriorates, falling to $\pm 10\%$ at $\phi=0$. As with the head performance, it would be interesting to compare the power curve in mercury with that of a pump running in water, with the seal clearance adjusted to give similar volumetric leakage rates at a given speed in the two fluids.

The efficiency characteristic of the pump in mercury may be predicted to $\pm 1\%$ by the performance of the same pump (i.e. with standard seal clearance) in cold water. This is because the higher absorbed power coefficient at low flowrates in mercury is offset by a

higher delivered head, when the two factors are combined to compute the pump efficiency.

The present attempt to predict the performance of a pump in mercury on the basis of water data is relevant for many industrial and research applications when a rotodynamic machine is required to run in a liquid of low kinematic viscosity such as naphtha, benzene, freon, etc., after acceptance trials in water. The main points which have emerged are:

(a)   Similarity of flow conditions is not necessarily achieved in two liquids of different viscosities by altering the rotational speed of a machine to attain equality of Reynolds Number. Viscosity changes appear to have greater significance than speed changes. This discovery is particularly important for the evaluation of Reynolds Number dependent parameters such as the skin friction coefficient.

(b)   In any design of pump where the seal leakage can interfere with the inlet flow to the rotor, changes in hydraulic as well as volumetric efficiency should be expected in fluids of differing viscosity. In the present case, this effect was found to be more important than any variation in skin friction losses with throughflow and/or rotational Reynolds Number. Since the pump delivered head was actually improved by the leakage flow, the possibility of channelling this leakage into the inlet should perhaps be considered, although the improvement is only noticeable at low nett flowrates (i.e. where leakage forms a high percentage of the total flow) and is therefore of little interest for normal pump applications.

(c)   Seal leakage is a function of both rotational and throughflow Reynolds Numbers in the clearance slot. It is unlikely that simultaneous equality of both parameters can be achieved by running a pump at different speeds in fluids of dissimilar viscosity. This is in addition to the drawback outlined in paragraph (a) above. Therefore, in order to model the effect of leakage on pump performance in a low viscosity fluid, it may be necessary to increase the volumetric leakage rate in water by widening the seal clearance.

(d)   The concept of performance scaling based on a total flow

         coefficient, which encompasses a delivered flowrate plus

leakage, has been investigated. Although it is reasonably successful

for predicting the effect of changes in leakage rate at a given speed

when the seal clearance is altered, the method cannot be extended to

include speed or fluid viscosity changes with any accuracy.

CHAPTER 10

THE HYDRODYNAMIC DISC SEAL

10.1 Introduction

Recent measurements have shown that mercury leakage through
the upper neckring at the duty point of the pump exceeds 20% of the
nett delivered flowrate, even with new seals (see Figure 89). The
standard seal clearance (0.165mm radial) increases through wear during
service, with a consequent increase in leakage rate and fall in pump
efficiency. The leakage flow acquires a high tangential velocity
through contact with the pump shaft and subsequently jets out of the
holes in the shaft casing (Figure 1) causing considerable turbulence
of the mercury and water in the pump tank. This results in the en-
trainment of wash water through the pump, which impairs the efficiency
of the brine cells, as discussed in Chapter 2.5. Therefore, one of
the aims of this project was to design a hydrodynamic seal (HDS)[7,49]
to replace the existing top neckring.

The HDS has been used for several difficult chemical
processes where reliability and zero liquid leakage are necessary[50].
The relatively large clearances and total absence of rubbing/sliding
contact are advantageous in the mercury environment, where the presence
of abrasive particles is thought to be one of the prime causes of wear in
the present neckring seals (see Chapter 8.2). Furthermore, the HDS is
not affected by radial shaft float, which, as discussed in Chapter 5.1,
has often caused problems with the existing face seals. The third
advantage with this type of seal is ease of assembly, which eliminates
the requirement for skilled fitters in the manufacturing plant.

The HDS consists of a disc rotating on the pump shaft (and hence at the same angular velocity as the impeller) in a fixed housing, situated above the pump casing (see Figure 120). The lower surface of the disc is smooth whilst the upper surface is vaned. Liquid which leaks through the annular space between the pump shaft and casing floods into the housing of the seal. Since a steeper pressure gradient exists on the vaned side, a nett pressure differential is produced and the liquid forms a stable interface at some radius R_i on this side. A simplified equation based on the forced vortex may be used to predict the sealing pressure coefficient in dimensionless form:

$$C_p = k_v^2 (1-X^2) - k_s^2 (1 - Y^2) . \qquad \ldots (10.1)$$

The derivation of this equation is given in Appendix VIII, Section 1b.

An important consideration in the design of a HDS is the power consumption, ωM. The equation for torque absorbed by a rotating disc may be written in the form:

$$M = C_M \tfrac{1}{2} \rho \omega^2 R^5 . \qquad \ldots (10.2)$$

In a single stage HDS , $C_M \simeq 0.01$ for well-designed geometry[49], which is two or three times that for a smooth disc and, in contrast to the latter case[51], C_M for the HDS is invariant with Re_ω.

Asymmetric pressure distributions on the two sides of a disc may result in a significant nett end load. The approximate maximum end load may be calculated from the following equation (see Appendix VIII, Section 1d):

$$C_{EL(max)} = \frac{\pi}{2} (1 - Y^2)^2 (k_v^2 - k_s^2) . \qquad \ldots (10.3)$$

Considerable reductions in absorbed torque and end load for the

same sealing pressure coefficient may be achieved by replacing a single disc by several smaller discs running at the same speed[49]. However, this may lessen the permissible radial and axial float on the shaft and reduce the ability of the seal to handle particle-laden liquids, due to smaller clearances. Results on two and three stage seals have been given by Howard[52]. Multi-stage HDS arrangements have been indicated in patents for use with sand and gravel pumps[53] and to lessen the pressure differential on mechanical seals in ultra high speed pumps[54].

One drawback of the HDS is that it provides no sealing action when the shaft is stationary and must therefore be fitted with a back-up static seal, unless a high leakage flow can be tolerated at shutdown, as is the case (transiently) in the present application. This secondary seal may lift off as the shaft rotational speed reaches an adequate value for the HDS to function[55], or for one-shot operation may be allowed to wear out[56]. The operation of a HDS in conjunction with a labyrinth seal has also been investigated[57]

10.2 Seal Design

The main design constraint for the new HDS was the 2.6kW rating of the existing pump motors in the manufacturing plant. Since the standard pump consumes 2.4kW at its duty point (1450 r.p.m. and $55\ell.\text{min}^{-1}$ flowrate), there is little excess power available for a HDS, although savings of up to 0.2kW are theoretically possible through effective sealing of the top shaft clearance (see Chapter 7.3.4).

Staging of the new seal is desirable, because of the power reduction for a given sealing pressure, but a limit of two stages was imposed by the restricted space available for fitting the seal on the pump shaft. Since a single stage seal would be less complex with respect to the number of components and ease of assembly, equivalent

111.

single and two-stage seals were manufactured for comparative studies. Aluminium was chosen as the fabrication material for the seals on the water rig, for ease of construction, but the seals to be tested in mercury had to be made from mild steel, because of amalgamation problems with most other common materials.

General arrangement drawings of the two types of HDS are presented in Figure 121, and details of the dimensions and design parameters are contained in Appendix VIII. The two stage seal was found to leak under certain operating conditions during pilot trials and particulars of a modified version (two-stage (II)) are also to be found in Appendix VIII.

Previous designs of HDS [49, 52, 58, 59] have included provision for a bleed flow from the tip region of the seal housing, but this was deemed unnecessary for the present application, since any heat generated in the seal should pass through the end wall of the housing, to be dissipated by the fluid contained in the pump tank.

It should be noted that the lower neckring is still an integral part of the pump assembly when a HDS is fitted, so that the volumetric efficiency of the pump will not be increased to 100%, even if the HDS does not leak. However, by preventing leakage through the upper shaft clearance, the new sealing arrangement should bring about a substantial decrease in water entrainment through the pump, thus contributing towards the overall efficiency of the brine cells by reducing "thick" mercury formation.

CHAPTER 11

MEASUREMENT AND ANALYSIS OF HDS PERFORMANCE IN WATER

11.1 Experimental Procedure

Minor modifications were necessary to accommodate the new seals above the pump on the existing rig and to test the seals alone. These have been described in Chapter 4.2.

When the seal was running in conjunction with the pump, the air/water interface position in the HDS was controlled by the chosen point of operation on the pump head characteristic, which governs the seal inlet pressure. The pressure gradient across the vaned surface of the sealing disc was monitored by a row of radially-spaced tappings, as shown in Figure 121, which indicated the approximate location of the interface. In previous experiments with a HDS [49,52,59], the interface position has been accurately determined by visual inspection through a perspex housing, but this method was precluded in the present tests by the geometry of the rig, since the top of the seal housing is screened by the cylindrical supporting tube (Figure 11).

Variation in Re_ω was achieved by running at speeds between 1000 rpm (the lowest speed at which pressure measurements were accurate enough to be meaningful) and 2500 rpm, which produced the maximum end load compatible with the air-bearing (Appendix IIIA). Tests at elevated water temperatures were not carried out due to time limitations and the range of speeds for the two-stage (II) seal was restricted for the same reason.

113.

Careful measurements were taken of the pump head/flow characteristics and upper and lower seal inlet pressures at each speed, to see how they were affected by the presence of each seal design. Total input power to the pump and seal was also measured, from which the pump efficiency with the new sealing arrangements could be computed.

The single and two-stage (I) seals were tested alone, using the equipment shown schematically in Figure 122. Inlet pressure was supplied from the water mains, via a Flostat regulator which permitted coarse adjustment of the interface position, but the control afforded by this instrument was disappointing.

In the absence of the compensatory weight of the pump impeller on the shaft, the maximum rated thrust load on the air bearing (see Appendix IIIA) would have been exceeded at speeds above 2000 rpm. This restricted the range of rotational Reynolds Number that could be investigated.

Measurements were taken of the radial pressure distribution across the sealing discs. Data obtained for the nett power absorbed by the bare seals was unreliable, because the parasitic torque absorbed by the test rig gearbox (see Chapter 4.1) accounted for almost 50% of the gross measured torque, even with the single stage HDS at the highest test speed (see Appendix IV).

11.2 Effect of the HDS on Pump Performance

The main differences in performance of the pump fitted with a HDS as compared with the standard pump (Chapters 5.2 and 5.3) are summarised in this section. A more detailed analysis is presented in Appendix IX.

11.2.1 Leakage

Leakage through the upper seal is reduced to zero at all points
on the pump characteristic by the single stage and two stage (II) HDS
The two stage (I) seal leaks slightly at low pump flowrates (i.e. maximum
inlet pressure for a given speed) but is 100% effective at higher flows.

The advantages of a HDS , which reduces leakage to zero with
a substantially greater radial clearance than the original face seal,
are illustrated in the table below.

Table 11.1:   Radial Clearances and Efficiency of
Neckrings and HDS

	Radial Clearance (mm)	η_{vol} (at 1500 rpm and maximum η_{tot} in cold water)
Neckring (standard clearance)	0.165	87%
Neckring (enlarged clearance (1))	0.318	82.5%
Neckring (enlarged clearance (2))	0.636	67%
Single Stage HDS	1.6	unknown for pump with lower neckrings fitted – 100% with HDS replacing both neckrings.
Two-Stage (II) HDS	1.3	

Efficient sealing by the HDS leads to higher pressure at both
the upper and lower seal inlets as compared with the standard pump
(Figures 123-127). This will increase the leakage rate through the lower
neckring. Measurements of this leakage were not taken, but the maximum
increase is estimated to be 6% of the leakage in the standard pump.

11.2.2 Generated Head

The HDS has a beneficial effect on the pump head characteristic,
particularly at high flows, where generated pressure head is greater than
in the standard pump (Figures 128-130). A slight speed effect is

introduced in the non-dimensional characteristic, so that the
conventional laws of head performance scaling for changes of speed
are less accurate than in the standard pump (Figure 21).

11.2.3 Absorbed Power

Total power absorbed by the pump and HDS   is higher than that
of the standard pump at a given duty point, although the extra power
requirement is partially offset by the reduced leakage rate (Figures 131-
133). The two-stage (II) HDS   consumes less power than the single
stage   HDS   for an equivalent sealing capacity (compare Figures 131 and 133):
a detailed comparison of these seals is presented in Section 11.4.

The power requirements of the pump fitted with each design of
HDS   can be scaled for speed changes with an accuracy of $\pm 5\%$.

11.2.4 Efficiency

The efficiency characteristics of the pump with the new seal
configurations are compared with the standard pump characteristics in
Figures 134-136. The curves peak at higher flows than in the standard
pump, because of the increase in delivered head at high flowrates
discussed above.

The efficiency of the pump at the duty point (in the chlorine
plant) and at the best efficiency point is presented for each design
of   HDS   in Table 11.2, which clearly illustrates the advantage of
staging.

116.

Table 11.2:   Effect of   HDS   on Pump Efficiency
in Water.

Tabulated figures give the efficiency of the pump with each seal configuration at the stated operating point (from Figures 134-136)

Operating Point	Standard Pump (neckrings with 0.165mm radial clearance)	Pump with Single Stage HDS	Pump with Two-Stage(I) HDS	Pump with Two-Stage(II) HDS
Duty point ($\phi=2.06 \times 10^{-3}$)	41.5%	28.5%	39.5%	38.5%
Best efficiency	55.0%	40.0%	51.5%	50.0%

Efficiency data for the pump fitted with a   HDS   can be scaled for speed changes using the conventional scaling laws with an accuracy of ±1.5%.

11.3 Comparison between   HDS   Performance Tested Alone and in the Pump

In previous work with a HDS   at Southampton[27,49,52,57], the seal has been mounted on its own for convenience, with an applied loading pressure to simulate conditions in a pump. Without the main pump impeller, there is less whirl in the fluid at the seal entry region and pressure distributions are axi-symmetric, whereas in a volute, some degree of asymmetry is introduced, especially at flowrates well away from the design point. It is therefore of interest to compare the performance of the single stage and two-stage (I) HDS   when tested alone and as part of the pump.

117.

Seal performance is fully described in Appendix X (single stage HDS) and Appendix XI (two-stage (I) HDS). Similar values of sealing pressure coefficient are found for the bare single-stage seal and for the same seal in the pump (Table X(i)). Unfortunately correlation of C_p values for the two-stage (I) HDS in the different configurations is not possible, due to an error in interstage pressure measurement. The pressure distribution across the sealing discs is scarcely affected by the test configuration (Figures 137-138 and Figures 143-144), whilst basic relationships, such as the variation of k_v with Re_ω and with interface position (see Section 11.5) remain unchanged.

The main difference observed for the seal tests in the pump was a slight variation in k_s with interface position, which was absent in the bare seal trials (Figures 141 and 142b). This is thought to be connected with the inlet swirl and asymmetry of pressure distribution at the inlet of a seal running above a pump, because these parameters will change according to the pump operating point (which controls the interface position). The trend is for k_s to decrease as the amount of swirl and pressure asymmetry increases (i.e. at low pump flowrates and high inlet pressures). Low k_s values will improve the overall sealing pressure coefficient by reducing the parasitic pressure rise.

By the same argument, k_s on the single stage HDS and on the lower disc of the two-stage (I) HDS should be lower when the seal runs in the pump than in the bare seal. This is corroborated by the data presented in Tables X(ii) and XI(ii), but further investigation is required because the inlet pressure tapping for the seal/pump assembly was poorly positioned (see Appendix Y). Hence the experimental measurements of parasitic pressure rise, which were subsequently used to calculate k_s, may be inaccurate.

Since a low value of k_s is desirable for efficient HDS operation, the present research confirms that the seal performance is not impaired by fluid swirl or an asymmetric pressure distribution at the inlet. Satisfactory operation in a bare configuration with an applied inlet pressure (for example in seal acceptance trials) will guarantee

equivalent sealing characteristics when the HDS runs in conjunction with rotodynamic machinery.

11.4 Comparison of Single and Two-Stage HDS Performance

The sealing capacity of the two-stage (I) HDS is lower than that of the single stage HDS Although this is mainly because the presence of the shaft was neglected when the radius of an equivalent two-stage seal was first calculated (see Appendix VIII), the detrimental effect of an oversize tip clearance on this seal is also apparent, as demonstrated by the results in Appendix XI.

The performance of the modified two-stage (II) HDS ,where the sealing discs have been enlarged to compensate for the shaft radius and the disc clearances are correct (see Appendix VIII), is fully described in Appendix XII. The sealing capacity is similar to that of the single stage HDS. Both the seals are overdesigned for their intended duty in the mercury pump, since they do not run full at pump shut-off and considerable power savings would result from a small reduction in disc radius (with $P_{in} \propto R_D^5$: see Equation (10.2)) without causing leakage.

The relationship between absorbed power and disc radius leads to the advantage of staging, whereby the power requirement is reduced for an equivalent sealing capability. The benefits are illustrated by the power characteristics of the pump with each design of HDS in Figures 131-133.

In computing the theoretical power saved by staging a HDS (see Appendix VIII), it is generally assumed that $C_M \propto Re^{-1/m}$, leading to the relationship:

$$\frac{P_{in} \text{(two-stage)}}{P_{in} \text{(single stage)}} = 2^{-(\frac{3m-2}{2m})} \qquad \text{... (VIII.18)}$$

The above equation is based on the simple theory of staging, which ignores the sealing performance loss due to the presence of a shaft (see Equation VIII.13), and therefore compares the power requirements of the single stage and two-stage (I) designs.

With values of m between 3 and 5[52], the ratio becomes:

$$\frac{P_{in}(\text{two-stage})}{P_{in}(\text{single stage})} = 0.406 - 0.445 \qquad \ldots (11.1)$$

Experimental absorbed power data for the three designs of HDS is presented in Table 11.3. The figures were obtained indirectly, by comparing the power characteristics of the pump with and without a HDS (see Figure 146). The method is fully described in Appendix X.B.

Table 11.3: Comparison of Power Absorbed by Single Stage and Two-Stage HDS Running in the Pump in Cold Water

HDS	Rotational Speed (rpm)	Re_ω	Absorbed Power (Watts)	C_M	Estimated Error
Single stage	2000	13.4×10^5	181	0.012	$\pm 3\%$
Two-stage (I)	↓	5.9×10^5	55	0.014	$\pm 10\%$
Two-stage (II)	↓	7.4×10^5	71	0.011	$\pm 8\%$

Over the limited range of Re_ω investigated, C_M remains constant for the single stage and two-stage (II) HDS (with allowance for the margin of error in C_M for the two-stage (II) seal). A high C_M for the two-stage (I) HDS is attributed in Appendix XI mainly to its wide tip clearance. Despite this disadvantage, the experimental measurements show that the power consumption of the two-stage (I) HDS is more favourable than the theoretical prediction in Equation 11.1, since:

$$\frac{P_{in}(\text{two-stage (I)})}{P_{in}(\text{single stage})} = 0.30 \pm 0.04.$$

For the modified two-stage HDS, experimental values yield:

$$\frac{P_{in}(\text{two-stage (II)})}{P_{in}(\text{single stage})} = 0.39 \pm 0.04.$$

This is close to the theoretical prediction in Equation 11.1. Therefore, for design purposes, this equation gives a useful approximation of the power saved by staging a HDS even though it is based upon an over-simplification, which ignores the effect of shaft radius.

Air entrainment is another aspect of HDS performance which is neglected by the simple theory of staging. Previous research has shown that gas entrainment is promoted by interface instability[7], which is more evident in a staged seal because of the relatively larger shaft and hole for the shaft in the seal casing. The grooves between the vanes are narrower in relation to disc radius on a multi-stage seal, which will also detract from interface stability (see Appendix XI). Air entrainment and frothing were indicated in the present investigations by a marked change in pressure distribution near the interface on both two-stage seals (Figures 143-145).

Although the problem has not been encountered in previous research with staged seals[52,60], the present measurements show that entrained air collects at the interstage region of the two-stage (I) and (II) HDS This is more prevalent in the two-stage (I) HDS : compare Tables XI(iii) and XII(iii). The process may be facilitated by a wide tip clearance, since entrained air bubbles must be swept across the clearance at the tip of the upper disc before they are carried inward, along the smooth side of the disc, by buoyancy forces and by the secondary, radially inward circulation of water next to the housing wall (see Chapter 12.3.3) to coalesce near the shaft.

Although gas collection near the shaft is not detrimental to the performance of either two-stage HDS in water, there may be other applications where such behaviour is undesirable. For example, in the chlorine plant at I.C.I., the prevention of water entrainment in mercury was one of the main reasons for replacing the existing upper neckring on the pump with a HDS (see Chapter 2.5 and Chapter 12.4). The problem could be solved by providing a bleed flow path from the inter-stage region of the seal. A slow bleed flowrate would have minimal effect on the sealing capacity of the HDS [57] and would carry away any entrapped air bubbles (or water bubbles in the case of the mercury seal: see Chapter 12.3.3) to dissipate in the pump tank (see Figure 164 b).

11.5 Comparison with Previous Research into HDS Performance

The following results from previous research at Southampton University into HDS performance[49,52,59] have been confirmed by the present investigations with seals of optimum geometry (i.e. single stage and two-stage (II) HDS).

(a) k_v and k_s increase with rotational Reynolds Number. This is reflected by a change in the pressure distribution across the sealing discs with varying speed (Figures 137, 138 and 145). For design purposes, 0.96 is generally chosen as a representative value for k_v. On the two-stage (II) HDS, k_v calculated from experimental data was favourably influenced by air entrainment and comparison cannot be justified, but on the single stage HDS, k_v=0.96 was only attained at Re_ω=1.7x10^6 (Table X(ii)) and a value of 0.94 or 0.95 may be more realistic.

(b) C_p is invariant with Re_ω, but depends on interface position. With straight radial vanes, a maximum of about 0.65 with the interface close to the shaft can be expected (Tables X(i) and XII(i)).

(c) k_v at the disc tip falls as the interface moves outwards (Figures 140 and 142a).

Previous work[49] has suggested that $C_M \propto Re_\omega^{1/m}$. C_M was found to be invariant over the limited range of rotational Reynolds number investigated during the present trials and therefore the reduction in absorbed power that is achieved by staging of the HDS is greater than predicted from theoretical calculations based on the above relationship.

The two-stage (I) HDS has a tip clearance of $0.076R_D$, which falls outside the scope of previous investigations. The wide tip clearance is detrimental in many respects: k_v is reduced (Table XI(ii)) C_M is increased (Table 11.3) and the Reynolds Number effect on pressure distribution across the sealing discs is eliminated (Figures 143 and 144). Entrapment of air at the interstage region may also be promoted (see Chapter 11.4).

11.6 Comments on Experimental Technique and Seal Design

11.6.1 Experimental Technique

In previous studies of the HDS [7,52,59], visual inspection of the interface has permitted an accurate determination of its location, together with an assessment of its stability and concentricity. These factors were found to affect the amount of gas entrained through the seal[7], which is of interest in the present project, not only for the general analysis of seal performance, but in particular for the performance in mercury with water inside the interface (see Chapter 12). One of the original specifications for the new sealing arrangement on the mercury pump was the reduction of water entrainment (see Chapter 10.1).

The pump support tube and drive shaft assembly on the water rig (see Figure 6) was intentionally designed to simulate the O.L.R. assembly (Chapter 4.1). The limitations of this configuration, which prevents

observation of the HDS interface, first became apparent in the analysis of two-stage HDS performance in water. Here a particularly steep pressure gradient in the vicinity of the interface was attributed to a radial density gradient caused by air entrainment (see Appendices XI and XII), which would have been conspicuous during the tests if the interface were visible. A transparent seal casing would also permit early detection of gas collecting near the shaft, which is known to influence the seal performance by a local pressure reduction (see Appendices XI and XII). In retrospect, it is felt that the provision of facilities for visual inspection of the internal flow patterns in a HDS is essential for a complete assessment of seal behaviour.

11.6.2 Seal Design

When a HDS is designed for a specific duty - in the present case, operation in conjunction with the pump - there is a critical disc radius for satisfactory sealing capacity combined with minimum power consumption. Since the two-stage (I) HDS absorbs least power and does not leak over the useful operating range of the pump, it is the most suitable of the three designs tested for industrial applications. Experimental results suggest that its performance could be improved by reducing the casing diameter to optimize the disc tip clearance. In addition to increasing k_v and hence C_p on both discs, this would also reduce the torque absorption coefficient C_M.

A further improvement in the two-stage seal performance is suggested by the discussion in Appendix XI concerning the effects of the central hole in the seal casing. The radius of the interstage hole could be reduced to give a shaft clearance similar to the tip clearance of the seal impellers, without losing the wider clearance advantage of a HDS over conventional face seals (see Table 11.1). This would ensure that the lower disc was working efficiently across most of its vaned surface and although a small rise in k_s on the upper disc might accompany the modification, losses due to the additional

parasitic pressure generation would be more than offset by the extra pressure drop across the vanes of the lower disc at small radii. A similar reduction in shaft clearance at the upper seal casing (i.e. at the seal exit) would be expected to promote interface stability, thereby suppressing air entrainment on the upper disc.

CHAPTER 12

MEASUREMENT AND ANALYSIS OF HDS PERFORMANCE IN MERCURY

12.1 Experimental Procedure

The modifications necessary to accommodate a HDS in conjunction with the pump on the OLR have already been described in Chapter 6.1. Changes in the test rig configuration were minimised, because of the limited workshop time available for academic work in an industrial concern such as I.C.I. This restriction illustrates the main drawback of the CASE award system; often the experimental facilities offered by the supporting body are inadequate for the requirements of research at higher degree level. In the present case, no bare seal trials were possible and only the single-stage and two-stage (I) HDS were tested on the mercury rig.

Previous investigations had established that the effect of mercury temperature on pump performance is negligible (see Chapter 7.2), therefore no attempt was made to run at elevated fluid temperatures. The nominal speed of the OLR motor is 1450 rpm, but in practice the speed was slightly lower, because of the additional loading with the new sealing arrangements.

The mercury/water interface position inside the HDS was controlled by varying the point of pump operation and hence the seal inlet pressure. The pressure distribution inside the seal housing was monitored by radially spaced tappings in nominally identical positions to those on the water rig except that one tapping was omitted on the two-stage seal because of limited space (see Chapter 6.2). As on the water rig, visual inspection of the interface was prevented by the rig geometry and its position was indicated solely by the pressure tappings. In this case, however, where

approximately 1m static head of mercury had to be added to all gauge readings to compensate for gauge height, the system was particularly disadvantageous, since any pressure head less than 1m of mercury would not register at the gauge.

The pump head/flow characteristics and upper and lower seal inlet pressures were examined with the two designs of HDS. Measurements of gross input power to the pump and seal permitted calculation of the overall efficiency. The temperature increment across the pump was also monitored during the two-stage seal trials to investigate the feasibility of a thermometric method for evaluating the nett pump efficiency (i.e. excluding efficiency losses due to power absorbed by the seal). The results are presented in Chapter 13.

Water ingestion was found to affect the pump characteristics at high flowrates during these experiments. Severe turbulence was visible in the pump tank at flowrates exceeding $100\ell.min^{-1}$ and all attempts to suppress this, for example by extending the return pipe from the hydraulic circuit with rubber hosing and by increasing the volume of mercury in the tank (up to the maximum amount available in the laboratory) were unsuccessful.

A subsequent investigation into the recommendations for pump sump design has shown that certain features of the sump on the O.L.R. are undesirable if water entrainment is to be avoided[61]. The high velocity return flow from the hydraulic circuit runs freely down the base of the tank and into one side of the sump (see Figure 82) causing an asymmetric velocity distribution which promotes swirl and vortex formation. In addition, water entrainment is encouraged by the mercury stream which jets over the edge of the tank floor into the sump, particularly at high pump flowrates, when the volume of mercury in the bottom of the sump is reduced. Although the above comments also apply to the pump tests described in Chapter 7, water entrainment was suppressed in the initial rig configuration by the proximity of the bellmouth to the sump floor. (According

to Prosser[61], pump performance is optimised for a floor clearance of $\frac{1}{2}-\frac{3}{4}D$, where D=bellmouth diameter). The motor assembly had to be lifted in order to accommodate the bulky HDS above the pump, but changes in the pump characteristics suggest that the floor clearance was also increased, so that mercury flow into the bellmouth became unstable and swirling at high pump flowrates, with consequent water entrainment. The situation is further aggravated by the unsatisfactory arrangements for returning mercury to the sump described above.

The presence of water in the mercury flow delivered by the pump affects both the generated pressure and apparent flowrate (since the latter is measured by a venturi meter, which is sensitive to changes in fluid density). Consequent changes in the pump characteristics calculated from experimental data are discussed in more detail in the following section and in Appendix XV.

12.2 Effect of the HDS on Pump Performance

Important effects of the HDS on pump performance in mercury as compared with the standard pump (Chapter 7.2 and 7.3) are summarised in this section. A more detailed analysis is presented in Appendix XV.

12.2.1 Leakage

The single stage HDS does not leak at any point on the pump characteristic in mercury. The two-stage (I) HDS leaks slightly at low flows, but not at the normal duty point of $55\ell.\text{min}^{-1}$ at 1450 rpm.

The more efficient sealing capability of the HDS compared with the upper neckring leads to higher pressure at the inlet to the upper and lower seals, (Figures 147 and 148). The resultant increase in lower neckring leakage rate will be less than 4% at the pump duty point of $55\ell.\text{min}^{-1}$ at 1450 rpm.

12.2.2 Generated Head

The HDS has a minimal effect on the head generated by the pump in mercury for $\phi < 2.6\times10^{-3}$ (see Figures 149 and 150). At higher flows, the head characteristic of the pump with a HDS falls below that of the standard pump, which is inconsistent with the results of seal tests in conjunction with the pump in water (Figures 128-129).

The apparent drop in generated head is caused initially by water ingestion through the pump inlet, brought about by an increased floor clearance, (see Chapter 12.1). The lower density of a mercury/water mixture as compared with pure mercury will decrease both the pressure generated by the pump and the pressure differential across the venturi flowmeter. Hence the experimental determination of pump head and flow-rate will be inaccurate. By assuming that the head characteristics of the pump fitted with a HDS will be similar at high flowrates in water and a mercury/water mixture, the water content at each data point has been calculated and marked on Figures 149 and 150.

Cavitation has been shown to occur in the standard pump at maximum flowrate on the O.L.R (see Chapter 7.2.1 and Appendix VII) and this will be promoted by the presence of water, which has a higher vapour pressure than mercury. The distinctive sound of cavitation was detected in the present trials at maximum flow, but the inception point may have occurred earlier on the pump characteristic, since the detrimental effects of cavitation and water ingestion are indistinguishable. A flow coefficient of $\phi = 4.0\times10^{-3}$ is thought to be the maximum for which the pump performance represented in Figures 149 and 150 is cavitation free.

The rapid drop in pressure generated by the pump when $\phi > 4.0\times10^{-3}$ reduces the pressure at the inlet to the HDS below the value required to maintain a stable mercury/water interface. The seal then breaks down and water (which covers all free mercury surfaces on the O.L.R. and fills the space around the drive shaft above the HDS: see Figure 1) is pumped by

the pressure rise across the vaned surface of the sealing disc(s) into the pump volute below. It then mixes with fluid from the pump impeller to further increase the water content of delivered mercury. The experimental points where water is flowing through the seal have been marked on Figures 149 and 150.

In theory, the two-stage HDS should function more favourably under these conditions, since an intermediate point occurs in the process of seal breakdown, whereby an interface is formed on the lower disc, the top housing being flooded with water. This interface will be more stable than the interface at the same seal inlet pressure on the single stage HDS because it lies at a smaller relative radius.

In practice, the improved performance of the two-stage seal is barely perceptible, because the operating range over which an interface forms in the lower disc is so limited. This range is indicated by a change in pressure gradient across the smooth surface of the upper disc (when it becomes flooded with water), whilst a steeper gradient on the smooth side of the lower disc shows that it is still flooded with mercury. In Figure 150, the interface lies on the upper disc for the data point at $\phi = 3.3 \times 10^{-3}$, but has moved to the lower disc at $\phi = 3.75 \times 10^{-3}$. At $\phi = 4.1 \times 10^{-3}$, water is flowing through the entire seal.

This malfunctioning of the single and two-stage HDS when running in conjunction with the mercury pump could be avoided by several methods. The seal breakdown is initiated by the collection of water near the shaft below the sealing disc(s), as described in Appendix XV. A bleed flowpath (Fig 164 b) could be incorporated in the seal design, introducing a throughflow from this region that would sweep entrapped water back into the pump tank. If this proved inadequate, small vanes could be incorporated on the underside of the disc(s), which would increase the parasitic pressure rise and force the mercury/water interface to form at a smaller, more stable, radius. Unfortunately, such a modification would inevitably be accompanied by an increase in power absorbed by the seal.

An alternative method is suggested by the work of Wood et al[7].
Here the nett pressure rise across a HDS running in water was augmented
by an applied pressure of inert gas inside the interface. A similar
system of applied water pressure at the mercury interface would allow
greater flexibility of new sealing arrangements on the O.L.R. as variation
of the applied pressure could be used to maintain the interface at a
stable radius.

The solutions outlined above involve extensive modifications to
the existing HDS designs. A simple remedy is to ensure that adequate
pump submersion is maintained, so that cavitation is suppressed and the
seal inlet pressure remains high enough to preserve a stable mercury/water
interface. The duty flowrate of the pump in the manufacturing plant is
approximately 50% lower than that which caused breakdown of the seal and
therefore the problem will not arise during normal in-plant operation.

12.2.3 Absorbed Power

The absorbed power characteristics of the pump fitted with a HDS
and running in mercury are presented in Figures 151 (single stage seal)
and 152 (two-stage (I) HDS). In each Figure, the experimental data has
been corrected for water content in the mercury and replotted as Curve B.

The test rig motor runs on continual overload with the single
stage HDS fitted to the pump. In addition to the extra power required
by the seal itself, the high generated end load increases the parasitic
power consumed in thrust bearings on the shaft assembly. Therefore this
seal is not suitable for the mercury pumps in the chlorine plant, unless
the existing motors are to be uprated.

However, the present motors are adequate to drive the pump with
the two-stage (I) HDS. At the duty point ($55\ell.min^{-1}$ at 1450 rpm), the
gross measured power input to the motor is 2.5kW, which is just below
its maximum rating.

Comparison of the power characteristics of the pump with the two-stage (I) HDS in mercury and water suggests (within the limits of experimental error) that variation in Re_ω due to changes in fluid viscosity do not affect the power coefficient of the HDS. Therefore, data from trials in water on the pump with the two-stage (II) HDS can be scaled up by conventional methods (see Chapter 3.1) to give the power requirements in mercury. In contrast to the two-stage (I) HDS, this seal is 100% effective at all points on the pump characteristic and, with a gross power requirement to pump and seal (including parasitic losses) of 2.56 kW at the duty flowrate, would also be suitable to replace the present upper neckrings without uprating the pump motors (see Appendix XV.C).

12.2.4 Efficiency

The total efficiency of the pump fitted with a HDS is less than that of the standard pump, although the extra power consumption is partially offset by a reduction in leakage: see Figures 153 and 154. In these Figures, Curve B is the true characteristic, corrected for water content in the mercury. It is apparent that the curves are still rising when the HDS begins to malfunction and pump water, so maximum efficiency is not attained.

Efficiency values at the duty point and at the best efficiency point for the standard pump and pump with a HDS are presented in Table 12.1, which shows that the two-stage seal compares well with the standard pump.

132.

Table 12.1: Effect of HDS on Pump Efficiency in Mercury

Tabulated figures give the efficiency of the pump with each sealing
configuration at the stated operating point (from Figs.153 and 154)

Operating Point (at 1450 rpm nominal speed)	Standard Pump (neckrings with 0.165mm radial clearance)	Pump with Single Stage HDS	Pump with Two-Stage (I) HDS
Duty point ($\phi = 2.06 \times 10^{-3}$)	37%	25%	34.5%
Best efficiency	47.5%	>35%	>45%
		(maximum efficiency not attained)	

The drop in efficiency due to the presence of the HDS is generally
less in mercury than in water (compare Table 11.2) because of the notable
gains produced by effective sealing of this low viscosity fluid.

12.3 Comparison of HDS performance in Mercury and Water.

The performance of the single and two-stage (I) HDS running in
conjunction with the pump in mercury is compared in this section with the
results of tests on the same configuration in water (which have already
been presented in Chapter 11). The main differences between the two
systems (mercury with water inside the interface and water with air
inside the interface) are:

(i)   Rotational Reynolds Number on the O.L.R. is five times greater,
      even allowing for the higher speed on the water rig.

(ii) Interfacial tension in the mercury system is about nine times
      greater[62]. (This figure is based on surface tension data for
      tap water and pure mercury. It would be reduced if the mercury
      contained significant amounts of sodium, i.e. if the seal was
      running under plant conditions).

(iii) The viscosity ratio across the interface, outside → inside, is about 1.6 for the mercury/water system and 55 for water/air[40].

(iv) The density ratio across the interface, outside → inside, is roughly 13.6 for mercury/water and 840 for water/air[40].

(v) Absolute similarity between the geometry of seals tested on the two rigs cannot be guaranteed, although they are nominally identical. This uncertainty arises because it was not practical to run the same assembly on both rigs, due to problems of mercury contamination previously mentioned in Chapter 9.

The importance of the different density ratios in the two systems (see (iv) above) has already been demonstrated by the breakdown of the HDS at high flowrates on the QLR. (Chapter 12.2.2). With a density ratio $\rho_m : \rho_w$ of 13.6:1, the pressure rise due to water inside the interface becomes significant as the interface approaches the tip of the sealing disc and water can be pumped back through the seal against the (low) pressure head of mercury at the seal inlet. In contrast, the maximum pressure that can be generated across the vaned surface of the disc in air is 1/1000 of the pressure generated in water (or less than $80N.m^{-2}$ for the single-stage HDS). Therefore, even if the pump submersion were intentionally reduced on the water rig in order to induce cavitation, air could not be pumped through the HDS against a similar pressure head of water and the seal would continue to function normally.

12.3.1 Single Stage HDS

Full particulars of the single-stage HDS performance in mercury are given in Appendix XVI. The main conclusions concerning the comparison with performance in water are summarised below.

The dimensionless correlation of single stage HDS performance in water and mercury, presented in Figure 155, suggests that none of the factors listed in the preceding section has a major influence on the overall sealing performance with a relatively small (and therefore stable)

interface radius. A Reynolds Number effect on local C_p was noticeable for speed changes in water (Figure 137), but the trend is not continued for the high Reynolds Number mercury flows, where the pressure distribution is similar to that in water at high speeds.

Table 12.2: Comparison of Performance Parameters in Water and Mercury: Single Stage HDS in Pump

(Data for maximum seal inlet pressure: $R_i \simeq 0.45R_D$)

Rotational Speed (rpm)	Water		Mercury
	1500	2500	1440
Re_ω	1.0×10^6	1.7×10^6	8.5×10^6
C_p (max)	0.61	0.60	0.60
Average k_v	0.90	0.96	0.93
Average k_s	0.29	0.46	0.33
C_M	0.012±3% (mean value for all speeds)		0.012±11%

Table 12.2 shows that overall C_p is similar in the two fluids, although both k_v and k_s are slightly lower in mercury than the maximum values found for water. For k_v, this is thought to be connected with the relatively wide interface radius ($R_i \simeq 0.45R_D$), since earlier studies on water[49] have demonstrated a marginal fall in k_v when Re_ω is increased beyond 1.5×10^6 for $R_i = 0.65R_D$. If the interface were close to the shaft, k_v would be expected to increase with Re_ω initially and then remain constant at its maximum value.

The low value of k_s in mercury is also a Reynolds Number effect. On the smooth side of the sealing disc, rotational motion is passed on to the fluid by viscous drag and this will be less effective in a low viscosity fluid such as mercury. Unfortunately, existing data in the literature does not extend to such high Reynolds Numbers for comparison.

A weak interdependancy between k_s and interface radius in mercury (Figure 156b) confirms the results from seal tests in conjunction with the pump in water (Figure 141). The true relationship lies between k_s and seal inlet conditions, such as fluid preswirl and pressure asymmetry (see Appendix X.A). These conditions change when the pump flowrate is altered in order to control the interface position.

C_M in mercury was calculated indirectly from Figure 158 (see Appendix XVI) and there is excellent agreement with the value in water (Table 12.2). This shows that the power coefficient of the single stage HDS is invariant in the range $Re_\omega = (1.0-8.5)\times10^6$.

12.3.2 Two-Stage (I) HDS

A detailed analysis of the two-stage (I) HDS performance in mercury is presented in Appendix XVII. The main conclusions which relate to the comparison with seal performance in water are summarised below.

The dimensionless pressure distribution inside the seal correlates well for the two fluids, as shown in Figure 157. Values of the local pressure coefficient, which are not influenced by speed changes in water (see Figure 143), likewise remain unaffected by a change in fluid viscosity. The absence of any Reynolds Number effect for this seal has been attributed to its exceptionally wide tip clearance (see Appendix XI). As in water, where air entrainment alters the pressure distribution near the interface, water entrainment reduces the pressure in the same region when the seal runs in mercury. The problem of entrainment is fully discussed in the following section.

136.

Table 12.3: Comparison of Performance Parameters in Water and Mercury: Two-Stage (I) HDS in Pump

(Data for maximum seal inlet pressure with no leakage: $R_i \simeq 0.5R_D$)

Rotational Speed (rpm)	Water		Mercury
	1500	2500	1460
Re_ω	4.4×10^5	7.4×10^5	3.8×10^6
Lower Disc $\left\{ C_p \right.$	0.62	0.65	0.68
Average k_v	0.89	0.94	0.92
Average k_s	0.41	0.45	0.35
Upper Disc $\left\{ C_p \right.$	0.53	0.51	0.57
Average k_v	0.89	0.89	0.89
Average k_s	0.46	0.48	0.42
Average C_M (both discs)	0.014±10% (mean value for all speeds)		0.013±10%

Table 12.3 shows that C_p on both discs is higher in mercury than in water. C_p for a well-designed HDS is not expected to vary with Re_ω, but a rising trend was found in water on the lower disc (Appendix XI) and this unusual behaviour is attributed to the wide tip clearance of the two-stage (I) HDS. As on the single stage HDS (Table 12.2), the low viscosity of mercury is reflected by smaller k_s values than in water, whereas the k_v values listed in the Table above for the two fluids agree more closely. This will contribute to the superior C_p data for mercury. In addition, there is the favourable influence of pressure generated by water inside the interface on the upper disc, but on the lower disc the exceptionally high C_p value is probably connected with water entrapment at the interstage region and the consequent local reduction in pressure (see Section 12.3.3).

On the lower disc, tip region k_v is an increasing function of Re_ω for both speed and viscosity changes (see Table XVII(ii)), but this relationship is masked in the average k_v values quoted in Table 12.3 by the effect of varying amounts of fluid collecting near the shaft (water in mercury and air in water). All k_v data for the two-stage (I) HDS is unusually low, probably as a result of the wide tip clearance (see Appendix XI).

The accuracy of data for power absorbed by the two-stage (I) HDS in mercury, calculated indirectly from Figure 158 (see Appendix XVII.B), is disappointing. However the high C_M value in water (also attributable to the wide tip clearance of this seal) is corroborated and the figures in Table 12.3 suggest that C_M may rise when Re_ω is reduced below 1.0×10^6.

12.3.3 Interface Stability and Fluid Entrainment

Visual inspection of the fluid interface inside the HDS is not possible on either test rig (see Chapter 11.6.1), but pressure measurements suggest that entrainment of water occurs more readily in the mercury/water system than the entrainment of air when the seals run in water. Experimental evidence is offered by (a) a slightly steeper pressure gradient near the interface of the single stage HDS when it runs in mercury as compared with water (Figure 155), and (b) a rise in tip region k_v as the interface moves outward for mercury operation (Figure 156a) which is contrary to the behaviour in water (Figure 140). These discrepancies are attributed to a radial density gradient on the vaned side of the HDS in mercury, caused by the entrainment of water at the interface (see Appendix XVI) whilst in water, the interface with air is more sharply defined.

Previous research with water[7] has shown that gas entrainment in a HDS is promoted by an unstable interface. This in turn may be caused by several geometric factors, such as the relative size of the shaft and central hole in the seal casing, as well as the shape, size

138.

and number of vanes. The adverse effect of increasing the size of the shaft and casing aperture in relation to the sealing disc radius has been demonstrated during the present project by the occurrence of air entrainment at the interface for both designs of two stage HDS running in water (Figures 143-145), which was not found with the larger, single stage seal (Figures 137-138).

The formation of a smooth, stable interface is facilitated by backward-curving vanes[59]. With straight, radial vanes, which were chosen in the present work for simplicity, the interface will assume a slightly toothed profile, due to the pressure gradient across the channel between adjacent vanes. Pressure is highest at the leading edge of a vane, so the interface will be at the widest radius here, with an approximately linear transition to a position closer to the shaft on the trailing edge of the preceding vane. In addition, curved vanes restrict the secondary circulation caused by radial outflow of fluid next to the sealing disc, with a return flow next to the casing, which also contributes to interface stability. This implies that the problem of entrainment could be reduced in both water and mercury by optimising the vane shape on the sealing discs.

In general, the interface between two immiscible liquids becomes unstable due to the growth of small-scale disturbances at the boundary[63]. Such disturbances will be damped by fluid viscosity and therefore water/air should be the more stable of the two systems, because mercury has an exceptionally low viscosity (Figure 4). However, except at the lowest rotational speed in water, the rotational Reynolds Number for the single stage HDS always exceeds 10^6 (see Table X(i)) which means that the influence of viscosity on interface stability and the consequent entrainment of water bubbles will be small.

The dimensionless number used to predict droplet formation is the Weber Number (We) which is the ratio of inertial to surface tension forces. If We is too high, the inertial force overcomes surface tension,

139.

which is responsible for maintaining a droplet's shape, and the droplet shatters. In a similar fashion to the Reynolds Number, We only becomes important at low values.

The author has been unable to trace any theoretical analyses of water droplet formation in mercury, but some work is available which relates to the entrainment of oil droplets in water[64]. When conventional oil containment booms are deployed in water currents greater than about one knot, oil droplets form at the bottom surface of the slick and are entrained in the water flow under the boom. The existence of a critical Weber Number, We_{crit}, has been postulated, below which no droplets will be formed. Estimates of the value of We_{crit} vary between 14 and 28.

If the same approach is applied to the interface in the single stage HDS, we can compare Weber Numbers in mercury and water. In general:

$$We = \frac{\rho c^2 L}{\sigma} \qquad \qquad \ldots (12.1)$$

where ρ is the density of the dispersed medium, σ is the surface tension between the two fluids, c is the velocity and L is a typical length of the system. The choice of a typical length in the HDS is difficult, although the vane side clearance (s_v) seems most appropriate, since it is here that maximum shear at the interface occurs. An alternative method is suggested in Ref.[64], whereby, for water entrainment in mercury:

$$L = \sqrt{\frac{\sigma}{g(\rho_m - \rho_w)}} \qquad \qquad \ldots (12.2)$$

Here σ is the mercury/water surface tension.

The two methods yield similar results. Using $L = s_v$ (1.8mm) and the tangential velocity of the interface at X=0.5 for c, we obtain:

140.

We(air/water) at 2500 rpm = 4.4

We(water/mercury) at 1440 rpm = 128.

If L is calculated separately for each system from equation (12.2):

We(air/water) at 2500 rpm = 5.8.

We(water/mercury) at 1440 rpm = 145.

The low Weber Number of the air/water system shows that surface tension forces are relatively important and the formation of small air bubbles is discouraged. Therefore the interface is much sharper than for mercury/water, where a high Weber Number shows that inertial rather than surface tension forces prevail, promoting the entrainment of tiny water droplets.

The consequences of different surface tension effects on the water and mercury test rigs are only apparent for the single stage HDS. Other factors, such as interface position and/or unfavourable seal geometry (as discussed at the beginning of this section), have a greater influence on interface stability in the two stage (I) and (II) HDS, where air is always entrained at the water interface, (see Appendices XI and XII). This occurs although peripheral speeds are lower than in the single stage seal, leading to a reduction of Weber Number in both liquids.

An important consequence of droplet entrainment is the collection of entrained fluid at the interstage region of the two-stage HDS. This is verified by a reduction in pressure near the shaft for both mercury and water operation, whereby local k_v calculated from experimental pressure readings exceeds the maximum expected value of 0.96 (see Tables XI(iii), XII(iii) and XVII(ii)).

The mechanism by which droplets are carried from the interface to the disc tip involves the relative magnitude of buoyancy and drag forces (see Appendix XIV). These both depend on droplet radius (r):

141.

$$F_B = \Delta\rho \frac{4}{3} \pi r^3 \dot{c}_r \qquad \ldots (12.3)$$

$$F_D = \pi r^2 C_D (c_{rel})^2 \qquad \ldots (12.4)$$

C_D is a function of Reynolds Number (see Figure XIV(i)), which also depends on the droplet radius. Therefore, there is a maximum size of droplet in each system which can be carried out to the disc tip. The calculations in Appendix XIV show that for the two-stage (I) HDS the diameter of water drops in mercury must be less than 0.6μm, as opposed to 5-6μm for air bubbles in water. However, it is apparent from the foregoing discussion of surface tension effects that the average size of water bubbles in the high Weber Number mercury regime will be much smaller than air bubbles formed in water.

Experimental data concerning the size of entrained droplets is scarce. Anand[59] analysed the size of disturbances at the air/water interface in a HDS with backward curving vanes, and the same vane clearance (s_v=1.3mm) as in the present two-stage seals. At X=0.6, he found 30% of the disturbances were 100μm in diameter, whilst the minimum diameter was 40μm. This is an order of magnitude too large for the transport of air bubbles to the disc tip, but it is unlikely that smaller disturbances would have been visible because a simple photographic technique was used for his investigations.

According to an analysis of water droplet size in mercury on the O.L.R. using a sedimentometer[65], droplets smaller than 5μm are rare. However, this work was carried out before a HDS was fitted on the pump and therefore water was entrained in the leakage flow from the pump neckrings (see Chapter 2.5). Since the shear forces experienced at the interface of a HDS are exceptionally high, the droplet size in the present trials may be reduced by the necessary factor of 10 required for water transport to the disc tip.

Once a droplet has reached the edge of the disc, the rapid

interchange of fluid between vaned and smooth sides (see Appendix XV) will carry it across the tip, whence it will be swept by buoyancy forces and by the secondary, radially inward circulation next to the casing wall, toward the shaft. Comparison of the two-stage (I) and (II) seal performance in water shows that this process is encouraged by a wide tip clearance (Tables XI(iii) and XII(iii)).

The droplets coalesce next to the shaft to form a pocket of air (on the water rig) or water (in mercury). Thereafter the fluid is unlikely to disperse, because the new interface will be at a small radius, where tangential velocities are too low for bubble formation. The wide clearance on the smooth side will also reduce shear forces. The most effective method of removal would be via a bleed flow path from the interstage region, as discussed in Section 12.2.2.

Fluid entrapment does not appear to detract from seal performance, although it may contribute to the eventual breakdown of the seal at low inlet pressures (see Section 12.2.2).

12.4 Suitability of the HDS for Industrial Application in the Chlorine Plant

The wide radial clearance of a HDS as compared with more conventional face seals (see Table 11.1) is particularly desirable on the mercury pump to accommodate run-out on the long, overhung shaft, as well as the presence of small particles in the pumping fluid (see Chapters 2.4 and 2.5). Elimination of leakage through the upper shaft seal was the main reason for replacing the upper neckring with a HDS, since the turbulence caused by leakage flow leads to problems in the chlorine manufacturing process (Chapter 2.5). If the lower neckring were also replaced, the greater clearance of the new seals would be fully available and the end load on the two sets of sealing discs would cancel out.

The two-stage (I) HDS is more suitable than the single stage
seal for industrial application. The staged seal does not leak at the
pump duty point and the total power consumption of the pump and seal
(including motor losses) is less than the rating of the existing motors.
A small amount of leakage must be tolerated at start up and shut down,
but this is acceptable, particularly in view of the present high leakage
rate of seals, even when in a new condition (see Chapter 7.3.4). Leakage
could be checked at all points of pump operation by increasing the radius
of the sealing discs to the size of the two-stage (II) HDS (Appendix XII),
but the concomitant increase in absorbed power does not warrant the
modification.

With the new sealing arrangement, it is important not to exceed
the pump duty flowrate for long periods, to avoid overloading the motor.
The same precaution is necessary to ensure that the mercury/water inter-
face is maintained at a relatively small, stable radius on the upper
disc. This will discourage the entrainment of water droplets, as
discussed in the preceding section. The undesirable effects of entrained
water in the electrolytic processing of brine have already been outlined
in Chapter 2.5 and this is a major cause for dissatisfaction with the
existing pump neckring seals.

The geometry of the two-stage (I) HDS has not been optimised, as
shown by both the water and mercury trials. Several suggestions were put
forward in Chapter 11.6.2 to improve its performance, such as a reduction
of the radial clearance at the sealing disc tips and smaller holes in the
seal housing for the shaft at the interstage region and seal exit. These
modifications would improve the sealing capacity of the HDS without
increasing its absorbed power. In fact, comparison of the seal
performance with that of the modified two-stage HDS (II) in water
suggests that the absorbed power would fall if the disc tip clearance
were reduced (see Table 11.3).

An uprated motor would be required to drive the pump fitted
with the single stage HDS, which is also more bulky (in a radial
direction) than the two-stage design. Therefore it is unlikely that
the use of a single stage seal could be justified in any commercial
enterprise, unless simplicity of design and assembly were paramount,
or limited axial space precluded staging.

CHAPTER 13

THERMODYNAMIC MEASUREMENT OF THE PUMP EFFICIENCY

13.1 Notation

In this Chapter, the traditional symbols for thermodynamic quantities have been used, although they conflict in many instances with the notation listed at the beginning of this thesis. The undermentioned symbols refer to Chapter 13 and the associated Appendices (XVIII and XIX) only:

		Units
A	Area	m^2
c	Fluid velocity	$m.sec^{-1}$
C_p	Specific heat	$J(kg\ K)^{-1}$
D	Pipe diameter	m
E_{CT}	Compressibility energy $(\int \rho [\frac{\partial V}{\partial p}]_T\ dp)$	$J.kg^{-1}$
h	Enthalpy	$J.kg^{-1}$
k	Thermal conductivity	$W(mK)^{-1}$
$k_{\overline{c}}$	Coefficient of velocity distribution	—
K	Pressure coefficient	—
p	Pressure	Pa or bar
P_r	Prandtl No. ($\frac{\mu C_p}{k}$)	—
q	Heat flowrate	$J.sec^{-1}$
Q	Volumetric flowrate	$m^3.sec^{-1}$
r	Frictional recovery factor	—
R_f	Overall recovery factor	—

s	Entropy	$J.kg^{-1}$
S	Stagnation coefficient	-
T	Thermodynamic temperature	K
T_D	Dynamic temperature $(\frac{c^2}{2gC_p})$	K
T'_D	Dynamic temperature $(\frac{c_\infty^2}{2gC_p})$	K
u	Internal energy	$J.kg^{-1}$
V	Specific volume $(\frac{1}{\rho})$	$m^3.kg^{-1}$
Z	Geodetic level	m
α	Cubic expansion energy $(\int [\frac{\partial V}{\partial T}]_p \, dp)$	$J.(kgK)^{-1}$
ΔT	Temperature increment (T_2-T_1)	K
ΔT_{corr}	Temperature increment corrected for heat capacity of associated hardware	K
ΔT_{HC}	Temperature drop due to heat capacity of associated hardware	K
$\Delta'T$	Average temperature difference between a fluid and its surroundings	K
$\delta(\Delta T_M)$	Error in measured value of ΔT	K
η	Thermodynamic efficiency	%
θ	Angular coordinate from flow direction	Rad
λ	Coefficient of heat transfer	-
μ	Dynamic viscosity	cP

Suffices
_____

1	Inlet
2	Outlet
∞	Free stream
m	Mercury
M	Measured
w	Water
Δ	Incremental

147.

13.2 Introduction

The accuracy of the available facilities for determining the nett power absorbed by the pump on both the water and mercury test rigs proved unsatisfactory during the earlier stages of this project. On the water rig, the main source of error lies with the high power absorption of the right angle gearbox, which, for example, accounts for approximately 75% of the gross measured torque when the standard pump runs at 600 rpm (see Appendix IV). On the O.L.R., in addition to the parasitic power consumption in bearings and seals (which is difficult to quantify), the motor efficiency introduces another variable for which an allowance must be made in the two-Wattmeter method of power measurement (see Table 6.1). Therefore a thermometric technique has been investigated as an alternative method of measuring the pump efficiency, which does not require a knowledge of the nett input power to the pump.

The idea of using the temperature rise between the inlet and outlet of a water turbine to measure its efficiency was first conceived by Poirson in 1914. Considerable development in measuring techniques has subsequently been carried out in France[66] and the method has been extended to the measurement of water pump efficiency by several workers at N.E.L. [67,68]. Although the thermometric method has also been applied to a hydrostatic oil pump[69] and has been considered for pumps handling other liquids[70,71], such instances are rare, since insufficient data exists concerning the physical and thermodynamic properties of fluids other than water.

Thermometric techniques for determining the efficiency of hydraulic machinery exhibit several advantages over the more conventional methods. They are relatively simple, causing little interruption to the working of the machine, and require only the provision of thermometer pockets when the plant is first erected. Once the normal performance of a machine has been established (e.g. during acceptance trials), temperature measurements

will give an immediate indication of any change relative to that norm and are therefore useful for continuous performance monitoring.

An accurate knowledge of the flowrate or input power to the machine is unnecessary for the efficiency computation and therefore uncertainties due, for example, to parasitic power consumption or efficiency of the prime mover (as in the present work) are immaterial. In fact, it is possible to measure the rate of fluid flow through a pump or turbine via the thermometric method, if the efficiency of the electrical machine (motor or generator) coupled to the shaft is known[67]. This is particularly useful for on-site tests, where flowrate measurement by normal methods becomes impractical.

At present, thermometric efficiency measurement is only accepted for high head turbomachines (>100m). The small temperature increment produced at lower heads generally causes a higher margin of uncertainty in the final computed efficiency than would be found with other, more conventional methods of efficiency determination, unless highly sophisticated and precise instrumentation is available. However, satisfactory results have been obtained at N.E.L. on a pump producing a head as low as 7.6m of water[72].

For the present research, the temperature rise across the pump running in conjunction with the two-stage (I) HDS was measured in both water and mercury. It was hoped that the results in mercury would be particularly satisfactory, since the low heat capacity of that fluid leads to a temperature rise which is roughly 30 times higher than in water at a similar pump operating point[43].

13.3 Basic Thermodynamic Principles

A small change in fluid temperature results from the losses during energy transfer inside a pump. Figure 159 illustrates on entropy-enthalpy axes the pumping process in which fluid energy is increased from position 1 to 2. Under isentropic conditions, position 2' would be reached, but in

149.

practice, because of energy losses in the system, position 2 represents the condition of the fluid at the pump exit. The efficiency of the pump under steady state conditions is then expressed by

$$\eta = \frac{h_{2'} - h_1 + \{\frac{1}{2}(c_2^2 - c_1^2) + g(Z_2 - Z_1)\}}{h_2 - h_1 + \{\frac{1}{2}(c_2^2 - c_1^2) + g(Z_2 - Z_1)\}} \qquad \ldots (13.1)$$

This expression does not take into account the effects of heat transfer between the pump and its surrounding or of fluid leakage, which are discussed in Section 13.5.

The energy quantities in equation (13.1) are determined from calculations based on the first and second laws of thermodynamics, as follows.

(a)   To obtain the real change in enthalpy $(h_2 - h_1)$ as fluid passes through the pump, we utilize the enthalpy equation:

$$h = u + pV \qquad \ldots (13.2)$$

On differentiation this gives:

$$dh = du + pdV + Vdp \qquad \ldots (13.3)$$

However, $du + pdV = dq = Tds$ (from the first and second laws of thermodynamics). Substituting in equation (13.3):

$$dh = Tds + Vdp \qquad \ldots (13.4)$$

This expression may be expanded as:

$$dh = T\left(\frac{\partial s}{\partial p}\right)_T dp + T\left(\frac{\partial s}{\partial T}\right)_p dT + Vdp \qquad \ldots (13.5)$$

The specific heat at constant pressure is expressed by:

$$C_p = T\left[\frac{\partial s}{\partial T}\right]_p$$

and from the Maxwell relation[97]:

$$\left(\frac{\partial s}{\partial p}\right)_T = -\left(\frac{\partial V}{\partial T}\right)_P .$$

Inserting these values in equation (13.5) and rearranging terms, we obtain:

$$dh = C_p dT - T\left(\frac{\partial V}{\partial T}\right)_p dp + Vdp \qquad \ldots (13.6)$$

On putting into integral form:

$$h_2 - h_1 = \int_{T_1}^{T_2} C_p \, dT - \int_{P_1}^{P_2} T_1 \left(\frac{\partial V}{\partial T}\right)_p dp + \int_1^2 V \, dp \qquad \ldots (13.7)$$

Since $\displaystyle \int_1^2 Vdp = \int_1^2 \{d(pV) - pdV\} = p_2 V_2 - p_1 V_1 - \int_1^2 pdV$

and $\displaystyle dV = \left(\frac{\partial V}{\partial p}\right)_T dp + \left(\frac{\partial V}{\partial T}\right)_p dT$, equation (13.7) becomes:

$$h_2 - h_1 = \bar{C}_p(T_2 - T_1) - T_1\alpha + p_2 V_2 - p_1 V_1 - E_{CT_1} -$$

$$p_2\left(\frac{\partial V}{\partial T}\right)_p (T_2 - T_1) \qquad \ldots (13.8)$$

where $\bar{C}_p$ = mean value of C_p between the temperatures T_1 and T_2

$$\alpha = \int_{P_1}^{P_2} \left(\frac{\partial V}{\partial T}\right)_p dp \quad \text{(cubic expansion energy)}$$

$$E_{CT_1} = \int_{P_1}^{P_2} p\left(\frac{\partial V}{\partial p}\right)_{T_1} dp \quad \text{(compressibility energy)}$$

(b)   The isentropic enthalpy difference of fluid passing through the pump is illustrated in Figure 160. Its value is given by:

$$h_{2'} - h_1 = \int_1^{2'} V \, dp = \int_1^{2'} \{d(pV) - pdV\}$$

i.e. $\quad h_{2'}-h_1 = p_2 V_{2'} - p_1 V_1 - \int_1^{2'} p\,dV \qquad \qquad \ldots (13.9)$

Since $\quad dV = (\frac{\partial V}{\partial p})_T\,dp + (\frac{\partial V}{\partial T})_p\,dT$

we obtain:

$$h_{2'}-h_1 = p_2 V_{2'} - p_1 V_1 - \int_{p_1}^{p_2} p(\frac{\partial V}{\partial p})_{T_1}\,dp - \int_{T_1}^{T_2} p_2(\frac{\partial V}{\partial T})_p\,dT$$

$$\ldots (13.10)$$

The third term in equation (13.10) is the compressibility energy E_{CT}, i.e.

$$h_{2'}-h_1 = p_2 V_{2'} - p_1 V_1 - E_{CT_1} - p_2(\frac{\partial V}{\partial T})_p (T_2 - T_1) \quad \ldots (13.11)$$

(c)   An expression for pump efficiency may now be obtained by substituting equations (13.8) and (13.11) into equation (13.1):

$$\eta = \frac{p_2 V_{2'} - p_1 V_1 - E_{CT_1} - p_2(\frac{\partial V}{\partial T})_p (T_2 - T_1) + \frac{1}{2}(c_{2'}^2 - c_1^2) + g(Z_2 - Z_1)}{\bar{C}_p(T_2 - T_1) - T_1\alpha + p_2 V_2 - p_1 V_1 - E_{CT_1} - p_2(\frac{\partial V}{\partial T})_p(T_2 - T_1) + \frac{1}{2}(c_2^2 - c_1^2) + g(Z_2 - Z_1)}$$

$$\ldots (13.12)$$

13.4 Experimental Technique

Three principal methods exist for efficiency determination by thermometric measurements in turbomachinery[68]. The direct method, which involves the smallest temperature increment and therefore the most precise instrumentation, requires only the measurement of temperature difference

$[T_2-T_1]$ across the machine.

For the partial method, a sample of fluid from the high pressure side (e.g. the outlet on a pump) is ᴧ throttled to a pressure p_3, where [*isenthalpically*] $p_3=p_1$, the pressure on the upstream side, and the temperature difference (T_3-T_1) is measured. One advantage of this technique is that T_3-T_1 is large compared with T_2-T_1, although the effect of inaccuracies in temperature measurement is ultimately the same. The partial method is particularly convenient when it is necessary to avoid inserting a thermometer on the high pressure side of a machine, where it might be damaged.

The null method is only suitable for turbines. Here, a sample of water is drawn from upstream and throttled to the downstream temperature so that $\Delta T=0$. This obviates the need for an accurate knowledge of C_p in the subsequent calculations, and for quantitative temperature measurements. Thus, although the temperature measuring equipment must still be very stable and sensitive, absolute calibration is unnecessary and the thermometers need only to have matched characteristics.

The main drawback of the null and partial methods is that, since the amount of water sampled is small, the effect of heat transfer from surroundings may be considerable, if conduits are not carefully lagged. Therefore, although extreme accuracy of temperature measurement is needed, the direct method was chosen for the present work.

The temperature rise across the pump running in both water and mercury was determined with a Hewlett Packard quartz crystal thermometer. Although the accuracy of absolute temperature measurements with this instrument is only $\pm0.08^{\circ}C$, it is capable of resolving temperature differences between the two matched probes to $\pm0.0001^{\circ}C$ (see Appendix III.B).

The siting of the probe to measure inlet temperature caused some difficulty because the pump runs submerged in a tank on both test rigs

and the probe cable is not totally waterproof. As explained in Chapter 4.3, this problem was overcome by sealing the probe inside a 1m length of polythene piping (to protect the cable) with just the probe sensor protruding. This sensor could then be located close to the pump inlet with the polythene pipe supported manually.

In order to smooth out rapid temperature fluctuations at the inlet probe on the water rig, due to disturbed flow conditions caused by fluid returning to the pump tank from the hydraulic circuit (see Figure 5), a fine mesh grid was fitted across the tank between the pump and return pipe (see Chapter 4.2). The T_1 readout was then found to be reasonably stable, increasing very slowly as the mean water temperature in the tank rose during pump operation (see Appendix XVIII).

On the O.L.R., the location of the inlet temperature probe was dictated by the geometry of the collecting tank and pump assembly (see Figure 82). The probe was introduced into the sump through the only available space, next to the pump delivery pipe, where it was immersed in the return flow of mercury. In this position, the absolute inlet temperature readings were self consistent, increasing steadily with cumulative pump running time (Appendix XVIII).

The outlet temperature probe was situated in the 38mm bore pump delivery pipe. On the water rig (see Figure 5), the probe was about 40cm along the pipe (which was submerged in the water tank closer to the pump), but the intervening length was well lagged to minimize heat losses (see Section 13.5 below). On the mercury rig, space limitations imposed by the safety screens and pump tank meant that the probe was located about 1m along the delivery pipe and no lagging was available. Since the pipe passed through the cooling water in the tank above the mercury and was then exposed to forced ventilation from the extraction hood over the rig, the heat losses were significant. This problem is discussed more thoroughly in Section 13.6.2.

On both test rigs, the effects of frictional heating of the
fluid in the conduit between the pump inlet and temperature measuring
probe were considered and found to be negligible.

When experimental measurements were taken, the pump speed (on
the water rig only) and flowrate were adjusted and allowed to stabilize
beforehand, for a period of at least 5 minutes. A series of 54 direct
readings of ΔT were then taken, between each of which the absolute
temperature at pump inlet and outlet were constantly monitored, to
check for abnormal fluctuations and also to assess the heating rate of
the bulk fluid and rig assembly, (Appendix XVIII). Statistical analysis
was applied to the 54 ΔT values, to obtain the mean measured temperature
increment and the corresponding error band for the 99% confidence interval.[73]
Measurements were taken for selected pump flowrates at a nominal speed
of 1450 rpm in mercury and 2000 rpm in water.

On the O.L.R., the ambient air temperature and the temperature of
the water above the mercury pool were also monitored (with a simple
mercury in glass thermometer) for subsequent heat transfer calculations
(see Section 13.6.2 and Appendix XIX).

Since the two probes had not been calibrated for absolute
temperature, there was a zero error on the ΔT readout, which was determined
in a separate experiment. For this purpose, the probes were immersed side
by side in a large beaker of water, which was kept in the instrument
calibration room of the Mechanical Engineering Department at Southampton
University. Here the environment is controlled to maintain a nominally
constant temperature of 20 $\pm$0.5°C and therefore the likelihood of
convection currents in the beaker of water, caused by external temperature
fluctuations, was minimized. Over a period of 10 days, continuous readings
of ΔT were taken at random intervals of 10-20 minutes, to give a total of
650 values. Statistical analysis of this data gave a mean zero error of
0.0683°C, with an error band of $\pm$0.0002°C (99% confidence interval).
Graphical presentation of the data was also used to confirm the stability

of the instrument and absence of short-term fluctuations in the
temperature readout (see Figure 161).

13.5 Sources of Error

Because of the minute temperature rise across the pump,
particularly in water, any inaccuracy in the measurement of ΔT may lead
to a significant error in the final computed efficiency value. However,
the percentage error in efficiency will be considerably less than the
error in ΔT. This is because the temperature rise depends on the
pressure difference across the pump, as well as the effectiveness of
energy transfer.

If we ignore the minor terms in equation (13.12) (see Appendix XVIII
for relative values):

$$\eta_M \simeq \frac{\Delta p V}{\Delta p V + C_p \Delta T_M} \qquad \ldots (13.13)$$

Then, for a percentage error in measured temperature increment,
$\frac{\delta(\Delta T_M)}{\Delta T_M}$, such that:

$$\Delta T = \Delta T_M \pm \delta(\Delta T_M) ,$$

the corresponding error in η_M is given by:

$$\delta \eta_M = \frac{d}{d(\Delta T)} \left[\frac{\Delta p V}{\Delta p V + C_p \Delta T_M} \right] \delta(\Delta T_M)$$

$$= \frac{-\Delta p V \, C_p}{(\Delta p V + C_p \Delta T_M)^2} \cdot \delta(\Delta T_M)$$

$$= \frac{-C_p \, \delta(\Delta T_M)}{\Delta p V + C_p \Delta T_M} \eta_M \qquad \ldots (13.14)$$

But, from Equation (13.13):

$$C_p = \frac{\Delta p V}{\Delta T_M n_M} (1 - n_M)$$

Substituting in Equation (13.14)

$$\delta n_M = \frac{-\delta(\Delta T_M)}{\Delta p V + C_p \Delta T_M} \cdot \frac{\Delta p V (1-n_M)}{\Delta T_M n_M} \, n_M$$

which, upon simplification, gives:

$$\frac{\delta n_M}{n_M} = -(1 - n_M) \frac{\delta(\Delta T_M)}{\Delta T_M} \qquad \qquad \ldots (13.15)$$

As an illustration, we may take a typical temperature rise on the water rig of $0.02°C$ at a pump efficiency of 50%. For a 10% uncertainty in ΔT_M:

$$\frac{\delta n_M}{n_M} = \pm(1-0.5) \times 0.1 = \pm 0.05 \, ,$$

which means that the accuracy of the computed efficiency is about twice as good as that of the temperature measurement.

The following factors have been considered as possible sources of error in the measurement of ΔT:

(a)   Instrumentation: With a resolution of $0.0001°C$ (see Appendix III.B), the precision of the quartz crystal thermometer is adequate, since the temperature increment varies between $0.02-0.06°C$ in water and $0.3-1.0°C$ in mercury. Thus the main problem with instrumentation lies in the accuracy of the experimentally determined zero error (see Section 13.4). This value was determined immediately after completion of the thermometric measurements in water and may therefore be applied with confidence to

those results. It is less certain to apply to ΔT_M values in mercury because of the inevitable jolting which occurred during transportation of the thermometer between Winnington and Southampton. The zero error correction reduces the smallest measured temperature increment in mercury by approximately 20%: see Section 13.6.2 for further details.

(b)   Heat transfer between the fluid and its surroundings: The effect of heat transfer on the measured temperature increment can be summarized as:

$$\delta(\Delta T) \simeq \frac{\lambda V(\Delta'T)A}{Q\ C_p}$$ ... (13.16)

where $\delta(\Delta T)$ denotes the consequent error in ΔT, $\Delta'T$ is the average temperature difference between the fluid and its surroundings and A is the available area for heat transfer. The constant λ is a function of the geometry of the pump, its thermal insulation and the flowrate and properties of the surrounding media (in this case, air or water).

For industrial applications, with high head and/or flowrate pumps, it is generally the case that either:

(a) Q is large, so, from Equation (13.16), $\delta(\Delta T)$ is small.
(b) ΔT is large, so that $\frac{\delta(\Delta T)}{\Delta T}$ is insignificant.

On the water rig, heat transfer was minimized by effective lagging of the pipework and in addition $\Delta'T$ was always small. The water in the pump tank was at ambient room temperature at the start of a run and the temperature rise of the bulk fluid during continuous pump operation was less than 2^oC per hour.

As explained in the previous section, heat transfer on the mercury rig caused significant errors, because no lagging was fitted and $\Delta'T$ was sometimes as high as 9^oC. An attempt to quantify these heat losses is made in Appendix XIX.

(c)   Thermal stability: Relatively large and rapid changes in the fluid temperature at the pump inlet will introduce uncertainties because of:

    (a) the response time of the temperature sensors,

    (b) the heat capacity of the pump assembly,

    (c) the time the fluid takes to pass through the unit
        from the inlet to outlet temperature measuring
        positions.

    In earlier work at Southampton University[52], an attempt was made to correlate the temperature rise across a HDS for particle laden liquids with the rate of wear of the seal. Because of short term temperature fluctuations, it was impossible to realize the full potential of the quartz crystal thermometer, since a sample period of 10 seconds is required to attain a resolution of $0.0001^{\circ}C$.

    During tests in both water and mercury, the inlet temperature was constantly monitored to check for random fluctuations, but in general none was found. However, the gradual rise in temperature of the bulk fluid, which was sometimes as high as $0.15^{\circ}C$ per minute on the O.L.R., was a source of heat loss, because of the thermal capacity of the pump, delivery pipe and sump, (see Appendix XVIII).

(d)   Recovery Factor: From boundary layer theory, it is known that the temperature T_M measured at a stationary adiabatic probe inserted normal to a flowing liquid is higher than the free-stream temperature T[72,74]. This results from:

    (a) the stagnation effect, due to the isentropic change
        of temperature of the fluid as it decelerates and
        accelerates round the probe.

    (b) the frictional dissipation of kinetic energy of the
        fluid in the boundary layer round the probe.

A correction for these effects may be applied in the form:

$$T_M = T + \frac{c^2}{2gC_p} R_f \qquad \ldots (13.17)$$

where R_f is the overall "recovery factor", which depends on the shape and position of the probe and the Prandtl Number $(Pr = \frac{\mu C_p}{k})$ of the fluid. The value of R_f is best determined empirically for a particular fluid and probe/conduit configuration, but theoretical determination is also possible. The method suggested in Reference [74] was used in the present work to calculate R_f, although this was unnecessary for the majority of ΔT measurements, because the corresponding value of dynamic temperature $(\frac{c^2}{2gC_p})$ was small enough to be neglected (see Appendix XVIII).

(e)   Pump leakage: This only presents a problem if leakage flow is drained from the "system" (i.e. the pump and conduit assembly between the inlet and outlet temperature stations) and lost[75]. If, as in the present case, (since the upper neckring is replaced by a HDS), the leakage (from the lower neckring) flows directly to the inlet and re-enters the pump downstream of T_1, no correction is necessary. Because there is a temperature rise due to friction in the seal, which is trans-ferred to the leaking fluid, this loss will be included in the final calculation of pump efficiency.

(f)   Accuracy of data concerning physical properties of fluids: The physical properties of water $(C_p, V, \alpha$ and $E_{CT})$ are accurately documented over a wide range of temperature[62]. Although the available information for mercury is less detailed, it was found to be adequate for the present requirements[62,76]. The acquisition of such data is often a problem for thermometric measurements in less common fluids[70,71].

13.6 Discussion of Results

13.6.1 Results in Water

The efficiency characteristic of the pump, as determined by thermometric measurements, is presented in Figure 162. The 99% confidence

interval, calculated from the standard deviation of the temperature measurements (see Appendix IV) and Equation (13.15), has been marked for each data point. The results are reasonably self-consistent, with a single outlyer at $\phi=2.43\times10^{-3}$. This represents the first set of measurements taken on the water rig and there is a possibility that the instrumentation had been given insufficient time to stabilize.

The pump was fitted with a HDS for these measurements, but the temperature increment is unlikely to be influenced by the presence of this seal. Heat transfer between the two assemblies was minimized by a thick rubber gasket and any interchange of fluid from the HDS to the pump or vice versa would be very slow. Therefore, the efficiency characteristic according to conventional measuring techniques, which has been included in Figure 162 for comparison, is that of the pump alone. This has been computed from the overall efficiency of the pump with the two-stage (I) HDS (see Figure 135), amended to allow for power absorbed by the seal (data from Table 11.3).

Agreement between the conventional and thermometric curves at or above the flowrate corresponding to maximum efficiency is closer than $\pm 1\%$. Satisfactory thermometric measurements in previous work have generally been obtained near the maximum efficiency point[67,72,74]. This is significant because at lower flowrates, the likelihood of fluid recirculation at the pump inlet increases, so that the T_1 measurement may not be truly representative of the thermodynamic processes involved. In addition, the effect of heat transfer between the fluid and its surroundings is more important at low flows, since $\delta(\Delta T) \propto 1/Q$ (see Equation (13.16)).

These factors may explain the discrepancy between the thermometric efficiency data in Figure 162 and the 'conventional' characteristic for flowrates below the maximum pump efficiency. Although this is disappointing, there are few practical applications where such measurements would be required. The close agreement at high flowrates is more important, and particularly encouraging in view of the minute temperature rise involved ($<0.02^{\circ}C$). Thermal instability of the test rig (e.g.

161.

temperature fluctuations in the tank near to the pump inlet) was originally expected to limit the accuracy of such small temperature measurements, but these misgivings proved to be unfounded.

The present research has shown that thermometric techniques are feasible for measuring the efficiency of a water pump, operating close to its maximum efficiency, for a delivered head as low as 7.5m. Measurements at lower flows are less satisfactory . Therefore the method is particularly suitable for monitoring the performance of a turbomachine during normal, in plant operation. Routine working of the machine is not interrupted (since flowrate measurements are unnecessary) and any deterioration in performance will be indicated directly by an increase in the temperature increment.

A submerged pump need not present problems, if the cable to the inlet temperature probe (which must also be submersed in the sump) can be protected.

13.6.2 Results in Mercury

The results of the thermometric efficiency measurements in mercury are presented in Figure 163, together with the 99% confidence interval calculated from statistical analysis of the ΔT_M data (see Appendix IV). Measurements taken when the pump flowrate exceeded $110\,\ell.\min^{-1}$ have been disregarded (because of the inevitable error introduced by the throughflow of water from the HDS) and the values of the flow coefficient where $Q > 65\,\ell.\min^{-1}$ have been corrected for the estimated water content of the mercury (see Chapter 12.2.2). The scatter of points in Figure 163 is disappointing, since it was originally hoped that this technique would be more successful in mercury than in water, (see Chapter 13.2).

The efficiency characteristic of the pump alone, determined by the conventional method used elsewhere in the project, has been included in Figure 163 for comparison. This curve was computed from the characteristic of the pump fitted with the two-stage (I) HDS running in mercury (see Figure 154), with allowance for the power absorbed by the seal (see Table 12.3).

162.

The mean thermometric efficiency curve lies well above the "conventional" curve. The smallest discrepancy is 4%, which occurs at and above the pump duty flowrate ($\phi \geqslant 2.0 \times 10^{-3}$), but the error increases to roughly +18% at low flows. This implies that the measured temperature increment is too small, due to substantial heat losses from the pump and pipework between the two thermometer probes.

Heat transfer between the mercury and surrounding environment is assisted by the absence of thermal insulation on the pump and pipework (see Section 13.4). The main sources of heat loss are listed below:

(a) Water above the mercury pool in the pump tank is continually replaced during pump operation. The mean water temperature is generally about 2°C lower than that of the mercury. Heat transfer can occur via the pump delivery pipe, which is submerged in the water for approximately 0.5m, and through the sides of the pump body (where it protrudes above the sump). Heat loss through the top of the volute is minimized by the rubber gasket situated between the pump and HDS (see Section 13.6.1).

(b) The O.L.R. is fitted with an extraction hood (as a safety precaution against mercury vapour) which provides a continuous stream of air over the rig components. The temperature difference between the mercury and air is typically 4°C. Heat may be lost to the air from the upper section of the delivery pipe and also from the base and sides of the sump. This latter source of error could be eliminated if the T_1 probe was repositioned close to the pump inlet, rather than in the flow of mercury entering the sump, (see Section 13.4).

An attempt has been made to calculate the likely magnitude of these heat losses (see Appendix XIX for a worked example) and the effect on the final computed efficiency has been marked for each data point in Figure 163. In most cases, if the statistical error in ΔT_M is also taken into account, the thermometric efficiency now coincides with the "conventional" curve.

163.

A further uncertainty lies on the value of the zero error for ΔT readings. As explained in Chapter 13.5(a), this was determined after the thermometer had been transported from Winnington back to Southampton and may have altered during the intervening period. The effect of the zero error varies according to the value of ΔT_M, being greatest for high efficiencies, where ΔT_M is smallest. The decrease in η_M if the zero error correction is omitted has also been marked in Figure 163 for points at both ends of the characteristic.

The combined consequences of heat loss and an inaccurate zero error are more than adequate to explain the discrepancy between the thermometric and conventional efficiency curves. Fluid recirculation at the pump inlet (see Chapter 13.6.1) may also contribute at flows well below maximum efficiency, but this is insignificant in relation to the other sources of error.

It has previously been shown in Chapter 12.2.2 that when $\phi > 2.5 \times 10^{-3}$, the fluid passing through the pump is a two-phase mercury/water mixture. The thermometric efficiency was therefore calculated initially by assuming that the thermal properties ($\bar{C}_p$ and $\bar{\alpha}$) of the mixture are directly related to the relative proportions of the two constituents (see Appendix XVIII.B). Figure 163 shows that this assumption is incorrect and that the efficiency based on the physical properties of pure mercury is more accurate. Because of the widely different values of C_p in water and mercury ($C_{p_w} : C_{p_m} = 30:1$), the effect of a minute quantity of water on the mean heat capacity of the mixture is disproportionately large, as shown by the calculations in Appendix XVIII.B.

The present results show that the experimental technique for measuring ΔT requires further refinement if the efficiency of the mercury pump is to be determined thermometrically. Considerable improvements would be obtained by fitting adequate insulation round the pump and pipework to minimize heat losses. In addition, it is suggested that the T_1 temperature probe should be repositioned, preferably by inserting it through

164.

the bottom of the sump so that it projects into the pump inlet, where it would measure the true pump inlet temperature. If these precautions were taken, thermometric efficiency measurements would be eminently suitable for any turbomachine running in mercury, because of the low heat capacity of that fluid which leads to relatively large temperature increments. Sophisticated instrumentation would be unnecessary: a ten-fold reduction in precision compared with the Hewlett Packard thermometer would be quite acceptable for an accuracy in ΔT measurement better than $\pm 1\%$.

The results have also shown that thermometric measurements are only suitable for a monophase fluid, or for a two phase fluid where the second phase is present in a small enough proportion to be neglected. This is more important for two fluids whose thermal properties (in particular the heat capacity C_p) are radically different. A maximum of 5% for the second phase is suggested.

13.7 Industrial Application of Thermometric Methods of Efficiency Measurement

Thermometric techniques are particularly suitable for the continuous monitoring of the efficiency of turbomachinery. The method has been successfully applied to a water pump operating close to maximum efficiency, with a generated head of only 7.5m. Industrial application of the technique for other low head turbomachines running in water is therefore feasible, although expensive instrumentation with a resolution of 10^{-4}C would be required.

A more promising industrial application is for the performance monitoring of pumps handling liquids of low thermal capacity, such as liquid metals, freon and Benzene. Problems of heat loss which were encountered in the present research, could be overcome with efficient lagging and judicious positioning of the temperature probes. Because of the larger temperature rise in such fluids, sophisticated and costly instrumentation becomes unnecessary. A resolution of $\pm$ 0.01°C would have been adequate for measurements on the mercury pump, giving an accuracy better than $\pm$ 2.5% for the computed efficiency (see Equation 13.15). Furthermore, the tedious statistical analysis of temperature data, which was performed manually in this project, could be automatically processed using microchip technology.

CHAPTER 14

CONCLUSIONS

The present work falls into three main sections, as outlined in Chapter 1, and the conclusions relating to each section will therefore be considered separately.

14.1 Performance of the Standard Pump

1.   It has been shown that for the conventional performance scaling theory of rotodynamic machines (based on equality of rotational Reynolds Number), changes in speed and fluid viscosity are not necessarily equivalent. Variatons in fluid viscosity have a more pronounced effect on Reynolds Number dependent parameters (such as skin friction losses) for a given change of Re_ω.

2.   The present pump design leads to an unusual relationship between seal leakage and hydraulic efficiency, because the high velocity leakage flow from the lower neckring is discharged directly into the pump inlet. Partial recovery of the dynamic pressure of the leakage increases the pump generated head.

3.   The concept of a total flow coefficient, based upon the pump delivered flowrate plus leakage, may be used to predict the pump head characteristic for different seal clearances in a given fluid at a fixed rotational speed. The technique is less successful for speed or viscosity changes and cannot be applied to the pump power characteristics.

4. Due to the leakage effects described in (2) above, conventional methods for predicting the pump performance in mercury from its head and power characteristics in water are not always successful, particularly at very high or low flows. An empirical scaling technique has been developed, whereby the seal clearance on the water pump is enlarged to give a similar leakage rate (as a percentage of total pump flowrate) to that on the mercury pump. Using this method, the accuracy of head performance prediction in mercury is better than $\pm 2\%$, although the power requirements of the pump may only be predicted to $\pm 5\%$ at best. An enlarged seal clearance is unnecessary for efficiency predictions, since the widest discrepancy between the standard pump efficiency characteristics in water and mercury is $\pm 1\%$.

The scaling technique described above may be useful in other industrial applications, where pump acceptance trials must be conducted in water, although the prospective operating fluid is of a lower kinematic viscosity (e.g. naphtha, benzene, freon, etc.).

5. The rapid rate of neckring wear is a major cause for dissatisfaction with the standard pump at I.C.I. Metallographic investigations have shown that a simple modification of the pump fabrication material from a grey cast iron to, perhaps, a spheroidal cast iron would eliminate the release of abrasive ferrite particles into the mercury flow, thereby reducing the rate of neckring wear.

An additional contributory factor is the continual running of the pump in the chlorine plant at a flowrate well below its maximum efficiency. The problem of wear would be diminished in a pump designed to produce the specified head and flowrate at peak efficiency and considerable power savings would also be achieved.

4.2 Hydrodynamic Seal Performance

1. A hydrodynamic seal has been designed to replace the existing top neckring seal of the standard pump. Despite wider clearances than in a

conventional face seal, the HDS eliminates leakage and, in consequence, the pump generated head is improved. The extra power absorbed by the seal can be reduced by staging and it is partially offset by the lower leakage rate, so that the existing motor is still adequate to drive the pump/two-stage HDS assembly. The overall efficiency of this configuration is comparable with that of an unworn standard pump.

2.   HDS performance is not impaired when it runs in conjunction with the pump, rather than alone with a symmetrically applied inlet pressure. Fluid preswirl and pressure asymmetry at the seal inlet, caused by the presence of the pump, reduces the parasitic pressure rise and hence improves the overall sealing capacity.

3.   The sealing capacity of a HDS is similar in water and mercury. The essential differences in performance for the two fluids are:

(a) If inadequate pressure is maintained at the inlet to a HDS running in mercury with water inside the interface, the interface breaks down and water is pumped through the seal. Similar behaviour in water with air inside the interface is unlikely and solutions to the problem for mercury operation have been suggested.

(b) Water entrainment at the mercury interface is more prevalent than air entrainment in water, where surface tension forces predominate.

4.   In a staged HDS, bubbles of fluid from inside the interface collect at the interstage region. This does not detract from the performance of a seal running intermittently, but may become a problem with sustained operation and a bleed flow path to carry away the trapped fluid is advisable.

168.

4.3 Thermometric Efficiency Measurements

1.   The efficiency of the water pump operating close to maximum efficiency has been successfully measured using a thermometric technique. The pump head of 7.5m is considerably lower than the hitherto accepted minimum of 100m for such measurements.

2.   Problems of heat transfer were encountered when the technique was applied to the pump in mercury. Analysis of the results has shown that these problems could be overcome and that thermometric methods for measuring efficiency are particularly suitable for pumps handling low thermal capacity fluids, such as freon, benzene and liquid metals.

3.   The technique is unsuitable for two-phase fluids, unless the second phase is present in a small enough quantity to be neglected. (A maximum of 5% for water in mercury is suggested). This is particularly important for two phases with widely differing thermal properties.

CHAPTER 15

RECOMMENDATIONS FOR FUTURE WORK

Results from the present work suggest that further research in the following areas would be fruitful.

1. The non-equivalence of variations in fluid viscosity and speed for changes in rotational Reynolds Number

It is suggested that the performance of a single pump (rather than two or more nominally identical pumps) should be examined over a wide range of speeds and viscosities, to incorporate laminar, transitional and fully rough/turbulent through-flow conditions.

2. The effects of seal leakage on pump performance

This is particularly important where leakage is discharged into the pump inlet. A more comprehensive method for leakage prediction than is presently available should be developed. Scaling of pump power requirements with high leakage rates could be further refined and the possibility of improving pump performance by channelling leakage flow back into the impeller should be examined.

3. Methods to improve interface stability in a HDS

Progress in this field is required for applications where the pressure to be sealed by a HDS (and hence the interface radius) cannot be closely defined, and also for staged seals, where the interface lies at a wide relative radius. Future work could included visual examination of the process of bubble entrainment at the interface and of interface breakdown at low seal inlet pressures.

4. Thermometric techniques for pump efficiency measurement

These methods should be further refined and extended in scope.
Their most useful application lies in performance monitoring of pumps
for the chemical industry, where fluids of low thermal capacity (such
as mercury) are common.

REFERENCES

1. KIRK OTHMER, Encyclopaedia of Chemical Technology, 2nd Ed., Vol.1,
        Wiley & Sons, pp.678-695 (1963).

2. CONSIDINE, D.M. (Ed.) Chemical & Process Technology Encyclopaedia,
        McGraw Hill, (1974).

3. SCONCE, J.S. Chlorine, its Manufacture, Properties and Uses.
        Am.Chem.Soc. Monograph, Reinhold Pub.Co., N.York (1962).

4. HODGE, R.N. Mercury Pumps - Preliminary Note giving details of
        the Performance of Existing Pumps and describing the Design
        and Development of New Centrifugal and Bucket Wheel Pumps.
        I.C.I. Mond Division, Report MD/186 (28.2.64).

5. ORSZAK, P. Electromagnetic Pumps for Sodium-Cooled Reactors. In
        "Pumps for Nuclear Power Plant", Mechanical Engineering
        Publications Ltd., London (1974).

6. CORDIER, O. Similitude Parameters for Flow Machines (1953) (in
        German). Trans. S. Merry, Ed. M.T. Thew. Report ME/76/24,
        Southampton University (1976).

6a. DAILY, J.W. Hydraulic Machinery. Chapter 13 in "Engineering
        Hydraulics", Ed. H. Rouse, Wiley & Sons, N.York (1950).

6b. SABERSKY, R.H. and ACOSTA, A.J. Fluid Flow. Chapter 9.
        Collier-MacMillan, N.York (1st Edition) (1964).

6c. BALJÉ, O.E. A Study on Design Criteria and Matching of Turbomachines:
        Part B - Compressor and Pump Performance and Matching of Turbo-
        components. Trans.ASME, J.Eng. for Power 84, pp.103-114,
        (Jan.1962). See also BALJÉ, O.E. Turbomachines. Wiley and Sons, New York (1981).

7. WOOD, G.M., MANFREDI, D.V. and CYGNOR, J.R. Centrifugal Types of
        Dynamic Shaft Seals. ASME Paper 63-W a-167 (1963).

8. Minutes of Meeting held at I.C.I. on 14.5.76 to discuss Mercury
        Pump Development for J/K Units (BCH/JN/TECH. 18.5.76).

9. Minutes of Meeting to discuss Mercury Pump Development for J Unit
        (BCH/JN/TECH. 29.7.76).

10. FARRANT, P.E. and McEWAN, D. Use and Interpretation of Dimensionless
        Pump Parameters. Lecture No.4, Introductory Course to Pump
        Testing. NEL, East Kilbride, Glasgow. (11.10.77).

11. DAILY, J.W. Hydraulic Machinery. In "Engineering Hydraulics",
       Proc. 4th Hydraulics Conference, Iowa, 1949 (Ed. H. Rouse).
       Pub. Wiley & Sons, Ch.XIII, pp.858-992 (1950).

12. IPPEN, A.T. Influence of Viscosity on Centrifugal Pump Performance.
       Trans. ASME, Vol. 68, No.6, pp.823-848 (1946).

13. DAUGHERTY, R.L. Investigation of the Performance of Centrifugal
       Pumps when Pumping Oils. Bulletin 126, Goulds Pumps Inc. (1925).

14. DAUGHERTY, R.L. A Further Investigation of the Performance of
       Centrifugal Pumps when Pumping Oils. Bulletin 130, Goulds
       Pumps Inc. (1926).

15. PANTELL, K. The Behaviour of Centrifugal Pumps Operating with
       Heavy Oils. (1953) (in German). Trans. S. Merry. Report ME/77/28,
       Southampton University (1977).

16. STEPANOFF, A.J. Centrifugal and Axial Flow Pumps. Pub. Chapman &
       Hall Ltd., London. Chapter 14.4, pp.308-317 (1957). (2nd Edition)

17. HORTON, G. Interim Note on the Performance of the Mercury Pumps
       on the High Slope Mark I Cells at Castner-Kellner Works.
       I.C.I. Mond Division Report No. MD.4607 (2.9.66).

18. MERRY, S.L. Mercury Pumping. Progress Report No.1, Report ME/77/12
       Southampton University (March 1977).

19. NIXON, R.A. and CAIRNEY, W.D. Scale Effects in Centrifugal Cooling
       Water Pumps for Thermal Power Stations. NEL Report No.505,
       East Kilbride, Glasgow. D.T.I. (1972).

20. OSTERWALDER, J. and ETTIG, C. Determination of Individual Losses
       and Scale Effect by Model Tests with a Radial Pump. Proc.Conf.
       on Scaling for Performance Prediction in Rotodynamic Machines,
       University of Stirling, 6-8 September 1977. I.Mech.E. Conference
       Publications 1977-7.

21. FAY, A. On the High Accuracy Scaling-Up for Pumps and Turbines.
       Proc.Conf. on Pumps and Turbines (Vol.I). N.E.L. East Kilbride,
       1-3 September 1976 (Paper 2-5).

22. BOBOK, E. Wall Roughness Effects on Loss Coefficient of Centrifugal
       Pumps. Proc. 5th Conf. on Fluid Machinery, Vol.I., Budapest.
       (Ed. L. Kisbocskói and Á. Szabó) p.103 . (1975).

23. NIKURADSE, J. Strömungsgesetze in rauhen Rohren. V.D.I. Forschungsb.
       No.361 (1933). (Transl. in N.A.C.A. Tech.Memo 1292).

24. MILLIONSCHCHIKOV, M.D., SUBBOTEN, V.I., IBRAGIMOV, M.Kh.,
    TARANOV, G.S. and KOBZAR, L.L. Hydraulic Resistance and
    Velocity Fields in Tubes with Artificial Wall Roughness.
    Soviet Atomic Energy, 34, 4, October 1975, pp.306-315.

25. SCHLICHTING, H. Experimentelle Untersuchungen zum Rauhigkeitsproblem
    Ingenieur-Archiv 7, pp.1-34 (1936) Trans. in Proc. ASME (1936).

26. OSTERWALDER, J. Scale Effect on Performance and Efficiency of
    Hydraulic Turbomachines. In Von Karman Institute Lecture
    Series No.61 on Recent Progress in Pump Research, Vol. II,
    December 1973.

27. GODDARD, S.J. Feasibility Tests on Hydrodynamic Disc Seals for
    Particle Laden Liquids. Ph.D. Thesis, Southampton University
    (1976).

28. BENEDICT, R.P. Fundamentals of Temperature, Pressure and Flow
    Measurement. 2nd Edition, John Wiley & Sons, N.York (1977),
    (Chapter 17.3).

29. HUTTON, S.P. Private communication (June 1978).

30. HADJI-SHEIK, M. The Performance of Pumps for Automotive Cooling
    Systems. M.Phil. Thesis, Southampton University (1979).

31. PEARSON, A.R. and DEEPROSE, W.M. Basic Fluid Mechanics and Pump
    Types. Lecture No.1, Introductory Course to Pump Testing,
    N.E.L., East Kilbride, Glasgow (11.10.77).

32. DAILY, J.W. and NECE, R.E. Roughness Effects in Frictional
    Resistance of Enclosed Rotating Discs. Trans. ASME Series D.
    J.Bas.Eng'g (1960), 82, pp.553-560.

33. WATABE, K. On Fluid Friction of Rotating Rough Disc in Rough
    Vessel. JSME (1958) 1(1), pp.69-74.

34. DAILY, J.W., ERNST, W.D. and ASBEDIAN, V.V. Enclosed Rotating
    Disks with Superimposed Throughflow: Mean Steady and Periodic
    Unsteady Characteristics of the Induced Flow. M.I.T. Dept. of
    Civil Engineering Hydrodynamics Lab. Report No.64 (April 1964).

35. WEBER, D. Experimental Investigations on Axial Flow Annular Slots
    such as Occur in Impeller Pumps (in German). Konstruktion (1972)
    24(b), pp.205-210. Pub. Springer Verlag 1972. Transl. by
    G.L.Cairns. N.E.L. Report No.TT.2422, East Kilbride, Glasgow
    (1972).

36. BRITISH STANDARDS INSTITUTION. Methods for the Measurement
   of Fluid Flow in Pipes, Part I: Orifice Plates, Nozzles and
   Venturi Tubes. BS.1042:Part I, 1964. Amended Sept.1965 and
   Dec.1968.

37. PERRY, J.H. Chemical Engineers Handbook. McGraw Hill, Section 3
   (1973).

38. CHEM.ABS. (Pub. American Chemical Society) 78, 102118x (1973).

39. J. Unit Maintenance Manual, Section 5, Fig.6 (I.C.I. Mond Division
   Internal Publication), 4.7.66.

40. ROBERSON, J.A. and CROWE, G.T. Engineering Fluid Mechanics.
   Houghton Miffin Co., Boston (1975).

41. WYLER, J.S. and BENEDICT, R.P. Trans.ASME J.Eng.Power, Oct.1975,
   p.569. "Comparisons between Throat and Pipe Wall Tap Nozzles".

42. MOORE, T. Literature Review on the Effects of Viscosity on the
   Performance of Centrifugal Pumps. Report No. TN.1530,
   BHRA, Cranfield, March 1979.

43. MERRY, S.L. Mercury Pumping. Progress Report No.2. Report No.
   ME/79/7, Southampton University (April 1979).

44. Internal Communication from B. Schofield (N.W.R. Materials Group,
   Heath Laboratory, I.C.I. Runcorn) to C.T. MacKenzie (15.8.74).

45. FLEMING, I.K., MOLLOY, N.A. and McCARTHY, M.J. Mercury Flow in
   Metallic Conduits under Non-wetting and Amalgamating Conditions.
   Nature Phys.Sci. 240, Nov.20, pp.69-71 (1972).

46. MOODY, L.F. Friction Factors for Pipe Flow. Trans ASME 66,
   p.671 (1944).

47. SELIM, S.M.A. Cavitation Erosion in Fluid Flow. Ph.D. Thesis,
   Southampton University (1981).

48. KRATZER, A. Corrosion and Erosion Damage to Chemical Centrifugal
   Pumps. In "Pumps for Progress", 4th Tech.Conf. British Pump
   Manufacturers' Assoc., 9-10 April 1975, Durham. (Org. BHRA Cranfield)

49. THEW, M.T. and SAUNDERS, M.G. The Hydrodynamic Disc Seal. Paper H5,
   Proc. 3rd Internat.Conf. on Fluid Sealing, Cambridge, U.K. 1967.
   Pub. BHRA Cranfield (1968).

50. ESELGROTH, P. Centrifugal Pumps with Hydrodynamic Seals Reduce Maintenance and Increase Reliability. Pumps 138, March 1978, pp.125-127.

51. DAILY, J.W. and NECE, R.E. Chamber Dimension Effects on Induced Flow and Frictional Resistance of Enclosed Rotating Discs. Trans. ASME Ser.D. J.Bas.Eng. 82, 1960, pp.217-232.

52. HOWARD, F.B. Aspects of the Hydrodynamic Disc Seal - Development and Performance. Ph.D. Thesis, Southampton University, (1972).

53. WILFLEY, A.R. & Sons.Inc. Centrifugal Pump having Hydraulic Seal Means. British Patent Spec. No.1222 598, Pub. 17.2.1971.

54. SUNDSTRAND CPN. High Pressure Centrifugal Pump Assembly. British Patent Spec.No. 1349 903. Pub. 10.4.74.

55. SAUNDERS, D.J. and CAMAC, G. Improvements in or relating to Pumps. British Patent Spec. No.1 185 312. Pub. 25.3.70.

56. BILLINGTON, I.J., SMILLE, W.D. and STONEHILL, B.C. Shaft Seals for Liquid Applications in a Space Environment. Can.Aeron. & Space J. 11 (9), pp.347-55 (1965).

57. THEW, M.T. The Labyrinth/Hydrodynamic Disc Seal (LHDS). Proc. 8th Int.Conf. on Fluid Sealing, Durham, Sept.1978. Paper B.1, Publ. BHRA, Cranfield.

58. THORNE, E.W. and BOWER, J.R. Axial Thrust in Semi-Open Impellers. In 'Process Pumps', Pub. I.Mech.E., London (1973).

59. ANAND, J.S. The Effects of Aqueous Media Drag Reducers on the Performance of the Hydrodynamic Disc Seal. Ph.D. Thesis, University of Southampton (1974).

60. SAUNDERS, M.G. The Hydrodynamic Disc Seal. M.Phil. Thesis, University of Southampton (1968).

61. PROSSER, M.J. The Hydraulic Design of Pump Sumps and Intakes BHRA, Cranfield, July 1977.

62. CRC Handbook of Chemistry and Physics. 58th Ed. 1977-1978. Ed. R.C. Weald, CRC Press Inc., Cleveland, Ohio.

63. TRITTON, D.J. Physical Fluid Dynamics. Van Nostrand Reinhold Co., London (1977).

64. ZALOSH, R.G. and JENSEN, D.S. A Numerical Model of Droplet Entrainment from a Contained Oil Slick. in "Fluid Mechanics in the Petroleum Industry", Ed. C. Dalton. ASME New York, (1975).

65. COLMAN, D.A. and THEW, M.T. Hydrocyclone Development for Water/ Mercury Separation: Report No.3. Report No.ME/76/5, Southampton University (February 1976).

66. WHILLM, G. and CAMPMAS, P. Efficiency Measurements for Hydraulic Turbines by the Poirson Thermometric Method (in French). Houille Blanche $\underline{9}$(4), pp.449-460 (1954).

67. FOORD, T.R., LANGLANDS, R.C. and EL AGIB, A.A.R. New Developments in the Thermometric Methods of Measuring Hydraulic Efficiency and Flow. NEL Report No.130. East Kilbride, Glasgow: National Engineering Laboratory (January 1964).

68. EL AGIB, A.A.R. Principles of the Thermodynamic Methods of Measuring the Efficiency of Hydraulic Machines. NEL Report No.163: East Kilbride, Glasgow: National Engineering Laboratory (1964).

69. NORDGARD, J.S. Thermodynamic Determination of Power Loss in Hydraulic Components. ASME Paper No.72-WA/FE-22, New York: American Society of Mechanical Engineers, (1972).

70. WHILLIER, A. Pump Efficiency Determination in Chemical Plant from Temperature Measurements. Ind.Eng.Chem. Process Des. and Dev., $\underline{7}$(2) pp.194-6 (1968).

71. WHILLIER, A. On Line Determination of High-Head Pumps Handling any Liquid. S.Afr.Mech.Engr., $\underline{20}$(1), pp.12-14 (1970).

72. COLON, F.P. The Overall Recovery Factor in Thermometric Pump Efficiency Tests. NEL Report No.421. East Kilbride, Glasgow: National Engineering Laboratory (1969).

73. LENNOX, S.C. and CHADWICK, M. Mathematics for Engineers and Applied Scientists. Heinemann, London (1974).

74. EL AGIB, A.A.R., BINNIE A.J. and FOORD, T.R. Effects of Recovery Factor on Measurement of Temperature of Moving Fluids. NEL Report No.224, East Kilbride, Glasgow: National Engineering Laboratory (April 1966).

75. KJØLLE, A. Thermodynamic Methods for Determining Losses in Hydraulic Components - A Survey. NEL Report No.657, East Kilbride, Glasgow: National Engineering Laboratory (1978).

76. American Institute of Physics Handbook, 3rd Ed. (1974). Coordinating Editor D.E. Gray. McGraw-Hill, London.

77. WISLICENUS, G.F. Fluid Mechanics of Turbomachinery. McGraw-Hill Book Company Inc., New York (1947).

78. YAMADA, Y. Torque Resistance of a Flow between Rotating Co-Axial Cylinders having Axial Flow. Bull.JSME $\underline{5}$(20), pp.634-42 (1962).

79. BILGEN, E., BOULOS, R. and AKGUNGOR, A.C. Leakage and Frictional Characteristics of Turbulent Helical Flow in Fine Clearance. Trans ASME Series I: J.Fluid Eng. $\underline{95}$(4), pp.493-7 (1973).

80. DORFMAN, L.A. Hydrodynamic Resistance and the Heat Loss of Rotating Solids. Trans. N. Kemmer. Oliver and Boyd, London (1963).

81. THEW, M.T. Further Experiments on the Hydrodynamic Disc Seal. Proc. 4th Int.Conf. on Fluid Sealing. Philadelphia, USA. (1969). Publ. ASME, Illinois.

82. McNOWN, J.S., LEE, H.M., McPHERSON, M.B. and ENGEZ, S.M. Influence of Boundary Proximity on the Drag of Spheres. Proc. 7th Int.Cong. for Appl.Mech., London. Vol.II, Paper 2 (1948).

83. DAVIES, C.N. Definitive Equations for the Fluid Resistance of Spheres. Proc.Phys.Soc. $\underline{57}$(4), pp.259-270 (1945).

84. LYON, R.N. Liquid Metal Heat-Transfer Coefficients. Chem.Eng. Progress $\underline{4}$, pp.75-79 (1951).

85. BENNETT, C.O. and MYERS, J.E. Momentum, Heat and Mass Transfer. McGraw-Hill Book Co.Inc., New York (1962).

86. McADAMS, W.H. Heat Transmission. 3rd Ed. p.260. McGraw-Hill Book Co.Inc., New York (1954).

87. RODGERS, G.F.C. and MAYHEW, Y.R. Engineering Thermodynamics Work and Heat Transfer. 2nd Edition. Longmans, London (1967).

88. WIESNER, F.J. A Review of Slip Factors for Centrifugal Impellers. J. Eng. Power. Trans ASME $\underline{89}$ (4) p.558 (Oct 1967).

89. Flow Measurement. H and B News p.3. Publ. Hartmann and Brown (UK) Ltd, Northampton. (Winter 1974).